

The Northeast Greenland Margin - Tectonic Evolution

Dissertation

zur Erlangung des akademischen Grades doctor rerum naturalium
(Dr. rer. nat.)



seit 1558

vorgelegt dem Rat der Chemisch-Geowissenschaftlichen Fakultät der
Friedrich-Schiller-Universität Jena

von Diplom-Geophysiker Tobias Hermann
geboren am 22. Juli 1986 in Zeulenroda

Gutachter:

1. Prof. Dr. Gerhard Jentzsch, Friedrich-Schiller-Universität Jena
2. Prof. Dr. Wilfried Jokat, Alfred-Wegener-Institut Bremerhaven
3. PD Dr. Thomas Jahr, Friedrich-Schiller-Universität Jena

Tag der öffentlichen Verteidigung: 06. November 2013

**The Northeast Greenland Margin -
Tectonic Evolution**

Dissertation

Tobias Hermann

Summary

The Norwegian-Greenland Sea is an area of increasing interest. Here, the North Atlantic Current continues the Gulf Stream into the Norwegian-Greenland Sea. The warm ocean current plays an important role for the climate in Europe and influences the environment of the global Earth system. For climate reconstructions, the tectonic evolution of the Norwegian-Greenland Sea has to be known. Calculations of climate models for the future based on the evolution in the past. Based on few geological and geophysical data, the tectonic evolution of the Norwegian-Greenland Sea and the Northeast Greenland margin remains controversial. Seasonal sea ice cover and short summer seasons complicate the data acquisition along the Northeast Greenland margin.

In the summer of 2009, the Alfred Wegener Institute (AWI) acquired geophysical data along the Northeast Greenland margin during the ARK-XXIV/3 expedition. Two seismic refraction lines as well as gravity data, measured in parallel to the seismic refraction lines, were gathered in the Boreas Basin and offshore Kong Oscar Fjord. In addition, further gravity data of the Norwegian-Greenland Sea are available from the Arctic Gravity Project (ArcGP) and were used within this study.

Summarising our results, we could develop crustal models for the Boreas Basin and offshore Kong Oscar Fjord, using the seismic refraction data and the gravity data. Furthermore, a complex 3D gravity model of the Northeast Greenland margin was calculated, using the crustal models and further published data as boundary conditions. The crustal model of the Boreas Basin shows a 3 km thin oceanic crust without a significant lower oceanic crust (absence of oceanic layer 3). In contrast, the crustal model offshore Kong Oscar Fjord shows a 9 km thick oceanic crust and 3 km thick high-velocity lower crust (HVLC) within the continent-ocean transition zone. Our 3D gravity model shows thin oceanic crust in the Boreas Basin and the Greenland Basin (3–4 km) as well as thick oceanic crust offshore Kong Oscar Fjord. Between the Greenland Basin and the offshore Kong Oscar Fjord, the variation of the crustal thickness could be modelled across the narrow Jan Mayen Fracture Zone.

Summary

Following our conclusions, the structure of the oceanic crust (crustal thickness, absence of oceanic layer 3) along the ultraslow spreading Knipovich Ridge is more heterogeneous than previously thought. For the accretion of the thick oceanic crust offshore Kong Oscar Fjord, the rift history of Northeast Greenland (extensive rifting before continental breakup) is more important than higher mantle temperatures caused by the Iceland Hotspot. Therefore, the Iceland Hotspot has a smaller area of influence on the oceanic crustal accretion than previously thought.

Zusammenfassung

Die Norwegen-Grönlandsee ist ein Gebiet von großem wissenschaftlichem Interesse, da sich verändernde Meeresströmungen in diesem Bereich globale Auswirkungen zur Folge haben. Die warme Meeresströmung des Nordatlantikstroms, eine Verlängerung des Golfstroms, hat einen bedeutenden Einfluss auf das Klima in Europa und weltweit. Veränderungen dieser Meeresströmung sind unter anderem von der Meeresbodentopographie und demzufolge von der tektonischen Situation abhängig. Um Aussagen über die Zukunft des Nordatlantikstroms und das Klima machen zu können, ist das Verständnis über die frühere Entwicklung der Meeresströmung und die tektonische Entwicklung der Norwegen-Grönlandsee Voraussetzung. Dennoch bestehen bis heute Unklarheiten über die tektonische Entwicklung der Norwegen-Grönlandsee. Die Beseitigung dieser Unklarheiten mithilfe neuer Daten wird durch die saisonale Meereisbedeckung und die kurze Sommersaison vor Nordostgrönland erschwert.

Die dieser Arbeit zugrunde liegenden geophysikalischen Daten sind vom Alfred-Wegener-Institut (AWI) im Rahmen der Schiffsexpedition ARK-XXIV/3 im Sommer 2009 erhoben worden. Zielgebiet der Expedition war der Kontinentalrand von Nordostgrönland. Es wurden unter anderem zwei refraktionsseismische Profile im Boreas Becken und vor dem Kong Oscar Fjord vermessen. Parallel dazu wurden kontinuierlich Schwerefeld-daten erhoben. Zusätzliche Schwerefelddaten des Arctic Gravity Project (ArcGP) im Bereich der Norwegen-Grönlandsee sind ebenfalls in die Interpretation mit eingeflossen. Die Ergebnisse dieser Arbeit beinhalten zwei Modelle der Erdkruste im Bereich des Boreas Beckens und vor dem Kong Oscar Fjord. Des Weiteren ist ein komplexes 3D-Dichtemodell des nordostgrönländischen Kontinentalrandes erstellt worden. Im Boreas Becken konnte eine 3 km dünne ozeanische Kruste, ohne eine deutliche Unterkruste (keine ozeanische Schicht 3), modelliert werden. Im Gegensatz dazu wurde vor dem Kong Oscar Fjord eine 9 km mächtige ozeanische Kruste und ein 3 km mächtiger Hochgeschwindigkeitskörper in der Unterkruste des Kontinent-Ozean-Übergangsbereichs modelliert. Das 3D-Dichtemodell zeigt dünne ozeanische Kruste im Boreas Becken und

Zusammenfassung

Grönland Becken (3–4 km), sowie dicke ozeanische Kruste vor der Küste des Kong Oscar Fjords. Die Krustenmächtigkeit zwischen dem Grönlandbecken und vor dem Kong Oscar Fjord ändert sich deutlich über die Jan-Mayen-Bruchzone hinweg.

Die Modelle zeigen, dass der Krustenaufbau (Krustenmächtigkeit, keine ozeanischen Schicht 3) am extrem langsam spreizenden Knipovich Rücken heterogener ist als ursprünglich angenommen. Im Gegensatz dazu, ist für die Bildung dicker ozeanischer Kruste vor dem Kong Oscar Fjord die frühere Entwicklung des ostgrönländischen Rifts (starke Dehnung vor dem kontinentalen Aufbruch) wichtiger als hohe Manteltemperaturen durch den Island-Hotspot. Dies führt zu der Vermutung, dass der Island-Hotspot einen geringeren Einflussbereich auf die Bildung ozeanischer Kruste hat als bisher angenommen.

Contents

Summary	i
Zusammenfassung	iii
Contents	v
List of Figures	ix
List of Tables	xi
Abbreviations	xiii
1 Introduction	1
1.1 Motivation	1
1.2 Outline	3
2 The Norwegian-Greenland Sea	5
2.1 Regional Setting	5
2.1.1 Bathymetry	5
2.1.2 Seismic Refraction Lines	8
2.1.3 Gravity Field	10
2.2 Geological Evolution	11
2.3 Crustal Structures	14
2.3.1 Oceanic Crust	14
2.3.2 Continental Crust	17
3 Seismic Refraction Data	19
3.1 General Settings	19
3.1.1 Data Acquisition	19
3.1.2 Processing	21
3.1.3 Modelling	23

Contents

3.1.4	Error Analysis	30
3.2	Line Boreas Basin – Knipovich Ridge (20090200)	32
3.2.1	P- and S-wave Models	32
3.2.2	Error Analysis	39
3.2.3	Discussion of Line 20090200	40
3.3	Line Kong Oscar Fjord – Kolbeinsey Ridge (20090100)	49
3.3.1	P-wave Model	49
3.3.2	Error Analysis	54
3.3.3	Discussion of Line 20090100	56
4	Gravity Data	65
4.1	Gravimetric 2.5D Modelling	65
4.1.1	Data Acquisition, Processing and Modelling	65
4.1.2	Line Boreas Basin – Knipovich Ridge (20090200)	66
4.1.3	Line Kong Oscar Fjord – Kolbeinsey Ridge (20090100)	70
4.2	Gravimetric 3D Modelling	75
4.2.1	The Arctic Gravity Project (ArcGP)	75
4.2.2	Boundary Conditions	75
4.2.3	The 3D Model	80
4.2.4	Residuals	90
4.2.5	Discussion of the 3D Gravity Model	94
5	Crustal Variations along the Northeast Greenland Margin	101
5.1	Iceland Hotspot	101
5.2	An Evolution Model for the East Greenland Margin	105
5.3	Comparison with South Atlantic Margin	107
6	Conclusion and Discussion	109
7	Outlook	113

8	References	115
A	Appendix (Seismic Refraction Data)	139
	Acknowledgement	I
	Selbstständigkeitserklärung	III
	Curriculum Vitae	V

Contents

List of Figures

2.1	Map of the Norwegian-Greenland Sea	6
2.2	Seismic refraction lines in northern North Atlantic	9
2.3	Arctic Gravity Project (ArcGP) map of northern North Atlantic	11
2.4	Geological evolution Norwegian-Greenland Sea	13
2.5	Crustal thickness versus spreading rate	17
3.1	Locations of seismic refraction lines	20
3.2	Workflow for seismic data processing, modelling and interpretation	22
3.3	Projection of land stations onto the seafloor	23
3.4	Example: P-wave data for line 20090200	25
3.5	Example: OBS data for line 20090100	26
3.6	Example: REFTEK data for line 20090100	27
3.7	Example: S-wave data for line 20090200	28
3.8	Travel times P- and S-waves of line 20090200	29
3.9	Origin of S-waves	30
3.10	Velocity model of line 20090200	34
3.11	Interpretation of line 20090200	35
3.12	Ray coverage of line 20090200	36
3.13	1D crustal P-wave velocity model of line 20090200	38
3.14	Resolution of line 20090100	40
3.15	Crustal and upper mantle structures of Knipovich Ridge and its magmatic centres	42
3.16	P-wave model line 20090100	50
3.17	Interpretation line 20090100	51
3.18	Ray coverage and resolution of line 20090100	52
3.19	Combined P-wave models at Kolbeinsey Ridge	57
3.20	Crustal transect across northern North Atlantic	59
3.21	Crustal structure of conjugate Vøring margin	63

List of Figures

3.22 Comparison crustal thickness: Kolbeinsey Ridge crust – normal oceanic crust	64
4.1 $V_P - \rho$ relation	67
4.2 2.5D gravity model of line 20090200	68
4.3 2.5D gravity model of line 20090100	73
4.4 Arctic Gravity Project (ArcGP) map of northern North Atlantic	76
4.5 Boundary conditions 3D gravity model	81
4.6 Spectral analysis gravity field	82
4.7 Gravity model section 1	84
4.8 Gravity model section 4	86
4.9 Gravity model section 9	87
4.10 Gravity model section 13	89
4.11 Modelled sediment thickness	91
4.12 Modelled crustal thickness	92
4.13 Measured, calculated and residual free-air anomaly	95
4.14 Gravity effect of the mantle	99
5.1 Crustal thickness versus spreading rate	102
5.2 Global S-wave tomography of northern North Atlantic	104
7.1 Boundary conditions 3D gravity model	114
A.1 Example: OBS data of line 20090200	140
A.2 Example: OBS data of line 20090200	141
A.3 Example: OBS data of line 20090100	142
A.4 Example: OBS data of line 20090100	143
A.5 P- and S-wave travel times of line 20090200	144

List of Tables

2.1	Crustal layering of continental and oceanic crust	15
2.2	Classification mid-ocean ridges	16
3.1	General specifications of seismic refraction lines and air gun array . . .	21
3.2	Estimated pick uncertainties	24
3.3	Significance of line 20090200 velocity model	39
3.4	Comparison of crustal structures at Knipovich Ridge	43
3.5	Significance of line 20090100 velocity model	55
3.6	Domains of Atlantic rifted margins	62
4.1	Boundary conditions for 3D gravity modelling	78
4.2	Densities of geological model bodies	80
4.3	Densities of mantle model bodies	82
4.4	General comparison of gravity models	93

List of Tables

Abbreviations

AGC	Automatic Gain Control
AR	Aegir Ridge
ArcGP	Arctic Gravity Project
AS	Amagmatic Segment
AWI	Alfred Wegener Institute
BA	Bouguer Anomaly
BB	Boreas Basin
BGGS	Bodensee Gravimeter Geosystem GmbH
BVFC	Bremstein-Vingleia Fault Complex
CFB	Caledonian Fold Belt
COB	Continent-Ocean Boundary
COT	Continent-Ocean Transition Zone
DAAD	German Academic Exchange Service
DGG	German Geophysical Society
δV_s	Shear Wave Velocity Anomaly
EGR	East Greenland Ridge
EGU	European Geosciences Union
FA	Free-air Anomaly
GB	Greenland Basin
GEOMAR	Helmholtz Centre for Ocean Research Kiel
GEUS	Geological Survey of Denmark and Greenland
GFZ	Greenland Fracture Zone
HVLC	High-velocity Lower Crust
HR	Hovgård Ridge
IBCAO	International Bathymetric Chart of the Arctic Ocean
IGSN	International Gravity Standardisation Network
JMB	Jan Mayen Basin

Abbreviations

JMFZ	Jan Mayen Fracture Zone
JMI	Jan Mayen Island
JMMC	Jan Mayen Microcontinent
JMR	Jan Mayen Ridge
KB	Kolbeinsey Basin
KbR	Kolbeinsey Ridge
KOF	Kong Oscar Fjord
KR	Knipovich Ridge
LB	Lofoten Basin
Moho	Mohorovičić Discontinuity
MR	Mohns Ridge
MS	Magmatic Segment
NB	Norway Basin
NEGS	Northeast Greenland Shelf
OBS	Ocean Bottom Seismometer
ODP	Ocean Drilling Programme
PJMFZ	Proto-Jan Mayen Fracture Zone
PSD	Power Spectral Density
RFL	Seismic Reflection Line
RFR	Seismic Refraction Line
RMS	Root Mean Square
RR	Reykjanes Ridge
RV	Research Vessel
ρ	Density
ScS	Scoresby Sund
ScSFZ	Scoresby Sund Fracture Zone
SFZ	Senja Fracture Zone
TP	Trøndelag Platform
V_P	P-wave Velocity

V_S	S-wave Velocity
VB	Vøring Basin
VM	Vøring Margin
VMH	Vøring Marginal High
WFZ	Western Fault Zone
WGS	World Geodetic System

Abbreviations

1 Introduction

1.1 Motivation

The Norwegian-Greenland Sea is the northern part of the Northeast Atlantic. Furthermore, the Norwegian-Greenland Sea is significantly influenced by the North Atlantic Current, which continues the Gulf Stream to the north. The North Atlantic Current is an important part of the global Thermohaline Circulation, which is closely connected to the world's climate (Müller-Michaelis et al. 2013). Thus, the tectonic evolution of the Norwegian-Greenland Sea and variations of the current itself are important parameters for climate research. Therefore, the Norwegian-Greenland Sea is an area of increased interest for research.

However, the tectonic history of Northeast Greenland and the influence of the Iceland Hotspot on its formation is controversial due to few geophysical data along its continental margin (Mjelde et al. 2008b, Voss et al. 2009). For a better understanding of the rifting process in general, it is necessary to know the crustal variations along the Northeast Greenland continental margin. The crustal and upper mantle structures allow conclusions about the interaction of tectonic and magmatic processes during the continental breakup. The current knowledge is based on seismic refraction lines south of Kong Oscar Fjord and north of the Jan Mayen Fracture Zone (73–75°N; Schlindwein & Jokat 1999, Voss et al. 2009). Therefore, this study focuses on: (1) the Boreas Basin at 77°N, and (2) Kong Oscar Fjord at 72°N.

For the Boreas Basin, the poor magnetic data (ambiguous and weak magnetic spreading anomalies; Ehlers & Jokat 2009) and the missing seismic refraction data lead to several speculations on the nature of the Boreas Basin crust (oceanic vs. continental; Døssing et al. 2008). In addition, several seismic investigations at the ultraslow spreading Knipovich Ridge indicates thin oceanic crust and likely the absence of the lower oceanic crust (oceanic layer 3) in the Boreas Basin (Ritzmann et al. 2002).

The Kong Oscar Fjord is an important region along the Northeast Greenland margin (Schlindwein & Jokat 1999). North and south of the fjord significant differences are

1 Introduction

evident: (1) a high-velocity lower crust (HVLC) is only found north of Kong Oscar Fjord, and (2) onshore the thickness of exposed flood basalts is different to the north (thin flood basalts) and south (thick flood basalts) of the fjord (Escher & Pulvertaft 1995, Schlindwein & Jokat 1999, Henriksen et al. 2009). The nature and extent of the high-velocity lower crust below Kong Oscar Fjord remain uncertain (Weigel et al. 1995, Schlindwein & Jokat 1999). Therefore, new geophysical data is important for the understanding of the evolution of the research area (Boreas Basin, Kong Oscar Fjord), and subsequently the tectonic history of the Northeast Greenland margin.

In summer 2009, the Alfred Wegener Institute (AWI) carried out the ARK-XXIV/3 expedition with the German research icebreaker Polarstern to the Northeast Greenland margin (Jokat et al. 2010). The main objective of the expedition was to acquire geoscientific data to improve our knowledge about the tectonic and glacial history of Northeast Greenland.

During the expedition, the AWI acquired two seismic refraction lines: (1) in the Boras Basin, and (2) seaward of Kong Oscar Fjord (Jokat et al. 2010). Along the seismic refraction lines, gravity data were recorded in parallel. Furthermore, the public-domain gravity data grid of the Norwegian-Greenland Sea (Arctic Gravity Project, ArcGP; Kenyon et al. 2008) were used to modify evolution models for Northeast Greenland.

The seismic refraction data yield information on the crustal and upper mantle structures. Density informations along both seismic refraction lines can be obtained by 2.5D gravity models. Using the gravity data grid of the Norwegian-Greenland Sea, a 3D gravity model could be developed, using the seismic models and further published data as boundary conditions. Hence, spatial crustal variations like the crustal thickness and the Moho depth can be displayed.

Based on these data, a better understanding of the tectonic evolution of the Northeast Greenland margin is possible. Hence, the evolution model of the Northeast Greenland margin could be modified.

1.2 Outline

The temporal and spatial complexity of the tectonic evolution of the Northeast Greenland margin leaves open questions and is still under debate (e. g. Foulger & Anderson 2005, Mjelde et al. 2008b). Answering some open questions, like e. g. unknown crustal structures in the Boreas Basin and offshore Kong Oscar Fjord, seismic and gravity data are used. Two seismic refraction lines were acquired in these areas by the AWI during ARK-XXIV/3 expedition in 2009 (Jokat et al. 2010). Furthermore, gravity data were recorded in parallel to both seismic refraction lines. A gravity grid (ArcGP) of the research area with a resolution of 5' x 5' (Kenyon et al. 2008) is used for a 3D gravity model, investigating variations of crustal structures along the Northeast Greenland margin. For this purpose, various published geophysical datasets like other seismic refraction lines (e. g. Voss et al. 2009), interpreted geomagnetic data (e. g. Ehlers & Jokat 2009), research wells (e. g. Myhre et al. 1995d), and other 3D gravity models (e. g. Schmidt-Aursch & Jokat 2005b) are incorporated in our investigations.

Firstly, the Norwegian-Greenland Sea and the main research area are introduced physiographically (Chapter 2). In addition, published seismic refraction lines at the Northeast Greenland margin are mentioned and typical continental as well as oceanic crustal structures are explained.

Data acquisition, processing, modelling, and error analysis of the seismic refraction data are presented in Chapter 3.1 for both seismic lines. The modelled seismic refraction data are shown, interpreted, and discussed for the lines in the Boreas Basin (Chapter 3.2) and offshore Kong Oscar Fjord (Chapter 3.3).

On the basis of the modelled seismic refraction lines, 2.5D gravity models are developed along both seismic refraction lines (Chapter 4.1). The calculated 2.5D gravity models and other published geophysical datasets are used as boundary conditions for a 3D gravity model (Chapter 4.2). Our 3D gravity model of the Northeast Greenland margin is further discussed in the subsequent paragraphs of the chapter.

1 Introduction

The results of this thesis and other published data of the Northeast Greenland margin (e. g. Voss et al. 2009) allow the modification of evolution models of the research area (Chapter 5). In addition, the modified models are compared with evolution models for the South Atlantic margin. Finally, some conclusions about the tectonic evolution of the Northeast Greenland margin (Chapter 6) and suggestions for further investigations are made (Chapter 7).

2 The Norwegian-Greenland Sea

Greenland is the largest island of the world and covers an area of about 2.2 million km². Its north-south extension is about 2600 km and the latitude ranges between 60°N and 83°N. The east-west extension is about 1200 km and the longitude ranges between 11°W and 73°W. The coastline is approximately 44000 km long. To the east, Greenland is bounded by the northern North Atlantic.

The following study concentrates on the Norwegian-Greenland Sea which is the northern part of the Northeast Atlantic. The Norwegian-Greenland Sea is bounded by Norway to the east, the Barents Sea and Svalbard to the Northeast, the Fram Strait to the north, Northeast Greenland to the west, and Iceland to the south (Fig. 2.1).

The evolution and the structures of the eastern part of the Norwegian-Greenland Sea, namely the Norway margin, is well understood, based on geological and geophysical data (e. g. Mjelde et al. 2008b). In contrast, the evolution and the structure of the conjugate Northeast Greenland margin remain controversial due to rough sea ice conditions and short summer periods. During the 2009 summer expedition, the Alfred Wegener Institute (AWI) could acquire and collect geophysical and geological data along the Northeast Greenland margin (Jokat et al. 2010).

2.1 Regional Setting

2.1.1 Bathymetry

The main research area – the Northeast Greenland margin – is located in the Norwegian-Greenland Sea (NGS) as northern part of the Northeast Atlantic (Fig. 2.1). Recently published bathymetric data (IBCAO – International Bathymetric Chart of the Arctic Ocean, Jakobsson et al. 2012) show the primary features of the Norwegian-Greenland Sea: (1) mid-ocean ridges, (2) continental margins, and (3) deep ocean basins.

In general, the mid-ocean ridges consist of three active spreading main segments within the Norwegian-Greenland Sea (Fig. 2.1): (1) Kolbeinsey Ridgem (KbR), (2) Mohs Ridge (MR), and (3) Knipovich Ridge (KR). These ridges are located along the plate

2 The Norwegian-Greenland Sea

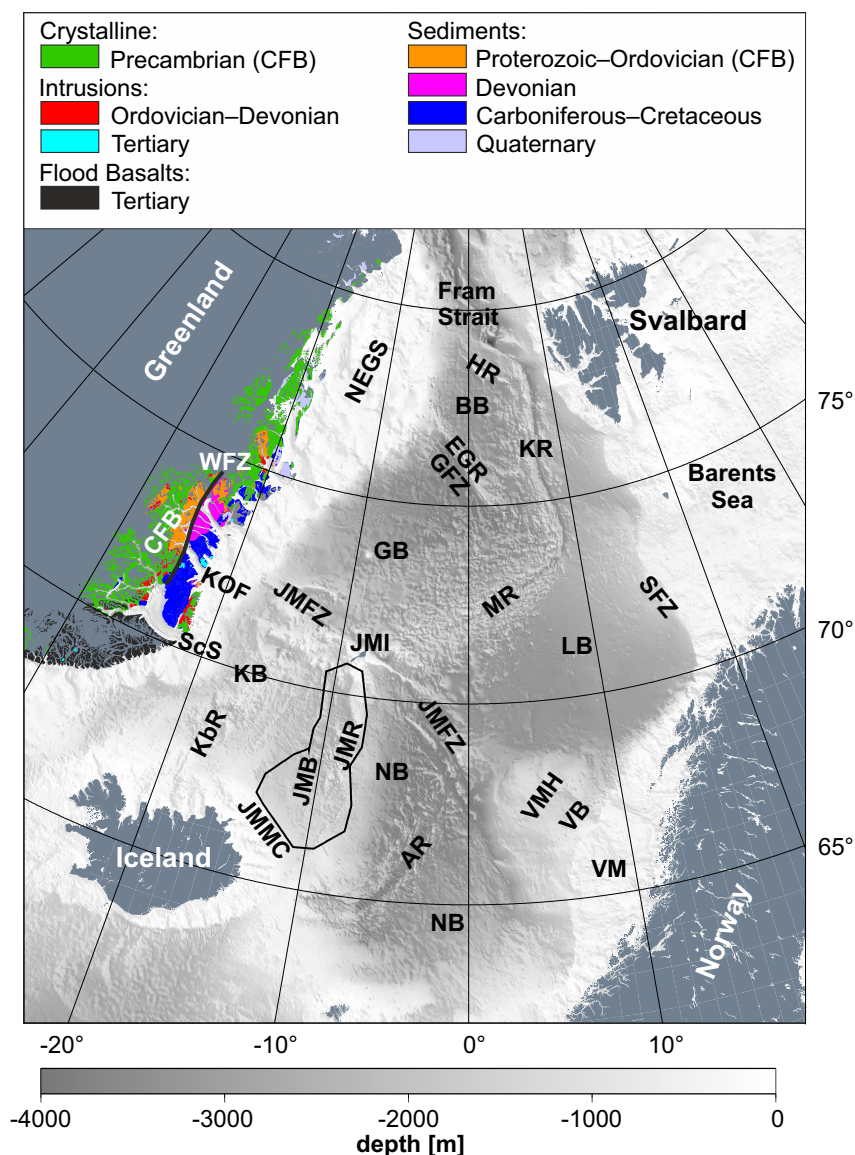


Figure 2.1: Bathymetric map (IBCAO, Jakobsson et al. 2008) showing the Norwegian-Greenland Sea and the simplified geology of Northeast Greenland (Henriksen et al. 2009). AR–Aegir Ridge, BB–Boreas Basin, CFB–Caledonian Fold Belt, EGR–East Greenland Ridge, GB–Greenland Basin, GFZ–Greenland Fracture Zone, HR–Hovgård Ridge, JMB–Jan Mayen Basin, JMFZ–Jan Mayen Fracture Zone, JMI–Jan Mayen Island, JMMC–Jan Mayen Microcontinent (Gaina et al. 2009), JMR–Jan Mayen Ridge, KB–Kolbeinsey Basin, KbR–Kolbeinsey Ridge, KOF–Kong Oscar Fjord, KR–Knipovich Ridge, LB–Lofoten Basin, MR–Mohns Ridge, NB–Norway Basin, NEGS–Northeast Greenland Shelf, ScS–Scoresby Sund, SFZ–Senja Fracture Zone, VB–Vøring Basin, VM–Vøring Margin, VMH–Vøring Marginal High, WFZ–Western Fault Zone.

boundary between the North American-Greenland and the Eurasian plates (Eldholm et al. 1990). Especially the Mohns Ridge represents a symmetrical plate boundary with respect to its adjacent basins. In contrast, north and south to the Mohns Ridge, the Knipovich and Kolbeinsey ridges, respectively, indicate asymmetrical plate boundaries. This asymmetry is related to the complex plate tectonic history of the Norwegian-Greenland Sea (see Chapter 2.2).

The Norwegian and Northeast Greenland continental margins are characterised by large shelf areas with wide shelf slopes (Eldholm et al. 1990). The Northeast Greenland shelf increases in wideness from south to north resulting in large sediment fans at the margin slope to the south (e. g. offshore Scoresby Sund (ScS) and Kong Oscar Fjord (KOF); Fig. 2.1). In contrast, the central Norway margin (Vøring margin, VM) is characterised by a prominent plateau (Vøring Marginal High, VMH) and a continental basin (Vøring Basin, VB; Fig. 2.1).

Physiographically, the Norwegian-Greenland Sea is divided into three regions: (1) southern region, (2) central region, and (3) northern region. These regions are separated by first-order fracture zone systems of the Jan Mayen Fracture Zone (JMFZ) and the Greenland-Senja Fracture Zone (Fig. 2.1).

The southern region is bounded by Iceland in the south and the Jan Mayen Fracture Zone in the north. It comprises the Kolbeinsey Basin (KB), the Jan Mayen Micro-continent (JMMC), and the Norway Basin (NB; Fig. 2.1). Within the Kolbeinsey Basin the active Kolbeinsey Ridge is located and in the Norway Basin the extinct Aegir Ridge (AR) can be found. The Jan Mayen Micro-continent is divided into the eastern Jan Mayen Ridge (JMR) and the western Jan Mayen Basin (JMB). The Jan Mayen island (JMI) rises up above the position where the Jan Mayen Fracture Zone and the Jan Mayen Ridge cross perpendicular. The Jan Mayen Fracture Zone is composed of a western and an eastern segment (Fig. 2.1). The western segment is the present active transform fault, trending west-northwest. It is a prominent bathymetric escarpment to the north of the Kolbeinsey Basin and Jan Mayen Micro-continent. The eastern segment represents the extinct transform fault and is structurally more complex. It consists of two parallel features trending southeast.

2 The Norwegian-Greenland Sea

The central region is bounded by the Jan Mayen Fracture Zone to the south and the Greenland-Senja Fracture Zone to the north. Its main structure is the Mohns Ridge separating the Lofoten Basin (LB) to the east and the Greenland Basin (GB) to the west (Fig. 2.1). The northern boundary of the Lofoten Basin is the Senja Fracture Zone (SFZ), which is buried below thick sediments from the Barents Sea. The northern boundary of the Greenland Basin is characterised by the East Greenland Ridge (EGR) as a distinct bathymetric feature and a continental sliver (Døssing et al. 2008). The Greenland Fracture Zone (GFZ) as counterpart to the Senja Fracture Zone is directly located at the southern end of the East Greenland Ridge, bounding the Greenland Basin to the north.

The northern region, north of the Greenland-Senja Fracture Zone, is dominated by the asymmetric spreading Knipovich Ridge and the Boreas Basin (BB) to the east (Fig. 2.1). The Hovgård Ridge (HR) bounded the Boreas Basin to the north.

2.1.2 Seismic Refraction Lines

In general, seismic refraction investigations were carried out to investigate deep crustal structures. Especially rifted continental margins, like the Norwegian continental margin, were explored by such methods (e. g. Breivik et al. 2006, Mjelde et al. 2009). First seismic refraction investigations, studying the conjugate continental margin of Northeast Greenland, started in 1988 by the AWI (Fig. 2.2; Weigel et al. 1995). Further investigations of the AWI focused on the area between Scoresby Sund and the East Greenland Ridge (Fig. 2.2; Schlindwein & Jokat 1999, Schmidt-Aursch & Jokat 2005a, Voss & Jokat 2007, Voss et al. 2009).

Remaining questions about crustal structures offshore Kong Oscar Fjord and the absence of seismic refraction lines north of the East Greenland Ridge (Boreas Basin), resulted in seismic refraction investigations of the AWI in these regions (Fig. 2.2; Jokat et al. 2010, Hermann & Jokat 2013a,b). However, sea ice cover of the Northeast Greenland shelf prevented the prolongation of the seismic refraction line, located in the Boreas Basin, onto the shelf. Therefore, the investigations were concentrated on the ultraslow

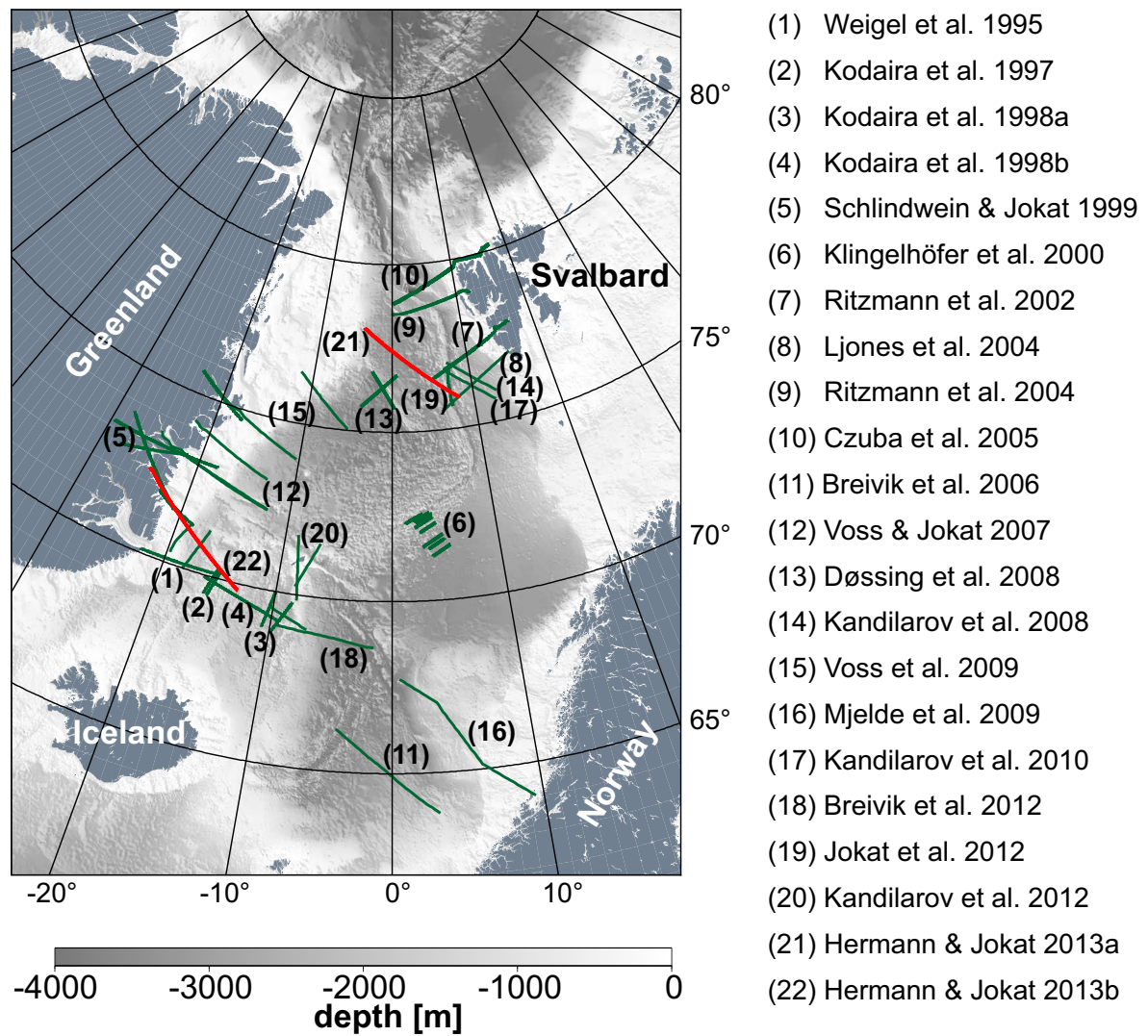


Figure 2.2: Bathymetric map (IBCAO, Jakobsson et al. 2008) showing existing seismic refraction lines in northern North Atlantic (green) and the seismic refraction lines of this study (red).

2 The Norwegian-Greenland Sea

spreading Knipovich Ridge. In this area and at the ultraslow spreading Mohns Ridge, extensive research was carried out in the last several years (Fig. 2.2; Klingelhöfer et al. 2000, Ritzmann et al. 2002, Ljones et al. 2004, Ritzmann et al. 2004, Czuba et al. 2005, Kandilarov et al. 2008, 2010, Jokat et al. 2012a).

Further seismic refraction surveys in the Norwegian-Greenland Sea investigated the relations of the Jan Mayen Micro-continent (Fig. 2.2; Kodaira et al. 1997, 1998a,b, Breivik et al. 2012, Kandilarov et al. 2012) and the East Greenland Ridge, a continental sliver (Døssing et al. 2008), to the tectonic evolution of this area.

2.1.3 Gravity Field

In general, gravity data were used to obtain spatial variations of crustal and upper mantle structures. For this purpose, a consistent database is necessary. The public-domain Arctic Gravity Project grid (ArcGP, Chapter 4.2.1; Kenyon et al. 2008) with a resolution of 5' x 5' is the database for the Norwegian-Greenland Sea (Fig. 2.3). This compiled free-air anomaly grid ranges between $-800 \mu\text{m/s}^2$ on the Northeast Greenland Shelf and $1200 \mu\text{m/s}^2$ at the Barents Sea Shelf. Generally, high values above $500 \mu\text{m/s}^2$ are observed at the shelf slopes, the Mohns Ridge, and the Knipovich Ridge (Fig. 2.3). In addition, both ridges show gravity lows (-200 – $100 \mu\text{m/s}^2$) along the mid-ocean rift valleys. In contrast, along the Kolbeinsey Ridge no distinct gravity low is observed. Other linear structures within the free-air anomaly map are the Jan Mayen Fracture Zone and the East Greenland Ridge. Both structures show lower gravity values ($<200 \mu\text{m/s}^2$) than the surroundings (Fig. 2.3). The Boreas Basin, the Greenland Basin, and the Lofoten Basin are characterised by values between $0 \mu\text{m/s}^2$ and $250 \mu\text{m/s}^2$. The Kolbeinsey Basin shows higher values than the other basins ($>500 \mu\text{m/s}^2$).

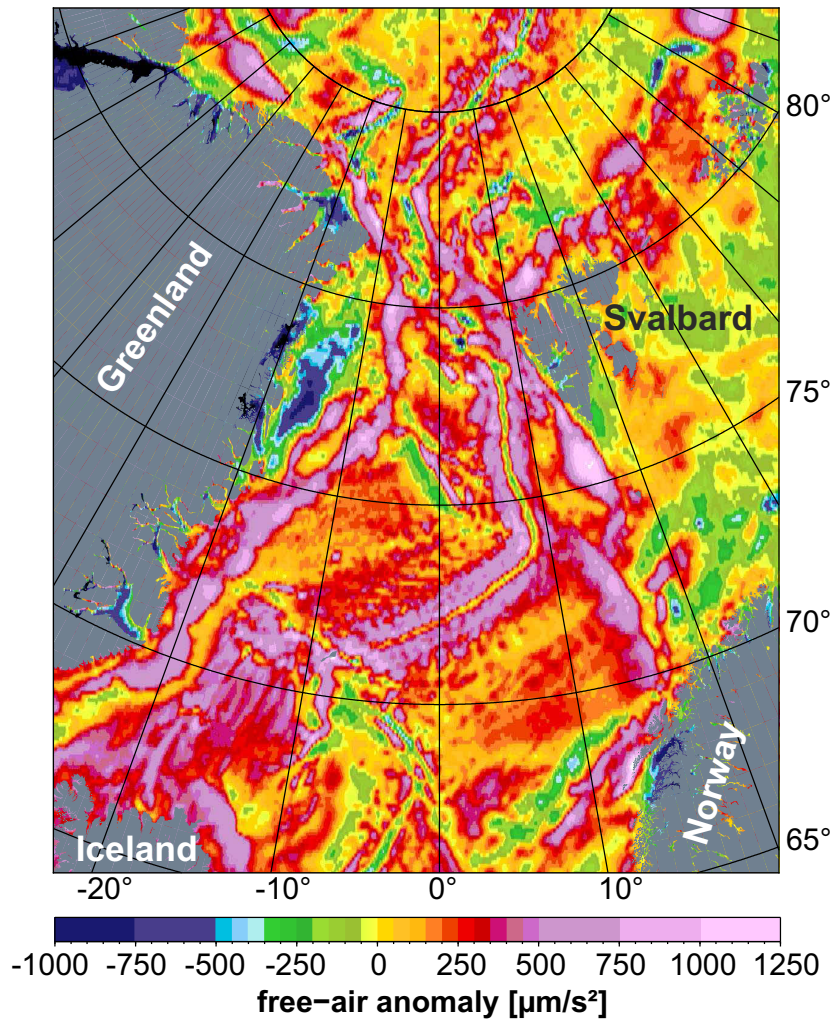


Figure 2.3: Free-air anomaly map of the northern North Atlantic with a resolution of $5' \times 5'$ (ArcGP, Kenyon et al. 2008).

2.2 Geological Evolution

The Norwegian-Greenland Sea and the Northeast Greenland margin have been subject to various geophysical and geological studies, investigating the tectonic evolution. The Northeast Greenland margin is dominated by the Caledonian fold belt (CFB), which was formed in Silurian times during the closing of the Iapetus Ocean through continent-continent collision (Haller 1985). Furthermore, the continental margin is characterised by sediment basins east of the Caledonian fold belt (Fig. 2.1). The basins were separated from the Caledonian fold belt by the Western Fault Zone (WFZ; Fig. 2.1), and

2 The Norwegian-Greenland Sea

developed during the ensuing Devonian extensional collapse and long-term rifting (Escher & Pulvertaft 1995, Henriksen et al. 2009). The Mesozoic rifting process culminated in Tertiary magmatism, resulting in large amounts of flood basalts and the formation of the Norwegian-Greenland Sea (Escher & Pulvertaft 1995, Henriksen et al. 2009). However, the influence of the Iceland Hotspot on the formation of the flood basalt provinces and the continental breakup is still under debate (e. g. White & McKenzie 1989, Korenaga et al. 2000, Foulger & Anderson 2005, Mjelde et al. 2008b).

Generally, the tectonic evolution of the Norwegian-Greenland Sea took place in two main stages (Talwani & Eldholm 1977). The first stage started with a continental breakup between Greenland and Europe in the Early Eocene (55–56 Ma, magnetic anomaly C24; Talwani & Eldholm 1977, Gradstein et al. 2012). Simultaneously, seafloor spreading started along the Mohns Ridge and the Aegir Ridge (Fig. 2.4A).

The second stage began with a change of the spreading direction between Greenland and Europe in the Early Oligocene (\sim 33 Ma, magnetic anomaly C13; Fig. 2.4B; Talwani & Eldholm 1977, Mosar et al. 2002a,b). Since that time, the tectonic evolution of the northern and southern region of the Norwegian-Greenland Sea is different. In the northern region asymmetric and oblique spreading started at the Knipovich Ridge (Figs. 2.4B,C; Talwani & Eldholm 1977, Mosar et al. 2002a). Hence, the Boreas Basin opened and the East Greenland Ridge were formed as a continental sliver staying attached to the continental margin of Northeast Greenland (Faleide et al. 1993, Døssing et al. 2008). However, the evolution of the Boreas Basin is still controversial, because there is an ongoing debate whether an extinct spreading centre in the the Boreas Basin exist or not (e. g. Mosar et al. 2002b, Ehlers & Jokat 2009).

In the southern region the detachment of the Jan Mayen Micro-continent off East Greenland was initialised (e. g. Gaina et al. 2009). In the Oligocene (\sim 30 Ma), the final jump of the spreading axis from the Aegir to the Kolbeinsey Ridge took place and the Aegir Ridge became extinct (Fig. 2.4C). Gradually, the Jan Mayen Micro-continent became completely detached from the East Greenland margin around 20 Ma (magnetic anomaly C6; Gradstein et al. 2012), thus, establishing seafloor spreading

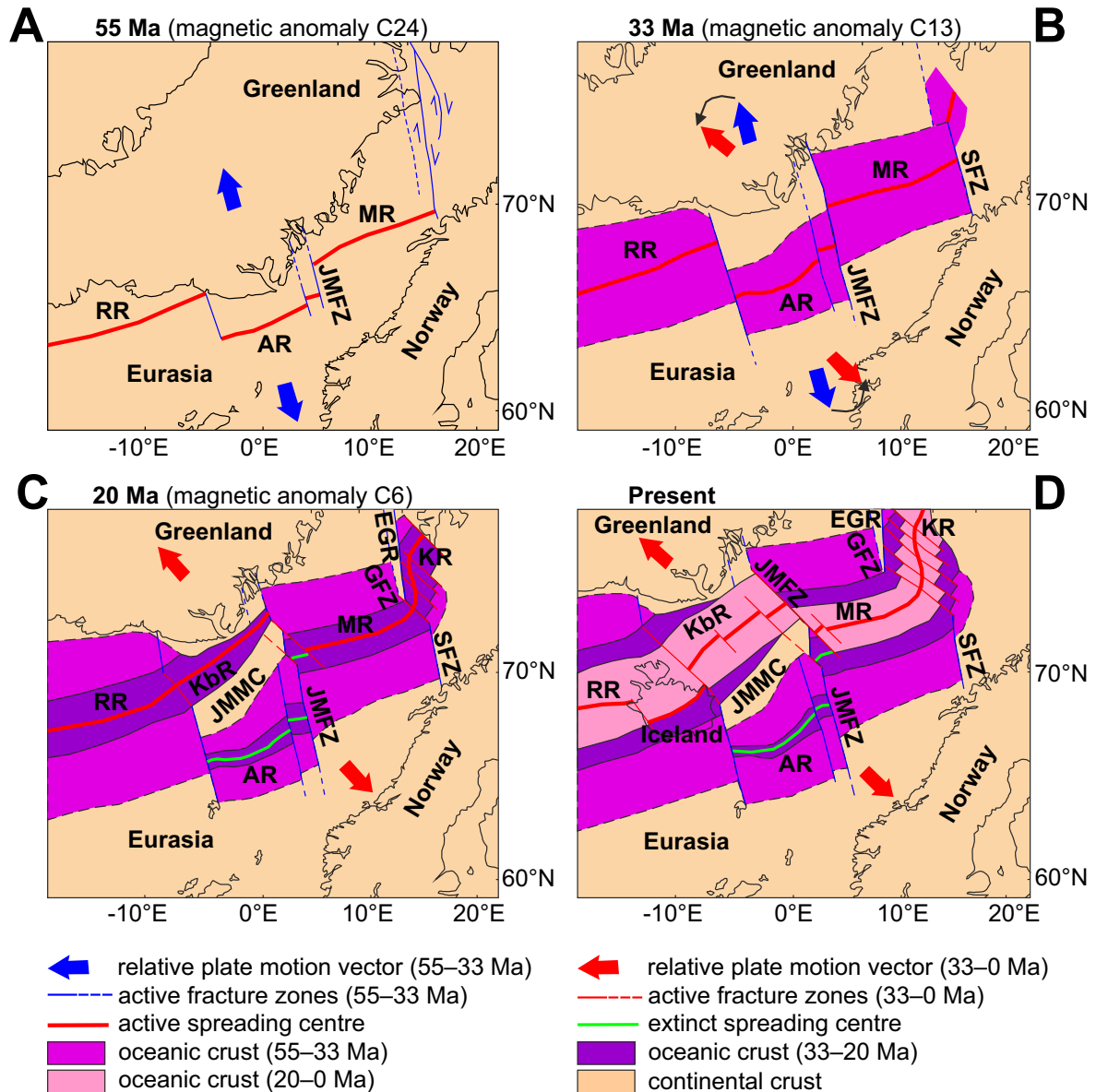


Figure 2.4: Geological evolution schema of the Norwegian-Greenland Sea according to Lundin & Doré (2002). The geological evolution is divided into four steps: (A) continental breakup and initiation of seafloor spreading, (B) plate reorganisation and change in relative plate motion direction, (C) northward propagation of the Kolbeinsey Ridge from the southern Reykjanes Ridge (RR) and breakup of the Jan Mayen Micro-continent, and (D) present geological situation.

2 The Norwegian-Greenland Sea

along the Kolbeinsey Ridge (Fig. 2.4D; Gaina et al. 2009). However, the reasons for the formation of the micro-continent are still under debate. Different models suggest that the detachment was triggered by the crossing Iceland Hotspot across the East Greenland margin (e. g. Gaina et al. 2009) or by the emplacement of high-velocity lower crust (Yamasaki & Gernigon 2010).

2.3 Crustal Structures

2.3.1 Oceanic Crust

In general, oceanic crust is formed by decompression melting below diverging plates at mid-ocean spreading ridges (White et al. 1992). Various geological and geophysical investigations show that the oceanic crust has the same structure and basaltic composition everywhere. Hence, the oceanic crust is divided into three main layers (Tab. 2.1; Juteau & Maury 1999): (1) oceanic layer 1 or sediments, (2) oceanic layer 2, and (3) oceanic layer 3. Oceanic layer 1 is built up by various unconsolidated sediments. The P-wave velocities are lower than 3.5 km/s.

Oceanic layer 2 can be divided into three sublayers (Tab. 2.1; Juteau & Maury 1999): (1) oceanic layer 2A, (2) oceanic layer 2B, and (3) oceanic layer 2C. The oceanic layer 2 consists of pillow lava (extrusive rocks, oceanic layer 2A) and sheeted dykes (intrusive rocks, oceanic layer 2C). Oceanic layer 2B represents the transition between extrusive and intrusive rocks (Tab. 2.1; Klingelhöfer et al. 2000). However, in some seismic refraction investigations, oceanic layer 2B cannot be resolved because of low data quality and large distances of the ocean bottom seismometers. As a consequence, oceanic layer 2 is only divided into oceanic layer 2A and oceanic layer 2B. In this case, oceanic layer 2B comprises the sheeted dykes and the transition between pillow lava and sheeted dykes. The P-wave velocities of oceanic layer 2 are generally lower than 6.3 km/s.

Oceanic layer 3 can be divided into oceanic layer 3A and oceanic layer 3B (Tab. 2.1; Juteau & Maury 1999). The sublayers were formed by gabbro and cumulate-rich gabbro,

respectively. For ultraslow spreading ridges (full spreading rate ≤ 20 mm/a), oceanic layer 3 might be absent (Jokat et al. 2003). However, this observation is still under discussion. The P-wave velocities are lower than 7.5 km/s and the resulting normal oceanic crust is 7 km thick (White et al. 1992). The underlying mantle consists of peridotite and has normal P-wave velocities above 7.9 km/s (Tab. 2.1).

Table 2.1: Continental (Holbrook et al. 1992) and oceanic crustal structures (Juteau & Maury 1999). The continental crust at volcanic margins has a high-velocity lower crust (HVLC), which is absent at non-volcanic margins. For the upper oceanic crust, a division in only two sublayers, oceanic layer 2A and oceanic layer 2B, is possible for seismic data of low data quality. In this case, oceanic layer 2B consists of the sheeted dykes and the transition between pillow lava and sheeted dykes.

Layer	P-wave velocity [km/s]	Characteristic
Continental Crust		
Sediment	< 6.0	Various Sedimentary Rock Types } Various Crystalline Rock Types
Upper Continental Crust	5.7 – 6.3	
Lower Continental Crust	6.3 – 6.9	
HVLC	7.0 – 7.5	
Mantle	> 7.9	Peridotite
Oceanic Crust		
Sediment	1.6–3.5	Various Sedimentary Rock Types
2A } 2B } 2C } 3A } 3B }	2.7–4.5 4.8–5.5 5.8–6.3 6.5–6.9 7.0–7.5	Pillow Lava Transition: Pillow Lava–Sheeted Dykes Sheeted Dykes Gabbros Cumulate-rich Gabbros
Upper Oceanic Crust		
Lower Oceanic Crust		
Mantle		
	> 7.9	Peridotite

2 The Norwegian-Greenland Sea

Classification of Mid-Ocean Ridges

Mid-ocean ridges can be divided into ultraslow, slow, intermediate, and fast spreading ridges (Dick et al. 2003). In addition to the spreading rate, the different mid-ocean ridge types can be divided by their morphological characteristics (Tab. 2.2), which depend on the composition and the thermal structure of the mantle. The crustal thickness shows low correlation to the spreading rate for values of 20 mm/a to 180 mm/a (observed full spreading rate; Reid & Jackson 1981, Bown & White 1994, White et al. 2001). In contrast, a high correlation exists for values less than 20 mm/a, where the crustal thickness decreases rapidly (Fig. 2.5).

Table 2.2: Classification of mid-ocean ridges based on (full) spreading rate and morphology (Dick et al. 2003).

Ultraslow	Slow	Intermediate	Fast
<ul style="list-style-type: none"> - <20 mm/a - intermittent volcanism (magmatic & amagmatic ridge segments) - absence of oceanic layer 3 in amagmatic segments - lack of transform faults 	<ul style="list-style-type: none"> - 20–55 mm/a - deep rift valleys with highly variable relief - rough rift mountain topography weakly correlated to spreading rate 	<ul style="list-style-type: none"> - 55–70 mm/a - long alternating sections with either slow or fast spreading ridge morphology 	<ul style="list-style-type: none"> - 80–180 mm/a - low axial highs - minimal rift mountain topography uncorrelated to spreading rate

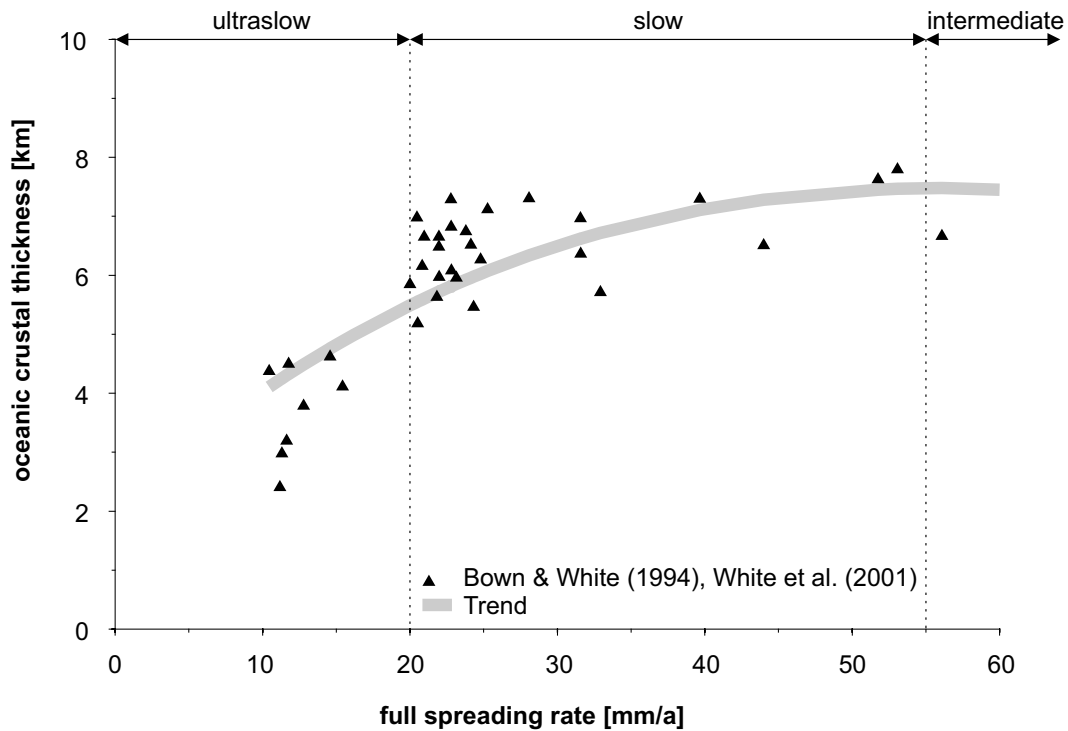


Figure 2.5: Crustal thickness versus spreading rate for ultraslow and slow spreading mid-ocean ridges (Dick et al. 2003).

2.3.2 Continental Crust

In general, the structure and composition of the continental crust are variable depending on tectonic provinces, like e. g. passive rifted margins (Christensen & Mooney 1995). Therefore, no general specifications on crustal composition can be made (Tab. 2.1; Holbrook et al. 1992, Christensen & Mooney 1995). A few examples for typical crustal rocks are amphibolite, gneiss, granite, and granulite. All these rocks show similar depth-dependent P-wave velocities and, therefore, a classification based on P-wave velocities can be made. The P-wave velocities of the upper continental crust are between 5.7 km/s and 6.3 km/s (Tab. 2.1). The lower crust has P-wave velocities less than 6.9 km/s. At volcanic margins, high P-wave velocities of 7.0 km/s to 7.5 km/s can be observed within the lower continental crust (high-velocity lower crust, HVLC) and likely indicates mafic material (Holbrook et al. 1992).

2 The Norwegian-Greenland Sea

Continent-Ocean Transition Zone (COT)

At continental margins, the transition from continental to oceanic crust is widely defined and uncertain. In this study, we used the definition of the continent-ocean transition zone (COT) after Whitmarsh & Miles (1995) for the transitional crust: the COT is that part of the lithosphere which includes the crust between the thinned continental crust characterised by tilted fault blocks and the first oceanic crust formed by seafloor spreading.

3 Seismic Refraction Data

3.1 General Settings

In the summer of 2009, the AWI acquired two seismic refraction lines – 20090200 and 20090100 – during the expedition ARK-XXIV/3 (Jokat et al. 2010). Main research area was the Northeast Greenland margin (Fig. 3.1). Line 20090200 crosses the central Boreas Basin from the Knipovich Ridge to the Northeast Greenland margin. The 340 km long line consists of 18 ocean bottom seismometers (OBS, KUM 1997; Fig. 3.1B). Line 20090100 starts within Kong Oscar Fjord, overlaps the existing seismic refraction line 94340 (Schlindwein & Jokat 1999) by 150 km and terminates 100 km east of the Kolbeinsey Ridge (Fig. 3.1C). For this 500 km long line four land stations and 20 OBS were used.

3.1.1 Data Acquisition

For data acquisition of both seismic refraction lines similar configurations were used (Tab. 3.1; Jokat et al. 2010). All 38 OBS were equipped with a Guralp CMG-40T broadband seismometer and a hydrophone. The REFTEK-72 land stations (Fig. 3.1) had three channels with three 4.5 Hz-geophone chains each to improve the signal-to-noise ratio. The data were recorded with a sample rate of 100 Hz (Jokat et al. 2010). The seismic energy was consistently generated by an air gun array consisting of eight G-Guns with a total volume of 66 l fired at 200 bar (Tab. 3.1). Based on an average ship velocity of 2.5 m/s and a shot interval of 60 s, the resulting shot distance was approximately 150 m (Jokat et al. 2010).

The resolution of seismic data is characterised by the Fresnel zone (Militzer & Weber 1987). The vertical resolution is about 50 m below seafloor (using a seismic velocity of 1.8 km/s and a peak frequency of 9 Hz) and decreases to about 300 m in 10 km depth (using a seismic velocity of 7.0 km/s and peak frequency of 6 Hz). In contrast, the horizontal resolution is about 180 m in 200 m below seafloor (using a seismic velocity and a peak frequency of 9 Hz).

3 Seismic Refraction Data

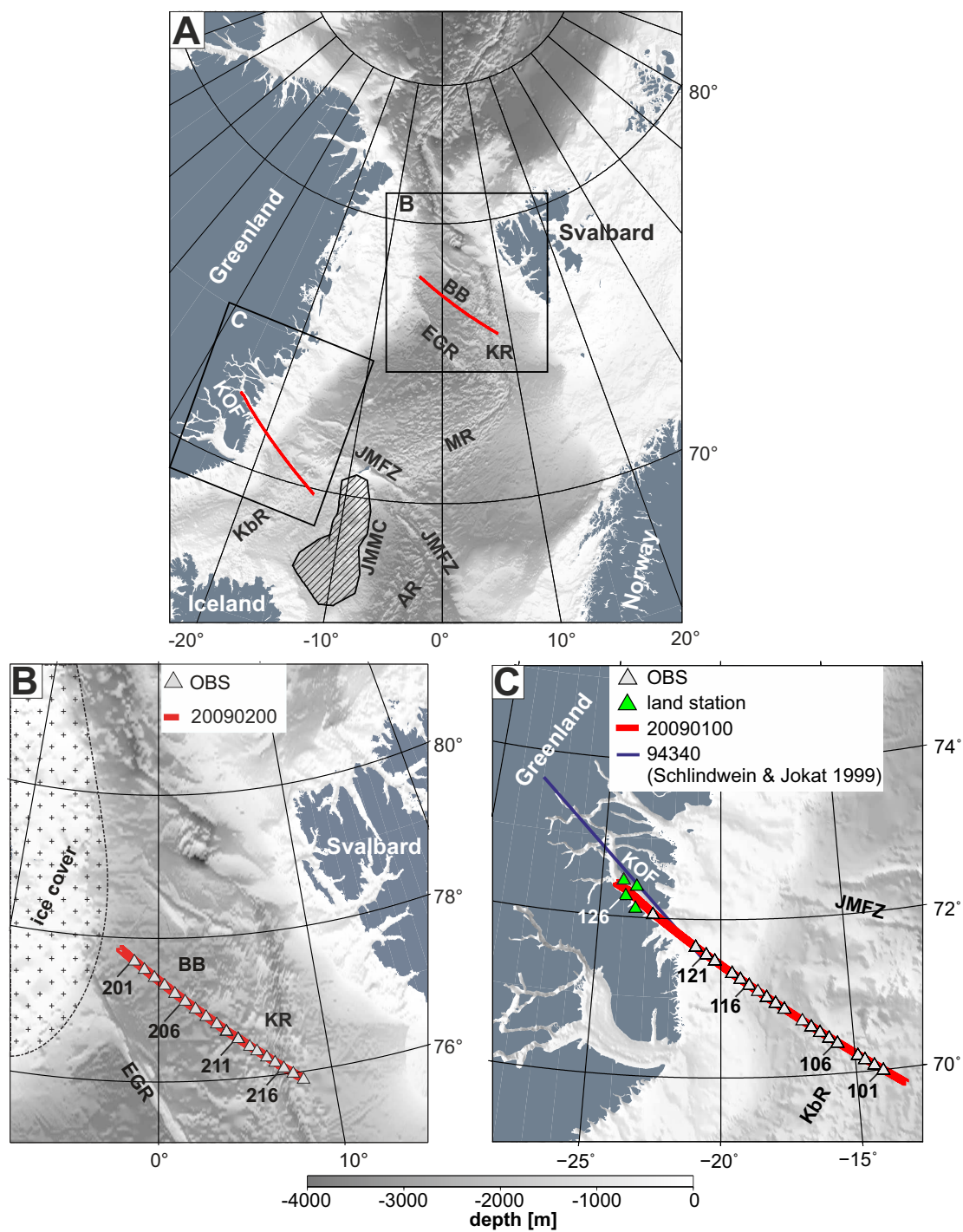


Figure 3.1: Bathymetric map (IBCAO, Jakobsson et al. 2008) showing (A) the main research area of the Northeast Greenland margin. (B) seismic refraction line 20090200 (Hermann & Jokat 2013a) and (C) seismic refraction line 20090100 (Hermann & Jokat 2013b).

Table 3.1: General specifications of the seismic refractions lines and the air gun array used during the 2009 expedition (Jokat et al. 2010).

	Line 20090200	Line 20090100
Area	Boreas Basin to Knipovich Ridge	Kong Oscar Fjord to Kolbeinsey Ridge
Length	340 km	500 km
Recording Systems	18 OBS	20 OBS 4 Land Stations
average OBS spacing	20 km	15 km
Record Length	60 s	60 s
Sample Rate	10 ms	10 ms
	Air Gun Array	
No. Air Guns	8 G-Guns	
Total Volume	66 l	
Pressure	200 bar	
Shot Interval/Distance	60 s/150 m	

3.1.2 Processing

Figure 3.2 shows the general workflow including processing, modelling and interpretation of the seismic refraction data. After acquisition, the offsets (distance between shot positions and stations) were calculated. The three seismometer and the one hydrophone channels of each OBS were demultiplexed and filtered with a band-pass filter of 4–17 Hz. Based on the narrow and shallow Kong Oscar Fjord geometry, as well as the thick sediment cover, the seismic refraction data of line 20090100 shows significant reverberations. These signals were removed (prior to demultiplexing and band-pass filtering; Fig. 3.2) using a predictive deconvolution filter (Yilmaz 2001) with an oper-

3 Seismic Refraction Data

ator length of 220 ms and a gap length of 10 ms for the deep sea stations (101–115), and an operator length of 200 ms and a gap length of 100 ms for the shelf and land stations (116–127; Fig. 3.1C). Furthermore, an automatic gain control (AGC) with a time window of 2 s was applied to all data.

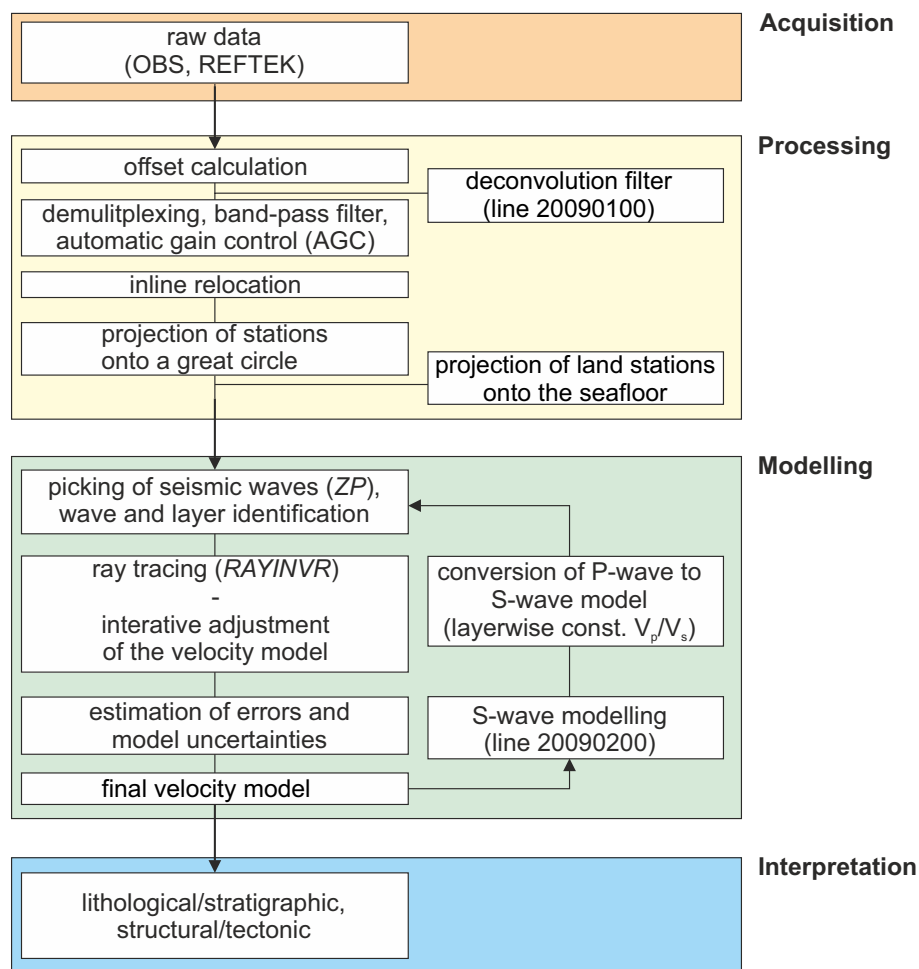


Figure 3.2: Workflow for seismic refraction data processing, modelling and interpretation of both lines 20090200 and 20090100.

Finally, the direct water waves were used to correct the in-line positions of the stations (Fig. 3.2; Schlindwein & Jokat 1999, Schmidt-Aursch & Jokat 2005a). Following the example of Schlindwein & Jokat (1999), all stations were projected onto a great circle resulting from the least square fit through the shot positions along the seismic refraction lines (Fig. 3.3A). Thereby, the offset were not modified (Schlindwein & Jokat 1999,

Schmidt-Aursch & Jokat 2005a). The land stations were additionally projected onto the seafloor and a corresponding static correction was applied (Schlindwein & Jokat 1999, Schmidt-Aursch & Jokat 2005a). The static correction is based on an average seismic P-wave velocity of 5.5 km/s for the uppermost crust and an assumed vertical ray incidence (Fig. 3.3B, Schlindwein & Jokat 1999, Schmidt-Aursch & Jokat 2005a).

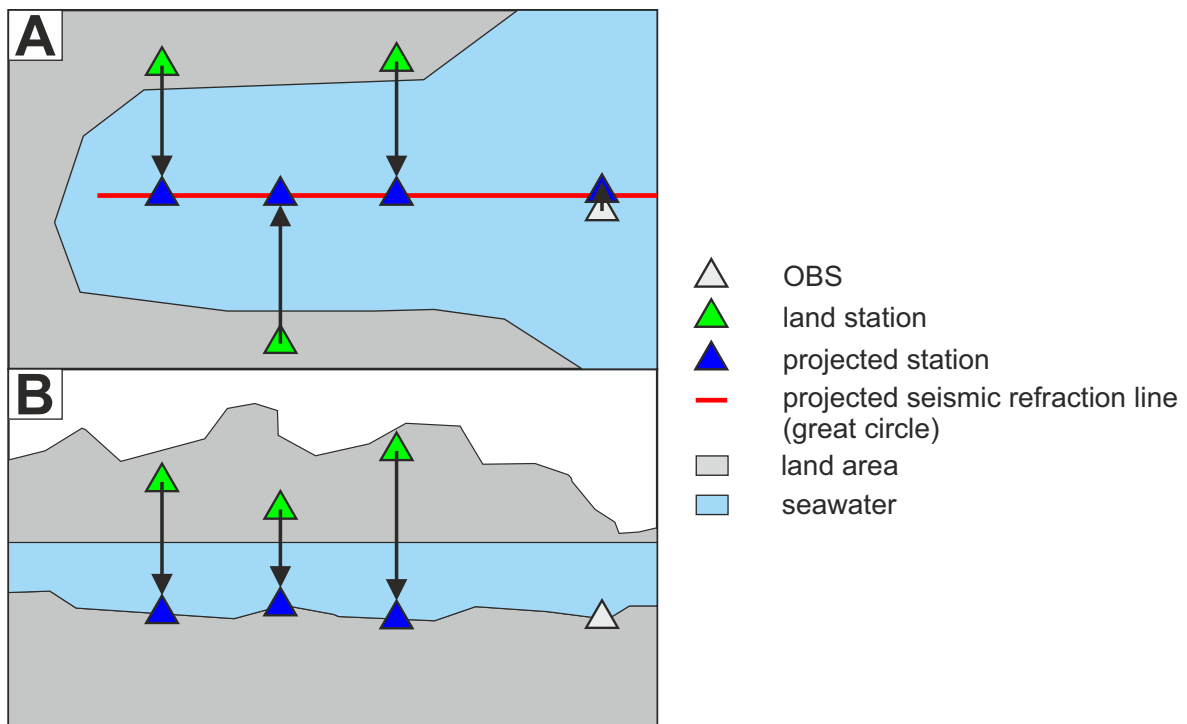


Figure 3.3: (A) Projection of land stations onto a great circle (red line) and (B) onto the seafloor.

3.1.3 Modelling

P-wave models were developed for both lines. In addition, for line 20090200 an S-wave model was calculated to substantiate the result of the P-wave model.

For the P-wave modelling the hydrophone channel of the OBS was preferred (Figs. 3.4 and 3.5; further examples see appendix A) because of a higher signal-to-noise ratio compared with the vertical seismometer component. However, the vertical seismometer component was used from land stations as well as from OBS with unusable hy-

3 Seismic Refraction Data

drophone data (Fig. 3.6). The S-wave model based on the two horizontal seismometer component data of all OBS along line 20090200 (Figs. 3.7 and 3.8; further examples see appendix A).

The picking of P- and S-waves, based on refraction and reflection waves, was done using the software package *ZP* (Fig. 3.2; Zelt 2004). Estimated pick uncertainties of seismic waves depend on the overall signal-to-noise ratio of picked seismic waves, and the decreasing signal-to-noise ratio with depth. Therefore, the pick uncertainties increase with depth (Tab. 3.2, Fig. A.4; Voss & Jokat 2007, Voss et al. 2009). For the land stations, the pick uncertainties are 100 ms larger, than these associated with the OBS data, due to it's larger off-line locations (Tab. 3.2, Fig. 3.3A).

Table 3.2: Estimated pick uncertainties of different seismic waves. The pick uncertainties are based on the signal-to-noise ratio of picked seismic waves, and the decreasing signal-to-noise ratio with depth.

Waves	Layers	Line 20090200	Line 20090100
P-waves (OBS)	Sediments	50 ms	50–60 ms
	Crust and Mantle	75–130 ms	75–130 ms
P-waves (Land Stations)	Sediments	no land stations	150–160 ms
	Crust and Mantle	no land stations	175–230 ms
S-waves (OBS)	Sediments	100 ms	not picked
	Crust and Mantle	150 ms	not picked

The P- and S-wave models were obtained by forward modelling with the 2D ray tracing software package *RAYINV*R (Fig. 3.2; Zelt & Smith 1992). Therefore, boundary conditions are necessary to reduce the multiple solutions related to seismic refraction modelling (Korenaga et al. 2000). Sediment thickness and basement topography for line 20090200 were used from seismic reflection line 20020700 running in parallel (Berger & Jokat 2009, Ehlers & Jokat 2009). Based on this, four sediment layers were included

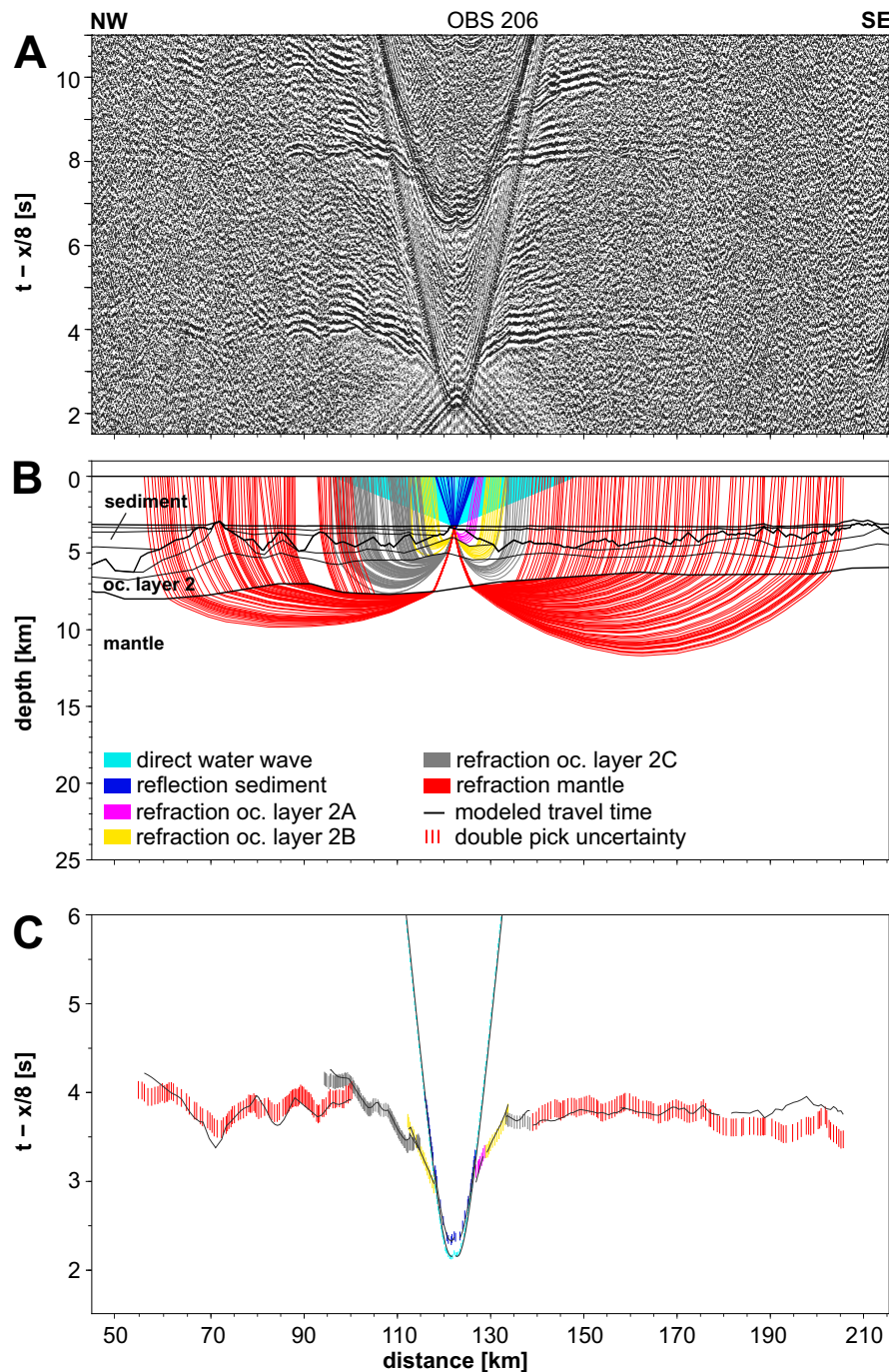


Figure 3.4: OBS data example (station 206) of line 20090200 used for the P-wave modelling. (A) Processed data of hydrophone channel, (B) modelled ray coverage, and (C) modelled and picked travel times (Hermann & Jokat 2013a). The upper and lower figure are plotted with a reduction velocity of 8 km/s. Both vertical scales are of different exaggeration. Further examples are shown in appendix A.

3 Seismic Refraction Data

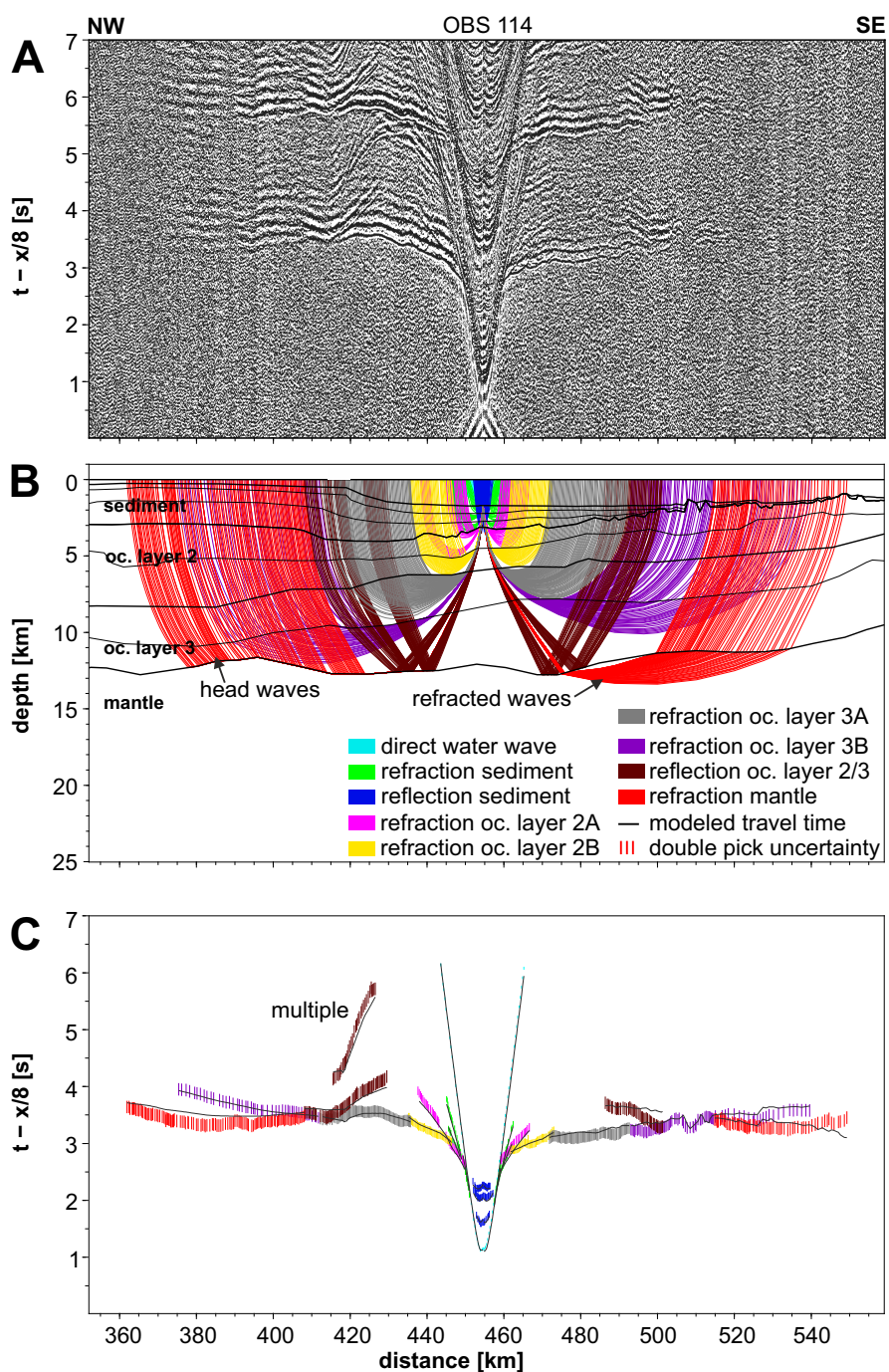


Figure 3.5: OBS data example (station 114) of line 20090100 used for the P-wave modelling. (A) Processed data of hydrophone channel, (B) modelled ray coverage, and (C) modelled and picked travel times (Hermann & Jokat 2013b). The upper and lower figure are plotted with a reduction velocity of 8 km/s. Both vertical scales are of different exaggeration. Further examples are shown in appendix A.

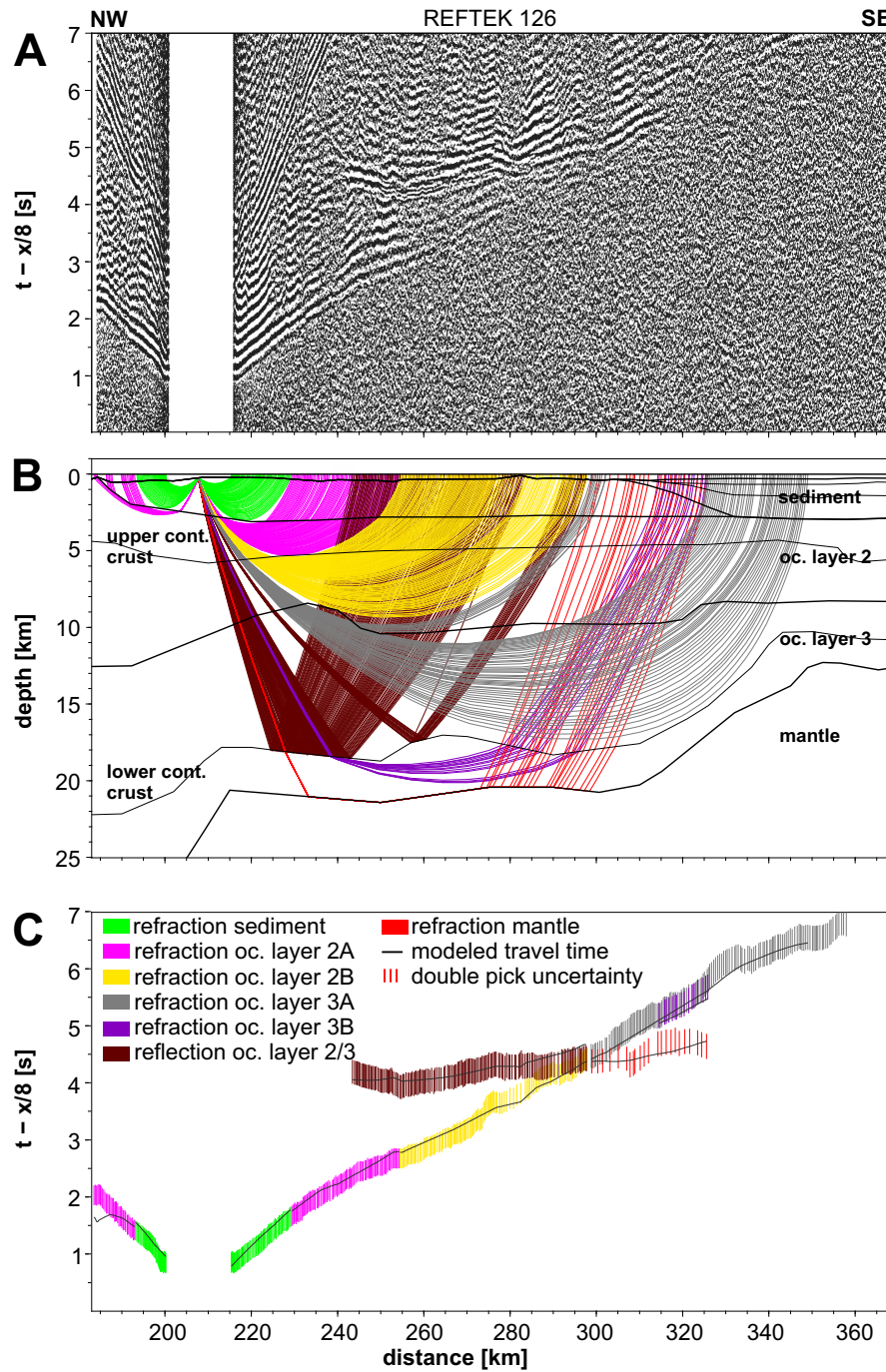


Figure 3.6: REFTEK data example (station 126) of line 20090100 used for the P-wave modelling. (A) Processed data of hydrophone channel, (B) modelled ray coverage, and (C) modelled and picked travel times (Hermann & Jokat 2013b). The upper and lower figure are plotted with a reduction velocity of 8 km/s. Both vertical scales are of different exaggeration.

3 Seismic Refraction Data

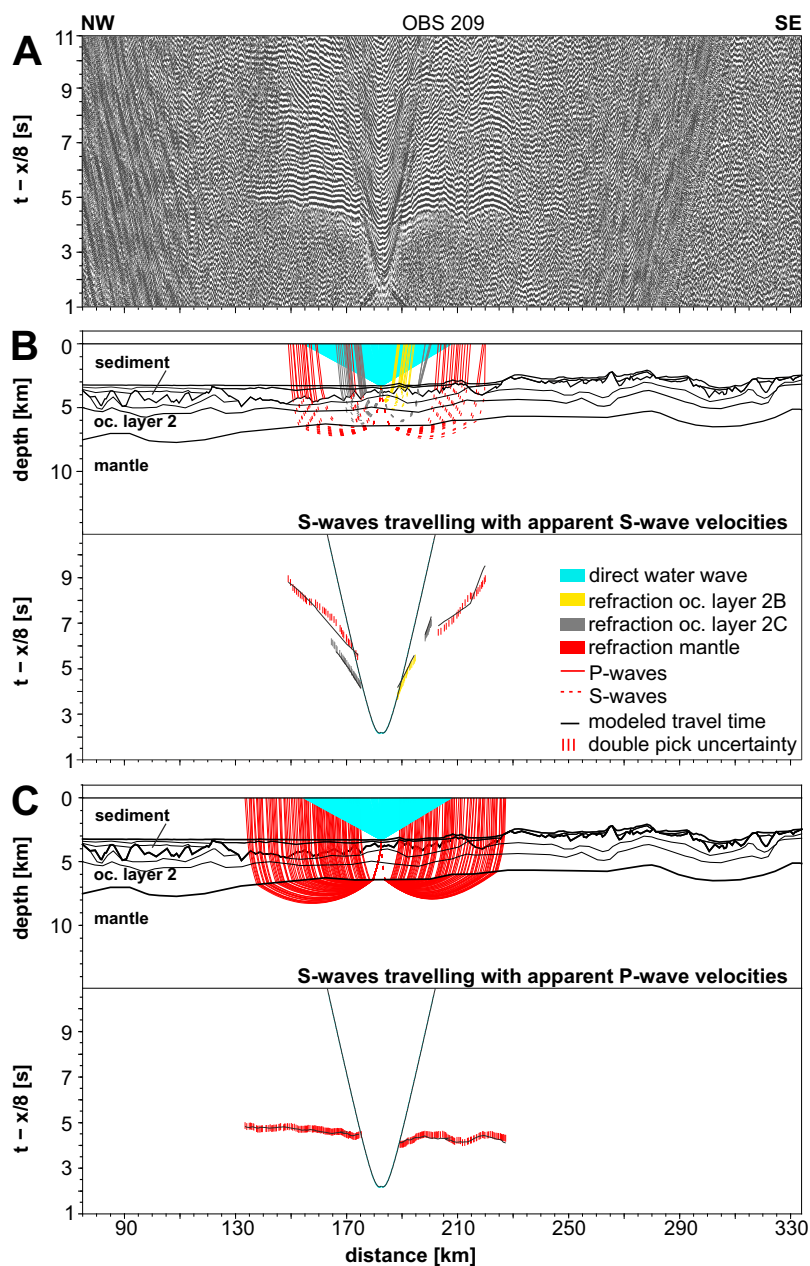


Figure 3.7: OBS data example (station 209) of line 20090200 used for the S-wave modelling. (A) Processed data of a horizontal channel, (B) S-waves travelling with apparent S-wave velocities, and (C) S-waves travelling with apparent P-wave velocities (Hermann & Jokat 2013a). Modelled ray coverage (B, C; upper panels), and modelled and picked travel times (B, C; lower panels) for both types of S-waves. Figure (A) and the lower figures of (B) and (C) are plotted with a reduction velocity of 8 km/s. The three vertical scales are of different exaggeration.

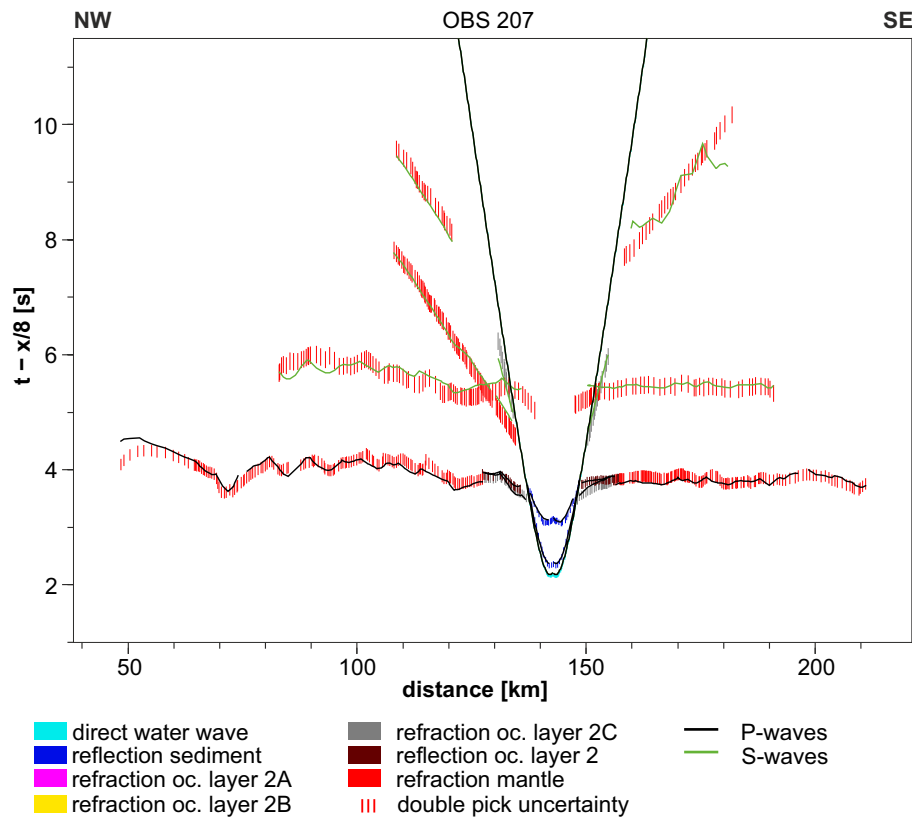


Figure 3.8: Observed and calculated P-wave as well as S-wave travel times from OBS station 207 of line 20090200 plotted with a reduction velocity of 8 km/s (Hermann & Jokat 2013a). Further examples are shown in appendix A.

in the P- and S-wave models. Furthermore, for line 20090100 the still existing P-wave model as well as its picked P-waves from the seismic refraction line 94340 (Schlindwein & Jokat 1999) were used within the overlapping area of both seismic refraction lines (Fig. 3.1C). Following Zelt (1999), the final models were obtained in layer-by-layer forward modelling, starting from the uppermost layer and keeping the velocity-depth-nodes constant when modelling the deeper layers. However, for the northwestern part of line 20090100, the refracted mantle waves could not be modelled properly (Fig. 3.5) due to sharp lateral velocity contrasts at the dipping crust-mantle boundary (Døssing et al. 2008, Voss et al. 2009). In this case, the picked P-waves were approximated by head waves, in contrast to the normally used refracted waves, along the crust-mantle boundary (Fig. 3.5). For further minimisation of the misfits between the observed and

3 Seismic Refraction Data

calculated travel times, the inversion algorithm of *RAYINV*R was applied layerwise (Fig. 3.2).

The initial S-wave model of line 20090200 was calculated by layerwise conversion of the P-wave velocities with constant V_P/V_S ratios (Fig. 3.2). Thereby, the layer boundaries of the P-wave model were used as conversion boundaries for the S-waves. Following Mjelde et al. (2002), we divided the S-wave travel time branches into: (1) S-waves travelling with apparent S-wave velocities, and (2) S-waves travelling with apparent P-wave velocities (Fig. 3.7). The P- to S-wave conversion caused by: (1) the downward travelling into the crust or (2) the upward travelling from the crust, respectively (Fig. 3.9; Mjelde et al. 2002). Therefore, different apparent velocities for the S-waves are observed (Fig. 3.7). During modelling, the V_P/V_S ratios were varied to achieve the best fit between the picked and modelled S-waves (Fig. 3.8; further examples see appendix A) while the layer boundaries from the P-wave model were kept constant.

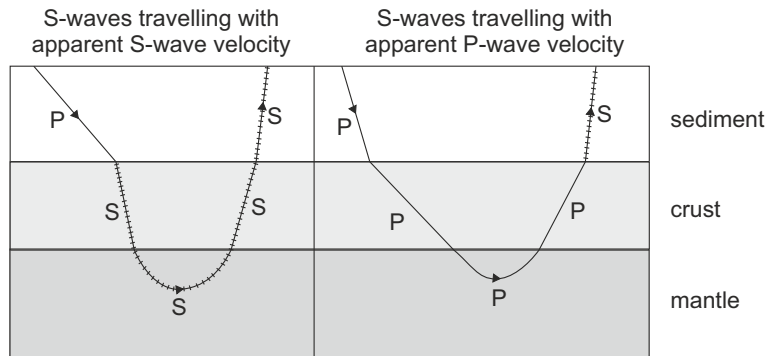


Figure 3.9: Origin of two types of S-waves caused by P- to S-wave conversion at a layer boundary.

3.1.4 Error Analysis

The significance of the P-wave models were calculated using the normalised χ^2 method and the residual time t_{RMS} (Zelt & Smith 1992). The χ^2 method weights the mismatch between the observed and calculated travel times. The χ^2 value is defined by the following equation

$$\chi^2 = \frac{1}{n} \sum_{i=1}^n \left(\frac{T_{oi} - T_{ci}}{U_i} \right)^2 \quad (3.1)$$

with T_o – observed travel time, T_c – calculated travel time, U – estimated pick uncertainty, and n – number of picks for different layers. The optimised value of a normalised χ^2 is 1.0 meaning a nearly perfect fit between the observed and calculated travel times (Zelt & Smith 1992). For $\chi^2 > 1.0$ small scale velocity anomalies and boundary topographies could not be modelled. In contrast, for $\chi^2 < 1.0$ the model suggest a higher resolution than it is possible using the acquired data.

Following Schlindwein & Jokat (1999), the model uncertainties were estimated by model perturbations of single boundary and velocity nodes until the calculated travel times are not within the uncertainty of the observed travel times. These model perturbations were carried out for a node interval of 50 km.

The resolutions of the P-wave models were calculated using an inversion method (Zelt & Smith 1992), which represents a quantitative description of model reliability. Therefore, the maximum uncertainties of the models were used. Resolution values greater than 0.5 indicate reasonably well resolved model parameters (Zelt & Smith 1992). In contrast, resolution values smaller than 0.5 describe a low ray covered model.

The significance of the S-wave model, χ^2 and t_{RMS} , was calculated like the significance of the P-wave models. The uncertainties of the S-wave model, including S-wave velocity and V_P/V_S ratio, were estimated as explained for the P-wave models.

3.2 Line Boras Basin – Knipovich Ridge (20090200)

The following results of line 20090200 as well as the interpretation of the crustal and upper mantle structures of the Boreas Basin and the Knipovich Ridge are published by Hermann & Jokat (2013a).

3.2.1 P- and S-wave Models

The P- and S-wave models have a length of 340 km. The results of S-wave modelling are displayed within the P-wave model by adding V_P/V_S ratios (Fig. 3.10). For the description and the interpretation of oceanic crust the classification of Juteau & Maury (1999) was used (Tab. 2.1).

Sediments

The models consist of four sediment layers with a total thickness of about 0.2 km. In general, the sediment P-wave velocities range between 1.6 km/s and 3.5 km/s (Fig. 3.10). The V_P/V_S ratio varies between 6.06 and 2.95.

Along our seismic refraction line, three sediment basins are observed (Fig. 3.10): (1) from 0 km to 60 km with a sediment thickness of 3 km, (2) from 80 km to 120 km with a sediment thickness of 1 km, and (3) from 130 km to 190 km with a sediment thickness of 1 km. Within these basins, in a depth interval of 200 m to 500 m, the P-wave velocities significantly increase from 2.2 km/s to 2.7 km/s (Fig. 3.10), and the V_P/V_S ratio decrease from 5 to 4. Berger & Jokat (2009) report a high-impedance contrast at the same depth interval along their seismic reflection line 20020700. This depth interval was dated to Mid Miocene age (~ 13 Ma; Fig. 3.11). Sediments above the depth interval can be described as poorly consolidated deep-sea sediments with high porosity and reduced lithification (Mjelde et al. 2002, Ljones et al. 2004). Sediments below the Mid Miocene interval might be more consolidated deep-sea sediments characterised by a decreasing V_P/V_S ratio with depth (Domenico 1984, Ljones et al. 2004).

Crust

Our models consist of three crustal layers with a total thickness of about 3.2 km (Fig. 3.10). This crustal thickness is well constrained by refracted and reflected waves from the crust-mantle boundary, especially by reflected waves in the northwestern part of line 20090200 (Figs. 3.10 and 3.12B). Below a seamount at 70 km (Fig. 3.10), the crust has its maximum thickness of 4 km. Close to the Northeast Greenland Shelf (20–60 km, Fig. 3.10), the minimum crustal thickness of 1.4 km was found. The crustal P-wave velocities range between 3.4 km/s and 6.3 km/s.

The crust is of oceanic origin and the oceanic layers 2A, 2B and 2C can be distinguished (Fig. 3.11, Tab. 2.1). Oceanic layer 2A has a thickness of approximately 0.6 km. In particular, between 60–130 km and 220–310 km the thickness of oceanic layer 2A is significantly increased by 0.4 km and highly variable (0.4–1.2 km thickness, Fig. 3.11). The P-wave velocities are between 3.4 km/s and 4.3 km/s (Fig. 3.10). From the Knipovich Ridge rift valley to the Northeast Greenland Shelf, the P-wave velocities increase by about 1 km/s, from 3.5 km/s to 4.2 km/s, respectively. The average V_P/V_S ratio is 1.73 decreasing with distance to the rift valley (1.81) and reaches 1.63 below the seamount (Fig. 3.10).

Interpreting our results, the variations in thickness of oceanic layer 2A might be the result of a variable amount of extrusive rocks and volcanism during the formation of oceanic crust (Klingelhöfer et al. 2000). Within the two distinct locations (60–130 km, 220–310 km), the magmatic activity was probably higher than throughout the rest of seismic refraction line 20090200 (Fig. 3.11). In general, the increasing P-wave velocities and the decreasing V_P/V_S ratios from the Knipovich Ridge to the Boreas Basin point towards small cracks, fissures and voids in pillow lava filled with secondary hydrothermal minerals (Grevemeyer & Weigel 1996, Ljones et al. 2004).

Oceanic layer 2B has the same thickness like oceanic layer 2A (0.6 km). However, the P-wave velocities are higher and range from 4.5 km/s to 5.2 km/s (Fig. 3.10). Below the rift valley, the P-wave velocities decrease to 3.0 km/s and below the seamount they increase to 5.4 km/s. The average V_P/V_S ratio is 1.72. Below the Knipovich Ridge

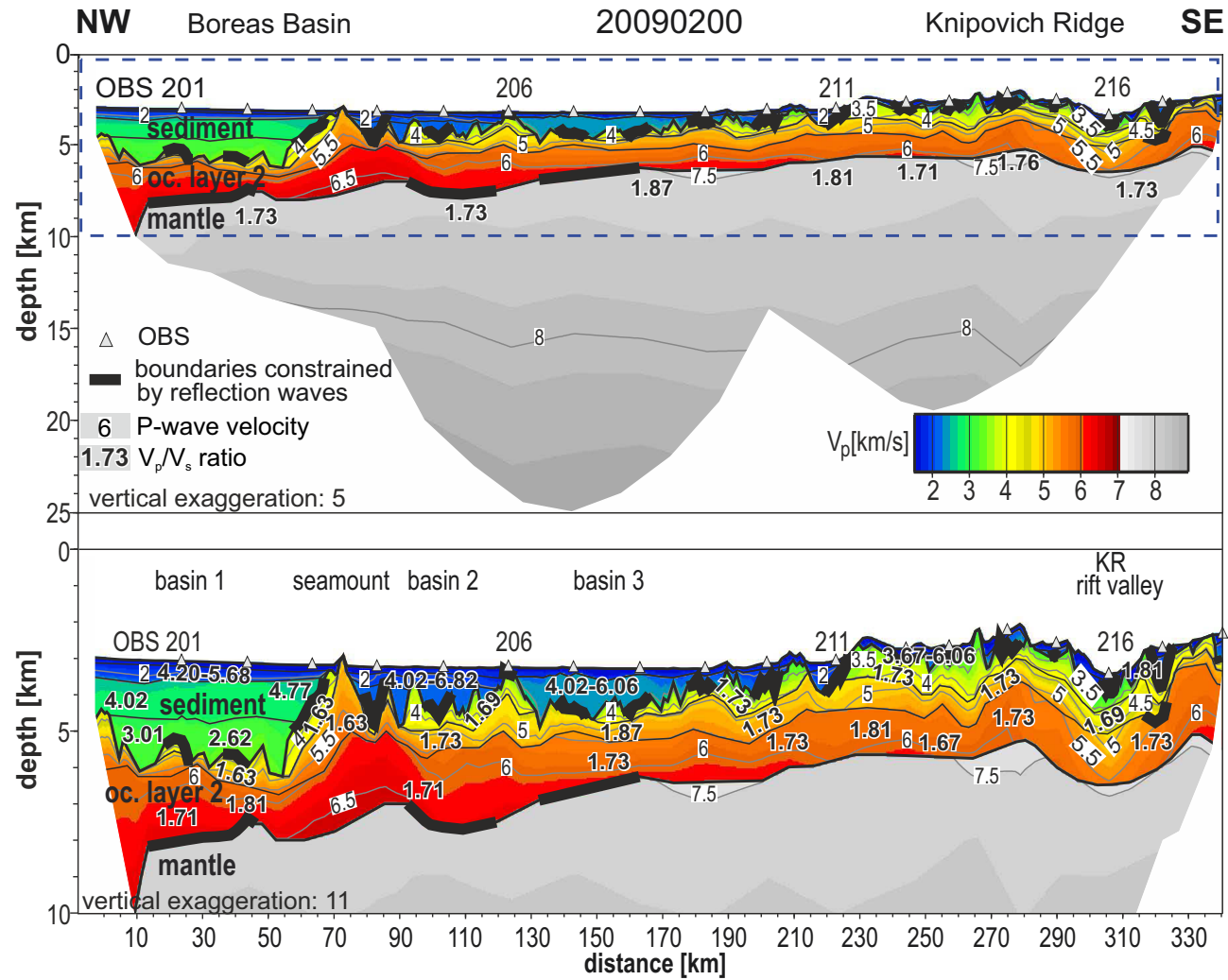


Figure 3.10: P- and S-wave model of line 20090200 (Hermann & Jokat 2013a). The lower panel shows an enlarged detail of the upper 10 km, which is marked by the blue dashed rectangle in the upper panel.

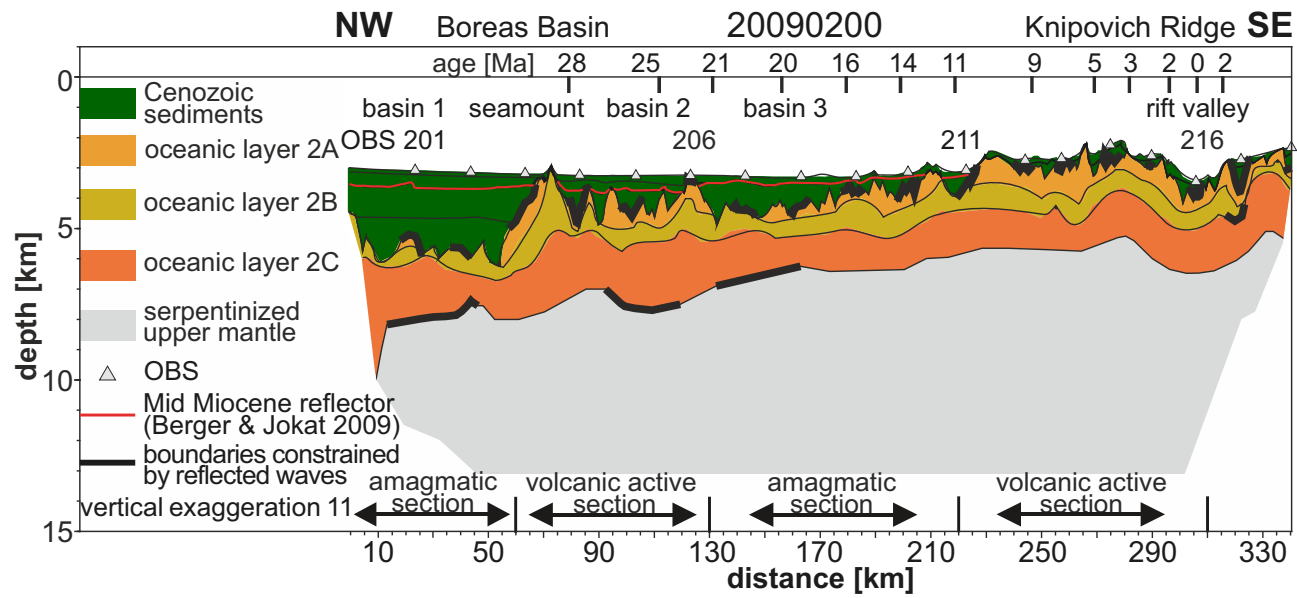


Figure 3.11: Interpretation of line 20090200 (Hermann & Jokat 2013a). Ages of the oceanic crust according to Ehlers & Jokat (2009).

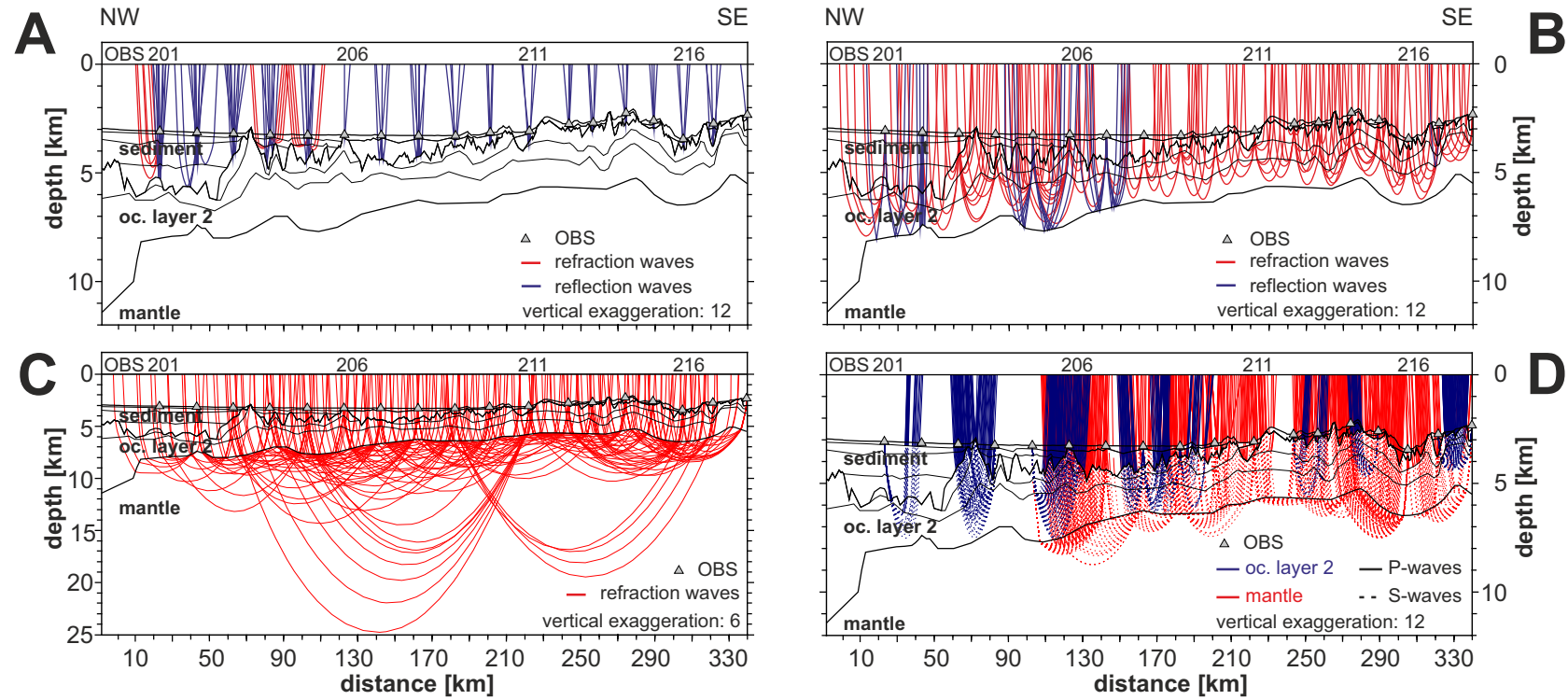


Figure 3.12: Ray coverage of the P-wave model for: (A) sediments, (B) oceanic layer 2, and (C) upper mantle. (D) shows the ray coverage of converted S-waves travelling with apparent S-wave velocities (Hermann & Jokat 2013a). Figure (C) is plotted with different vertical exaggeration.

rift valley and the seamount the V_P/V_S ratio is 1.69 and 1.63, respectively (Fig. 3.10). These results indicate that oceanic layer 2B represents the transition from extrusive pillow lava to sheeted dykes (Tab. 2.1; Klingelhöfer et al. 2000).

Oceanic layer 2C has a thickness of about 2 km and the P-wave velocities vary between 5.7 km/s and 6.3 km/s (Fig. 3.10). From the Knipovich Ridge rift valley to the Northeast Greenland margin, the P-wave velocities increase by 0.5 km/s. Below the Knipovich Ridge rift valley, the P-wave velocities decrease to 5.2 km/s and below the seamount they increased to 6.7 km/s (Fig. 3.10). The average V_P/V_S ratio of oceanic layer 2C is 1.73. At 40 km, where the crust is thinnest, the V_P/V_S ratio reaches the maximum value of 1.81.

Focusing on our interpretation, the low sedimentary and crustal P-wave velocities below the Knipovich Ridge rift valley were most likely caused by deep reaching cracks and faults. Along these faults, oceanic water possibly migrated downward to the crust-mantle boundary, modifying the physical properties and P-wave velocities of the rocks (Kodaira et al. 1997).

In general, oceanic layer 3 has a thickness of 4 km and typical P-wave velocities of 6.5 km/s to 7.5 km/s (Tab. 2.1, Juteau & Maury 1999). However, we could not observe oceanic layer 3 in our seismic refraction data due to the absence of typical oceanic layer 3 P-wave velocities (Figs. 3.10 and 3.13).

Upper Mantle

The upper mantle shows P-wave velocities with small lateral variations (Fig. 3.10). The P-wave velocities vary between 7.5 km/s, directly below the crust-mantle boundary, and 8.0 km/s, in approximately 15 km depth below sea level. The average V_P/V_S ratio is 1.74 (Fig. 3.10). Large deviations of the V_P/V_S ratio are found at 170 km and 280 km with values of 1.87 and 1.76, respectively.

Following our interpretation, the P-wave velocities are low, compared with global upper mantle studies ($V_P > 7.9$ km/s, $V_P/V_S \sim 1.84$, Christensen 1996). In addition, the partially low V_P/V_S ratios indicate a serpentinised mantle (Fig. 3.11; Horen et al.

3 Seismic Refraction Data

1996, Christensen 2004). Following Horen et al. (1996), a P-wave velocity of 7.5 km/s equates to a mantle serpentinisation of approximately 13%, which becomes negligible at about 15 km below sea level, where mantle velocities reach 8.0 km/s (Fig. 3.10). The serpentinisation of the normal mantle material (peridotite) maybe occurred due to oceanic water which reached the mantle by migration from the seafloor along faults and cracks (Horen et al. 1996, Christensen 2004).

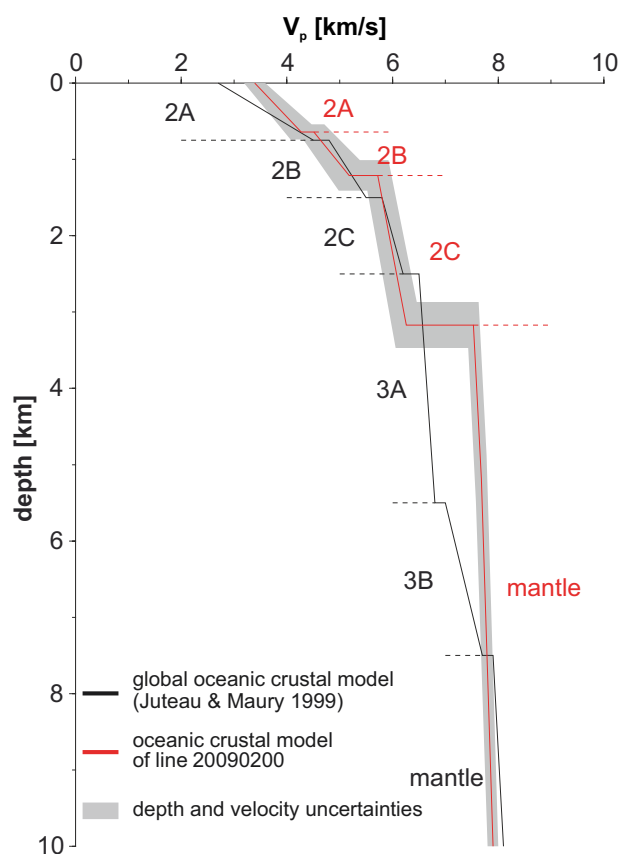


Figure 3.13: One-dimensional (1D) crustal P-wave velocity model of line 20090200 (red line, Hermann & Jokat 2013a). The black line represents P-wave velocities from global oceanic crust (Tab. 2.1, Juteau & Maury 1999). The comparison of both curves shows the absence of oceanic layer 3 in our seismic refraction model.

3.2.2 Error Analysis

The significance of the P-wave model resulted in a χ^2 value of 1.557 and a t_{RMS} value of 0.114 s (Tab. 3.3). Approximately 97% of 6627 observed P-wave picks could be ray traced. The uncertainty of P-wave velocities were estimated with ± 0.2 km/s for sediments and crustal layers, and ± 0.1 km/s for the uppermost mantle. These low uncertainties for mantle velocities are a consequence of good ray coverage of the uppermost mantle (Figs. 3.12C). Depth uncertainties of the boundaries are ± 0.1 km for the sediments, ± 0.2 km for the crustal layers and ± 0.3 km for the crust-mantle boundary (Fig. 3.13).

Table 3.3: Statistical significance of the P- and S-wave models (χ^2) based on the numbers of observed travel time picks (n) for different layers. The residual time t_{RMS} represents the misfit between observed and calculated travel times.

	Layer	n	t_{RMS} [s]	χ^2
P-waves	Sediment	1194	0.046	0.816
	Oceanic Layer 2	1692	0.076	1.063
	Mantle	3741	0.141	2.016
	All	6627	0.114	1.557
S-waves	Sediment	359	0.128	0.774
	Oceanic Layer 2	996	0.133	0.812
	Mantle	2412	0.151	1.024
	All	3767	0.143	0.945

Using the maximum uncertainty values of 0.2 km/s and 0.3 km, the resolution of the P-wave model was calculated (Fig. 3.14). The P-wave velocities are generally well resolved (0.50–1.00). However, two locations of poor resolution (0.03–0.49) are observed (Fig. 3.14): (1) 100 km to 200 km for the sediments and oceanic layer 2A, and (2) below basin 1 (0–60 km) for the crustal layers and the upper mantle. The poor resolution

3 Seismic Refraction Data

between 100 km and 200 km was caused by insufficient refracted signals from oceanic layer 2A due to recordings of only five OBS (203, 206, 212, 213 and 217, Figs. 3.4 and A.5). Below basin 1, the poor resolution was caused by the locally low ray coverage of the crust and upper mantle (Figs. 3.12B, C).

For the significance of the S-wave model, χ^2 was calculated with 0.909 and t_{RMS} with 0.143 s (Tab. 3.3). Approximately 96% of the 3767 observed S-wave picks could be ray traced. The uncertainties of the S-wave model were the same as for the P-wave model. The uncertainty of the V_P/V_S ratio was estimated with 0.05 in areas of high ray coverage and 0.12 in areas of low ray coverage (Fig. 3.12D).

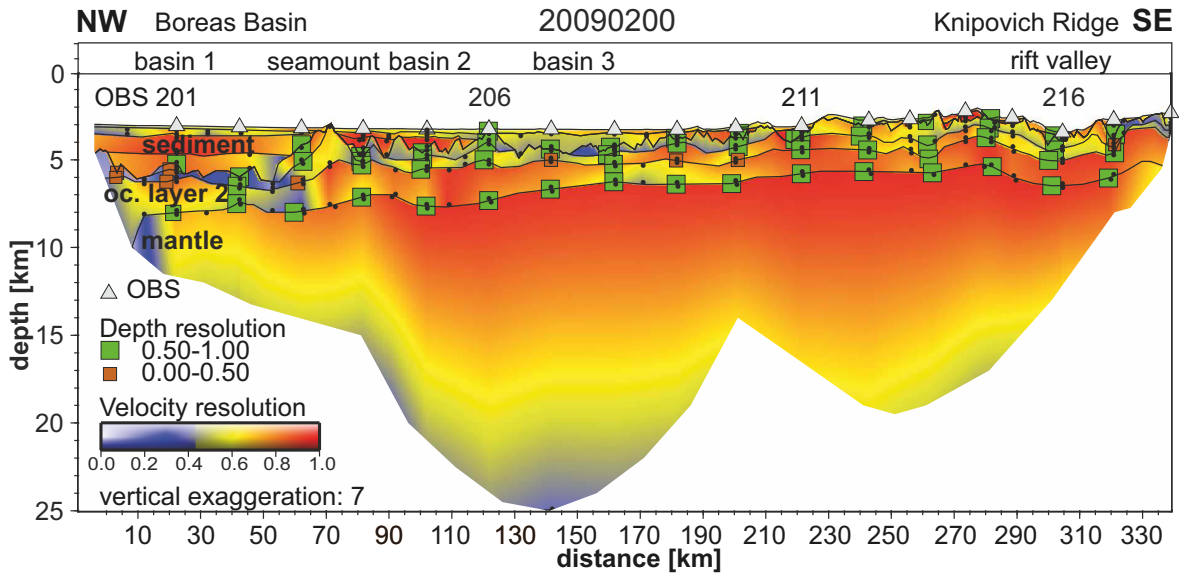


Figure 3.14: Resolution plot of line 20090200 (Hermann & Jokat 2013a). The black dots mark the positions of the nodes which were used for the calculation of the velocity resolutions.

3.2.3 Discussion of Line 20090200

Crustal and Upper Mantle Variations in Boreas Basin and across Knipovich Ridge

Line 20090200 is the only available seismic refraction line which crosses the Boreas Basin and the Knipovich Ridge, parallel to its spreading direction (Fig. 3.1B). Additional seismic refraction lines are located at the southern boundary of the Boreas Basin

to the East Greenland Ridge (Fig. 2.2; Døssing et al. 2008) and east of the Knipovich Ridge towards Svalbard (Fig. 3.15; Ritzmann et al. 2002, Ljones et al. 2004, Kandilarov et al. 2008, 2010, Jokat et al. 2012a).

Regarding the sediments, the P- and S-wave models show a thin sediment cover in the area of the Knipovich Ridge rift valley (Fig. 3.11). In contrast, within the three sediment basins (Fig. 3.11), the thick sediments are divided by the Mid Miocene reflector into two sublayers (Berger & Jokat 2009). The P-wave velocity contrast at the Mid Miocene reflector (2.2 to 2.7 km/s, Fig. 3.10) was also modelled by Døssing et al. (2008) for the southern part of the Boreas Basin. Similar P-wave velocity contrasts have also been reported along four seismic refraction lines east of the Knipovich Ridge (Fig. 3.15; Ritzmann et al. 2002, Ljones et al. 2004, Kandilarov et al. 2008, 2010). Here, Ljones et al. (2004) modelled V_P/V_S ratios between 7.14 and 2.00 for the upper sediments, and between 1.87 and 1.78 for the lowermost sediments. These values are interpreted to represent high-porosity muddy sediments at the seafloor, and a mixture of sand and shale for the lowermost units (Ljones et al. 2004). However, we modelled different V_P/V_S ratios in the Boreas Basin for the lower sediments (4.02–2.62, Fig. 3.10). Thus, the deposition of more fine-grained clay sediments is more likely to have taken place rather than sandy sediments (Berger & Jokat 2009).

The oceanic crustal structure west of Knipovich Ridge is comparable with observations at other ultraslow spreading ridges (e.g. Jokat & Schmidt-Aursch 2007). Along our line 20090200, the data quality allows to divide oceanic layer 2 into three sublayers (2A, 2B, and 2C). In five OBS records (203, 206, 212, 213, 217) three distinct refracted travel time branches support the existence of the three sublayers (Figs. 3.4 and A.5). The P-wave velocities as well as the thickness of the three layers correspond well to general classifications of oceanic layers (Tab. 2.1, Fig. 3.13; Juteau & Maury 1999). In contrast to our results, Døssing et al. (2008) modelled one crustal layer in the Boreas Basin because of limited ray coverage, since only one OBS was placed in the Boreas Basin close to the East Greenland Ridge (Tab. 3.4).

3 Seismic Refraction Data

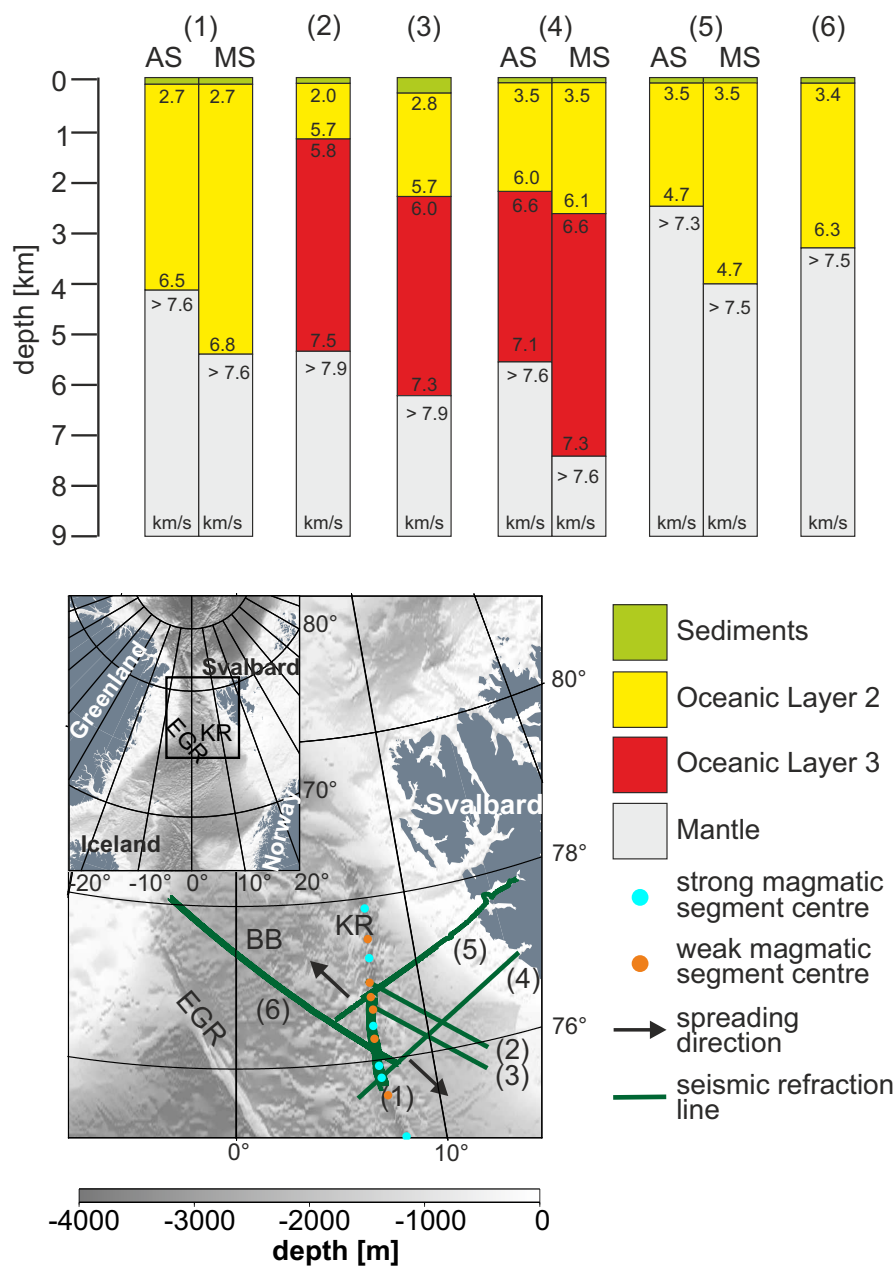


Figure 3.15: Crustal and upper mantle structures with average layer thicknesses and P-wave velocities of several seismic refraction lines across the Knipovich Ridge (Hermann & Jokat 2013a): (1) Jokat et al. (2012a), (2 and 3) Kandilarov et al. (2008, 2010), (4) Ljones et al. (2004), (5) Ritzmann et al. (2002), and (6) line 20090200 (Hermann & Jokat 2013a). If seismic refraction lines cross segment boundaries two 1D columns – amagmatic (AS) and magmatic segments (MS) – are shown. The magmatic segment centres are after Okino et al. (2002) and the spreading direction is from DeMets et al. (1990).

Along the Knipovich Ridge, Ljones et al. (2004), Kandilarov et al. (2008, 2010) and Jokat et al. (2012a) favour the subdivision of oceanic crust into two sublayers (Tab. 3.4). Our P-wave velocities and layer thicknesses do not contradict these results, as our oceanic layers 2A and 2B can be merged because of their similar velocity gradients and thicknesses (Fig. 3.13). Finally, Ritzmann et al. (2002) modelled one crustal layer (Tab. 3.4). Again, the large receiver spacing (30–50 km) along their seismic refraction line did not allow the subdivision of oceanic crust due to low resolution.

Table 3.4: Comparison of various published seismic refraction lines across the ultraslow spreading Knipovich Ridge. Crustal P-wave velocities (V_P), crustal thicknesses (Crust. Thick.), numbers of modelled sublayers of oceanic layer 2 as well as the P-wave velocities of the upper mantle are provided.

Author	Crust. Thick. [km]	V_P Layer 2 [km/s]	Sublayers Layer 2	V_P Layer 3 [km/s]	V_P Mantle [km/s]
Jokat et al. (2012a)	4.5	2.7–6.6	2	not observed	7.6
Kandilarov et al. (2008)	5.4	2.0–5.8	2	5.7–7.5	6.4–7.9
Kandilarov et al. (2010)	6.2	2.8–5.7	2	6.0–7.3	6.7–8.0
Ljones et al. (2004)	6.7	3.5–6.1	2	6.6–7.3	7.6–8.0
Ritzmann et al. (2002)	3.5	3.5–4.7	1	not observed	7.3–8.2
Line 20090200	3.2	3.4–6.3	3	not observed	7.5–7.6

In the upper mantle, consistently low seismic velocities of less than 7.9 km/s were observed, which might indicate a serpentinisation of the upper mantle of 13% maximum (Horen et al. 1996). This result we compared with the recording of a single OBS close to the East Greenland Ridge (Døssing et al. 2008). Based on this single, non-reversed short OBS-recording (30 km offset range into Boreas Basin), mantle velocities of 7.9 km/s to 8.0 km/s could be modelled. Thus, these data provide little control on the upper mantle velocities. Our model relies on 15 OBS in the centre of the Boreas Basin and, therefore, provides reliable seismic velocities for the mantle below the Boreas Basin. Along the Knipovich Ridge, low upper mantle velocities were identified (Fig. 3.15,

3 Seismic Refraction Data

Tab. 3.4). As it is an active mid-ocean spreading centre, the reduced upper mantle velocities might be caused by a warmer upper mantle as well as by serpentinisation of upper mantle rocks (Ritzmann et al. 2002, Ljones et al. 2004, Kandilarov et al. 2008, 2010, Jokat et al. 2012a). Following Ritzmann et al. (2002) and Jokat et al. (2012a), the serpentinisation of the upper mantle is 15% to 20% maximum.

Absence of Oceanic Layer 3

Along line 20090200, P-wave velocities of less than 6.3 km/s were modelled throughout the oceanic crust. Higher seismic velocities of 6.7 km/s could only be identified below the seamount at 70 km (Fig. 3.10). These P-wave velocity values are not typical for oceanic layer 3 (6.6–7.5 km/s, Tab. 2.1; Juteau & Maury 1999). In general, V_P/V_S ratios of oceanic layer 3 are between 1.78 and 1.91 (Holbrook et al. 1992). However, for the seismic refraction line, crustal V_P/V_S ratios vary between 1.63 and 1.87 (Fig. 3.10). The seismic refraction line of Døssing et al. (2008), in the vicinity of the Boreas Basin, also show the absence of oceanic layer 3. However, their northernmost OBS is located on the East Greenland Ridge, not in the Boreas Basin. Therefore, they could not model the crustal structure of the Boreas Basin well. Summarising our results, there is little doubt that the Boreas Basin and the Knipovich Ridge shows a general absence of oceanic layer 3.

Further seismic refraction lines east of the Knipovich Ridge, close to the Barents Sea and across the West Svalbard continental margin, provide contrasting models for the lower oceanic crust (Fig. 3.15, Tab. 3.4). Ljones et al. (2004) modelled an oceanic layer 3 with seismic velocities between 6.6 km/s and 7.3 km/s (Fig. 3.15, Tab. 3.4). The oceanic crust is thick (up to 6.7 km) compared with a normal crust of an ultraslow spreading ridge (~ 3.5 km, Fig. 3.15, Tab. 3.4). Kandilarov et al. (2008, 2010) calculated thinner oceanic crust (5.4–6.2 km) with seismic velocities higher than 6.6 km/s, which was interpreted as oceanic layer 3 (Fig. 3.15). In contrast, 80 km north of line 20090200, Ritzmann et al. (2002) did not find any evidence for the presence of an oceanic layer 3. This is valid for the OBS recordings close to the Knipovich Ridge as well as in the Boras

Basin and the small basin east of Knipovich Ridge (Fig. 3.15). Finally, the seismic refraction line along the Knipovich rift valley (Jokat et al. 2012a) shows no evidence for an oceanic layer 3 (Fig. 3.15), despite of a smooth basement topography and several OBS along the line.

Hypothetically, an average crustal thickness of 3 km would imply a thickness of 0.5 km to 1.0 km for oceanic layer 3 (Juteau & Maury 1999, White et al. 1992). The uncertainty of our P-wave model is better than 0.3 km, which would resolve an expected oceanic layer 3 in our seismic refraction data. However, there are no distinctive indications in our data that would support the existence of oceanic layer 3 (Figs. 3.10). It could also be argued that the rough basement topography, as shown in our seismic refraction line, might cause problems for the identification of reflection and refraction waves from oceanic layer 3. But Jokat et al. (2012a) and Ritzmann et al. (2002) also did not interpret the existence of an oceanic layer 3 from their seismic refraction lines from the Knipovich Ridge, including a smoother basement topography (Fig. 3.15).

The differences, whether an oceanic layer 3 exists at ultraslow spreading ridges or not, can be explained by segmentation of the crust. Therefore, the crustal structure in basins, which were formed along ultraslow spreading ridges, is more heterogeneous than the existing seismic refraction lines indicate, and the identification of oceanic layer 3 depends on the location and configuration (station spacing, line orientation) of the seismic refraction line.

In general, segmentation along the rift valley of ultraslow spreading ridges leads to the formation of magmatic and amagmatic segments (Okino et al. 2002, Michael et al. 2003). Magmatic segments are characterised by high productivity magmatic centres producing a thick crust, including oceanic layer 3. Melt is delivered from magmatic segments by lateral dyke propagation to otherwise magmatically starved, amagmatic segments (Minshull et al. 2006). Therefore, the oceanic crust of amagmatic segments is thin and oceanic layer 3 is generally absent (Jokat et al. 2003). Furthermore, lateral melt propagation also causes a rough basement topography (Klingelhöfer et al. 2000). For the Knipovich Ridge an interpretation is difficult, because of currently unknown

3 Seismic Refraction Data

position stability of magmatic and amagmatic segments along the Knipovich Ridge rift valley in geological times (Fig. 3.15; Okino et al. 2002).

Seismic refraction lines running in parallel to the spreading direction of the Knipovich Ridge are from Kandilarov et al. (2008, 2010) and line 20090200 by this study (Fig. 3.15). Using the interpretation of Okino et al. (2002), concerning the distribution of magmatic and amagmatic centres along the present-day Knipovich Ridge rift valley, the seismic refraction lines of Kandilarov et al. (2008, 2010) might obliquely cross magmatic segments or might run in parallel to the spreading direction along the track of a long-lived magmatic centre. Here, the higher magmatic activity has produced an oceanic layer 3 (Fig. 3.15) and explain the rather homogeneous crust. However, the large station spacing (20–35 km) did not allow a more detailed interpretation. On the other hand, seismic refraction line 20090200 did not cross any magmatic centre. Therefore, it shows only information about the amagmatic part of the Boreas Basin. In this context, the seismic refraction lines of Ritzmann et al. (2002) and Ljones et al. (2004) – acquired to understand the crustal structure of the continent-ocean transition zone of Western Svalbard – run obliquely to the spreading direction and across segment boundaries. They contain crustal information about magmatic and amagmatic segments (Fig. 3.15). While Ljones et al. (2004) report a significant variability of the oceanic crust with thicknesses up to 6.7 km, created most likely along an amagmatic centre, Ritzmann et al. (2002) did not mention such variations. Along the line of Ritzmann et al. (2002), between the Western Svalbard continent-ocean transition zone and the Boreas Basin, they identified consistently thin oceanic crust (1.5–4.0 km, Fig. 3.15). The low resolution due to large station spacing (30–50 km, Ritzmann et al. 2002) and rough basement topography (Ljones et al. 2004) did not allow to model the small differences between magmatic and amagmatic segments along both seismic refraction lines.

Finally, along the Knipovich Ridge rift valley, variations in crustal P-wave velocities (2.7–6.6 km/s, 2.7–6.9 km/s) and crustal thicknesses (3.4–5.7 km) between the particular segments were found (Fig. 3.15; Jokat et al. 2012a). P-wave velocities above

6.6 km/s, typical for oceanic layer 3, are only observed below the magmatic segments (Jokat et al. 2012a).

Variations of Magmatic Production along Knipovich Ridge

In general, at ultraslow spreading ridges the oceanic spreading and the evolution of thicker crust with rough basement topography are concentrated on local magmatic centres which are highly variable in time and location (e. g. Okino et al. 2002, Jokat et al. 2003, Jokat & Schmidt-Aursch 2007). These variations are caused by pulse-like episodic magma injections from the mantle (Tolstoy et al. 2001). At amagmatic centres, the absence of oceanic layer 3 was reported by e.g. Ritzmann et al. (2002) and Jokat et al. (2012a).

Using this model, we could identify magmatic and amagmatic sections in the Boreas Basin along our seismic refraction line 20090200. Following Klingelhöfer et al. (2000), the basement roughness and the thickness of oceanic layer 2A correlate with the magmatic activity along mid-ocean ridges. We identified two magmatic sections with rough basement topography and a thick oceanic layer 2A between 60 km to 130 km, including the seamount, and 220 km to 310 km (Fig. 3.11). According to the age model of Ehlers & Jokat (2009, Fig. 3.11), the magmatic active sections date back to >28 Ma – 21 Ma and 11 Ma – 0 Ma, respectively. In contrast, two areas with smooth basement topography and a thin oceanic layer 2A are located between 0 km to 60 km and 130 km to 220 km. These amagmatic sections (Fig. 3.11) formed before 28 Ma and between 21 Ma to 11 Ma (Ehlers & Jokat 2009). Therefore, the oceanic crust of the Boreas Basin has been forming at the ultraslow spreading Knipovich Ridge since at least 28 Ma.

The results of the seismic refraction lines east of the Knipovich Ridge rift valley show also crustal variations which can be interpreted as magmatic and amagmatic segments (Ljones et al. 2004, Kandilarov et al. 2008, 2010). Along the seismic refraction line of Ritzmann et al. (2002), such variations were not observed. Following their conclusion, the seismic refraction line is located in an amagmatic segment.

Crustal and Upper Mantle Structures at other Ultraslow Spreading Ridges

Other investigated ultraslow ridge systems are (1) the Gakkel Ridge in the Arctic Ocean (Jokat et al. 2003, Jokat & Schmidt-Aursch 2007), (2) the Mohns Ridge south of the Knipovich Ridge (Klingelhöfer et al. 2000), and (3) the Southwest Indian Ridge in the Indian Ocean (Muller et al. 1999). A thin oceanic crust (1.9–6.0 km) is typical for these ridges (Muller et al. 1999, Klingelhöfer et al. 2000, Jokat et al. 2003, Jokat & Schmidt-Aursch 2007). Along the Gakkel Ridge, the oceanic crust is thinner (1.9–3.3 km, Jokat et al. 2003, Jokat & Schmidt-Aursch 2007) compared with the crust along the Knipovich Ridge (3.2 km). Furthermore, for the Gakkel Ridge no crustal velocities greater than 6.4 km/s were observed. Hence, along most parts of the Gakkel Ridge, oceanic layer 3 is absent. Based on the low mantle velocities ranging from 7.5 km/s to 7.8 km/s an upper mantle serpentinisation is possible (Jokat et al. 2003). At the Mohns Ridge and the Southwest Indian Ridge, the crustal thickness varies between 2.0 km and 6.0 km (Muller et al. 1999, Klingelhöfer et al. 2000). For both ultraslow spreading ridges, crustal layer 3 was modelled with velocities between 6.5 km/s and 7.0 km/s and subsequent thicknesses of 0.5 km to 3.5 km, respectively. Low mantle velocities (7.5–8.0 km/s) were also interpreted as serpentinisation of the upper mantle (Muller et al. 1999, Klingelhöfer et al. 2000).

3.3 Line Kong Oscar Fjord – Kolbeinsey Ridge (20090100)

The following results of line 20090100 as well as the interpretation of the crustal and upper mantle structures of Kong Oscar Fjord and the Kolbeinsey Ridge are submitted by Hermann & Jokat (2013b).

3.3.1 P-wave Model

The seismic refraction line 20090100 was acquired as an extension of the older seismic refraction line 94340 (Schlindwein & Jokat 1999). The combined P-wave model has a total length of 685 km and a depth of 30 km (Fig. 3.16). In addition to the classification of continental crust (Holbrook et al. 1992) and oceanic crust (Juteau & Maury 1999, Tab. 2.1), we used the definition of a continent-ocean transition zone (COT) after Whitmarsh & Miles (1995). Hence, our line can be divided into three crustal sections (Fig. 3.17): (1) continental crust between 0 km and 200 km, (2) transitional crust between 200 km and 340 km, and (3) oceanic crust between 340 km and 685 km.

Continental Crust (0–200 km)

The continental crust consists of four crustal layers with a total thickness of 28 km (Fig. 3.17). The upper two layers show P-wave velocities between 5.7 km/s and 6.3 km/s representing the upper continental crust (Figs. 3.16 and 3.17). The lower continental crust has P-wave velocities between 6.3 km/s and 6.9 km/s (Fig. 3.16). Following Schlindwein & Jokat (1999), the continental crust was influenced by the Caledonian orogeny.

Continent-Ocean Transition Zone (COT, 200–340 km)

The transitional crust (Fig. 3.17) is covered by 2 km to 2.5 km thick sediments with P-wave velocities of 4.4 km/s to 5.1 km/s (Fig. 3.16). Higher sediment velocities between 5.2 km/s and 5.7 km/s (240–280 km, Fig. 3.16) are only constrained by refracted rays of OBS 123 and land station 124, respectively (Fig. 3.18A).

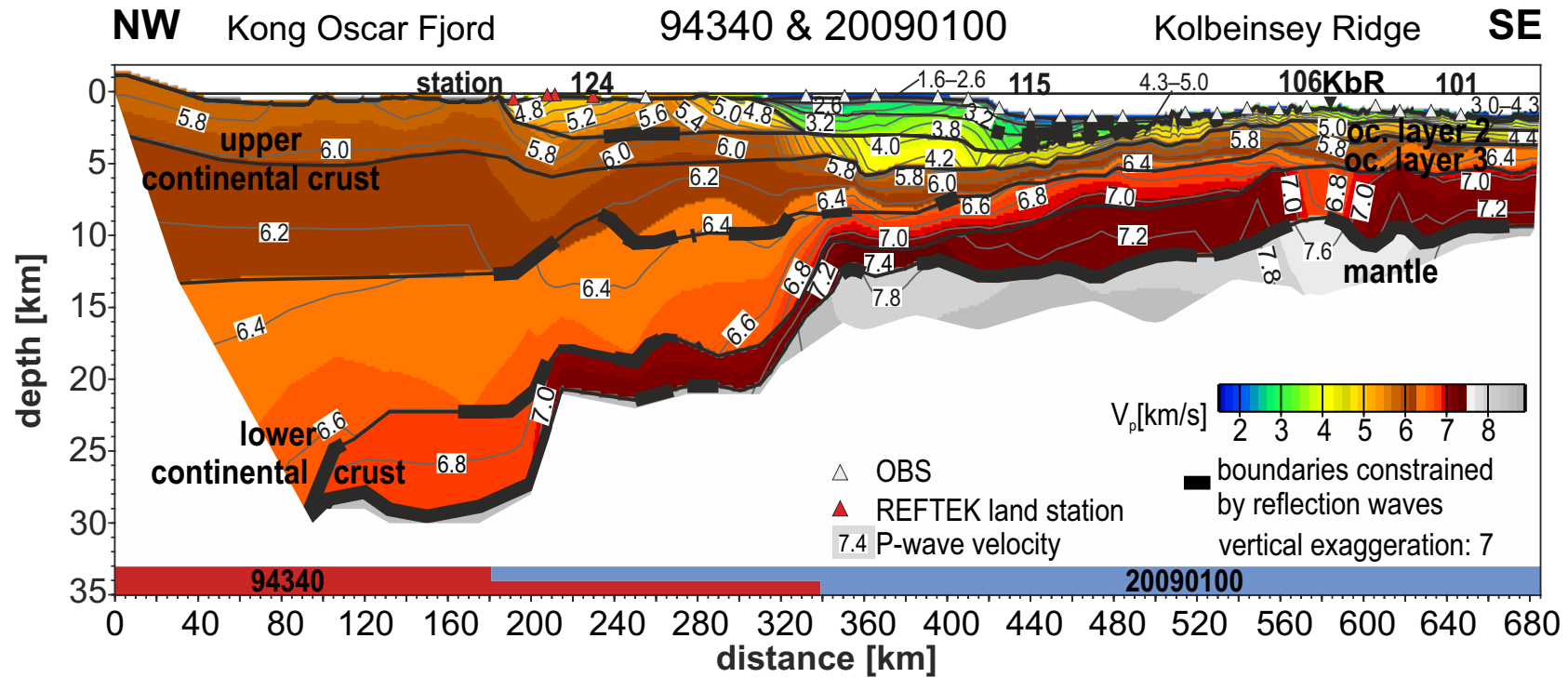


Figure 3.16: Combined P-wave model of line 94340 (Schlindwein & Jokat 1999) and line 20090100 (Hermann & Jokat 2013b).

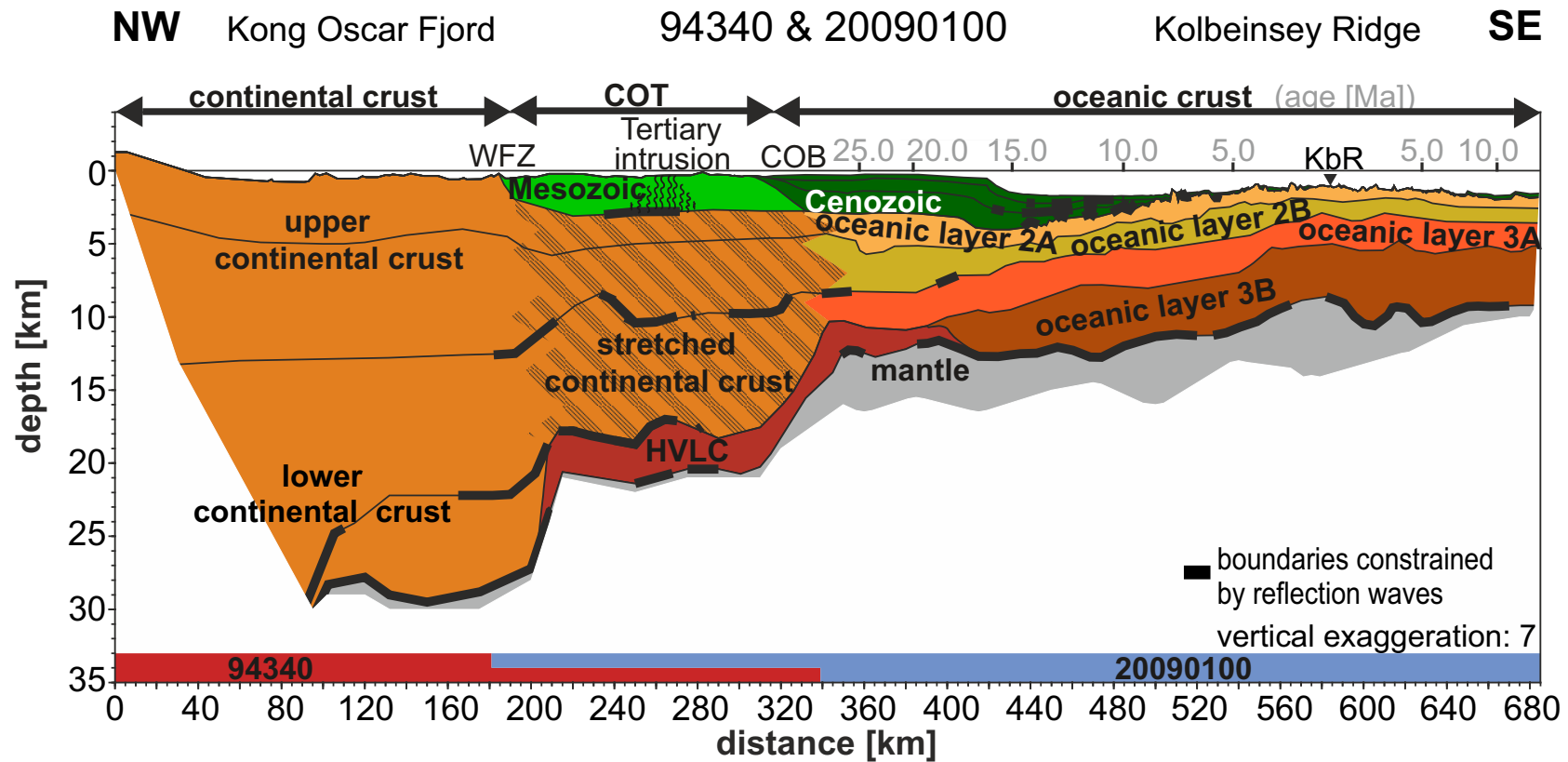


Figure 3.17: Interpretation of line 94340 (Schlindwein & Jokat 1999) and line 20090100 (Hermann & Jokat 2013b). Ages of the oceanic crust according to Müller et al. (2008).

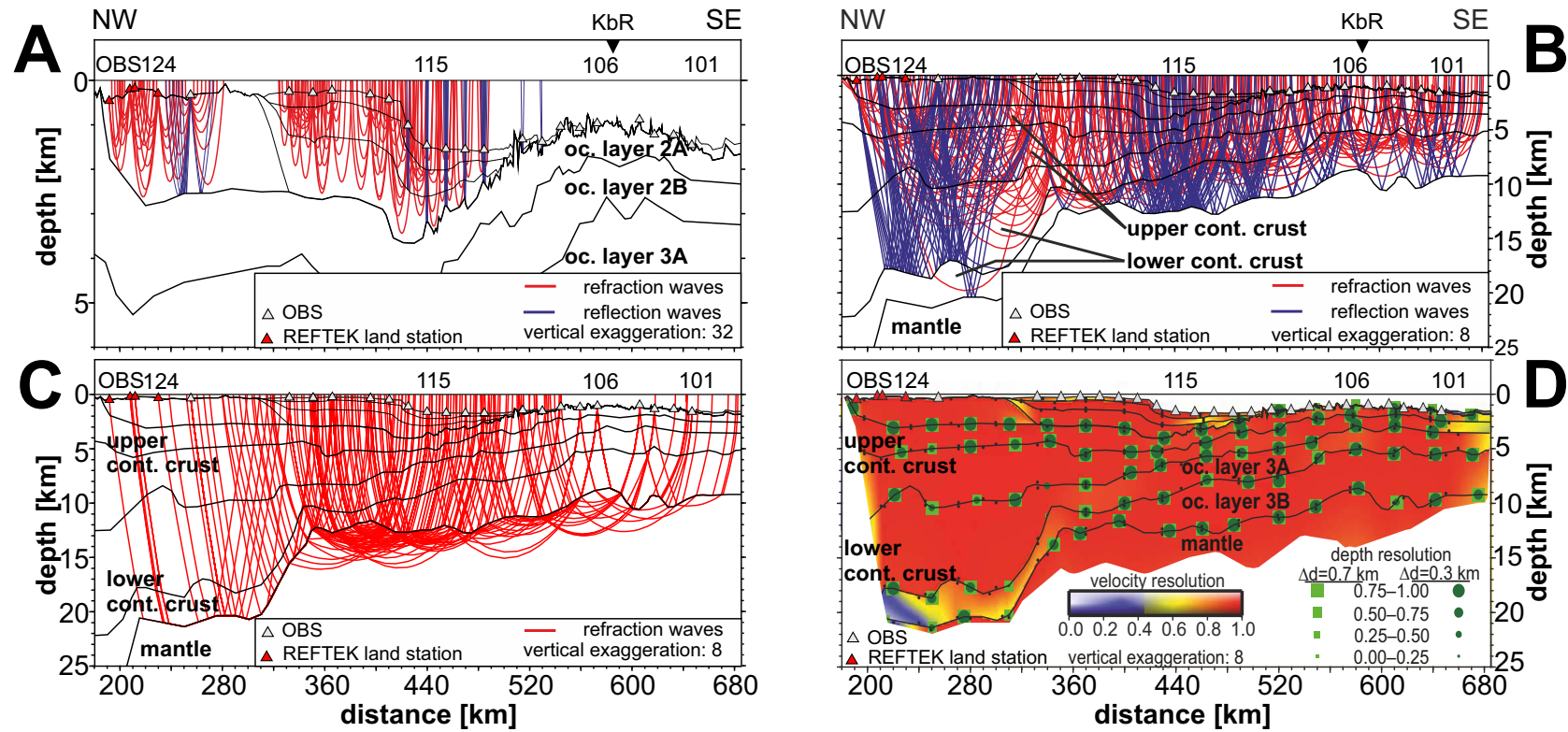


Figure 3.18: Ray coverage and resolution of seismic refraction line 20090100 (Hermann & Jokat 2013b). Ray coverage for (A) the sediments, (B) the crustal layers, and (C) the mantle. (D) resolution plot with node positions (black dots) for the calculation of the velocity resolution. Figure (A) is of different vertical exaggeration.

Compared with the 28 km thick continental crust, the thickness of the transitional crust is about 18 km (Fig. 3.17). The seismic velocities of the upper crustal layers within the transitional zone are similar to those of continental crust (5.7–6.7 km/s, Fig. 3.16). However, the deepest crustal layer has a thickness of about 3 km and high P-wave velocities larger than 7.0 km/s (Fig. 3.16).

Interpreting these results, we could identify, for the first time, the location of the COT between 200 km and 340 km, which means about 40 km offshore of Greenland. Following Schlindwein & Jokat (1999), the top layer consists of Mesozoic sediments which are deposited next to Caledonian rocks, separated by the Western Fault Zone (WFZ, 190 km, Fig. 3.17). The increased P-wave velocities within the Mesozoic sediments can be explained by intrusions of Lower Tertiary basalt sills and dykes (Fig. 3.17; Escher & Pulvertaft 1995, Schlindwein & Meyer 1999). Below the Mesozoic sediments, the stretched continental crust of the COT is characterised by a high-velocity lower crust (HVLC) with P-wave velocities above 7.0 km/s (Fig. 3.17; Schlindwein & Jokat 1999, Schmidt-Aursch & Jokat 2005a). Generally, these HVLC have been interpreted as underplated igneous crust (e. g. White & McKenzie 1989, Voss & Jokat 2007, Mjelde et al. 2008a). Several alternative hypotheses have also been proposed as: (1) igneous transitional or thick oceanic crust (e.g. Weigel et al. 1995, Holbrook et al. 2001), (2) granulite or eclogitic material (e. g. Mjelde et al. 2009), (3) pervasively intruded continental crust (e. g. White et al. 2008), or (4) serpentinised mantle (e. g. Whitmarsh et al. 1996, Funck et al. 2003, Lundin & Doré 2011). Therefore, HVLC is used as generalisation, because a distinction of the different scenarios is only possible due to deep drilling investigations and further detailed modelling (Peron-Pinvidic et al. 2012b).

Oceanic Crust (340–685 km)

The sediments, covering the oceanic crust, reach the maximum thickness (3 km) at the shelf edge, and almost vanish toward the Kolbeinsey Ridge rift valley (Fig. 3.17). The seismic sediment velocities range between 1.6 km/s and 3.8 km/s, which are well

3 Seismic Refraction Data

constrained by refracted and reflected waves (Figs. 3.16 and 3.18A). Slightly higher velocities of about +0.5 km/s are modelled between 360 km and 420 km (Fig. 3.16). Hence, the P-wave velocities are smaller than these within the Mesozoic sediments.

The average oceanic crustal thickness is 9 km (Fig. 3.17). The thickness is well constrained by refracted and reflected waves from the crust-mantle boundary along the entire oceanic crust (Figs. 3.16 and 3.18B). Between the transitional and the oceanic crust (340 km, Fig. 3.16), the P-wave velocities change rapidly. Towards the southeast, typical oceanic crustal P-wave velocities of 3.6 km/s to 4.3 km/s for oceanic layer 2A, 5.7 km/s to 6.3 km/s for oceanic layer 2B, 6.6 km/s to 7.0 km/s for oceanic layer 3A, and 7.1 km/s to 7.3 km/s for oceanic layer 3B are observed (Tab. 2.1, Figs. 3.16 and 3.17). Below the Kolbeinsey Ridge rift valley the seismic velocities decrease between 17% for oceanic layer 2A and 3% for oceanic layer 3B (Fig. 3.16).

Following the interpretation of Weigel et al. (1995) and Voss et al. (2009), the upper layers consist of Cenozoic sediments. The abrupt change of crustal velocities at 340 km marks the continent-ocean boundary (COB), with oceanic crust to the southeast (Fig. 3.17). Below the Kolbeinsey Ridge rift valley the crustal P-wave velocities decrease and represent most likely higher porosities and higher temperatures compared with its surroundings (Grevemeyer & Weigel 1996, Kodaira et al. 1997).

Upper Mantle

The upper mantle velocity is 7.9 km/s (Fig. 3.16). Below the Kolbeinsey Ridge rift valley the mantle velocities decrease to 7.6 km/s (Fig. 3.16). The low velocity can be assigned to about 10% mantle serpentinisation (Horen et al. 1996, Christensen 2004) and higher temperatures compared with its surroundings (Christensen 1979, Kodaira et al. 1997).

3.3.2 Error Analysis

The significance of the P-wave model is described by the χ^2 value of 1.388 and the t_{RMS} value of 0.126 s (Tab. 3.5). Approximately 97% of the 18643 P-wave picks could

be ray traced. Following the method of Schlindwein & Jokat (1999), the uncertainties of the P-wave velocities are ± 0.3 km/s for the high-velocity lower crust and ± 0.2 km/s for the rest of the P-wave model. The higher uncertainty for the HVLC is based on the low ray coverage compared with the rest of the P-wave model (Figs. 3.18A–C). The depth uncertainties of the boundaries vary by ± 0.3 km for the sediment layers and ± 0.7 km for the crust-mantle boundary. Below the Kolbeinsey Ridge and the HVLC, the depth uncertainty is ± 1 km due to high lateral variations in crustal structures and varying ray coverage (Figs. 3.18B–C).

The resolution of the P-wave velocities is well resolved (0.50–1.00) for an uncertainty of ± 0.2 km/s within the whole model (Fig. 3.18D). However, three locations of poor velocity resolution (0.40–0.46) exist (Fig. 3.18D): (1) the HVLC between 210 and 340 km, (2) the Mesozoic-Cenozoic sediment boundary at 320 km, and (3) the area of non-reversed ray coverage to the southeast of 650 km. The depth values of the upper layers are well resolved (>0.50) within our model for an uncertainty of ± 0.3 km and of the crust-mantle boundary for ± 0.7 km (Fig. 3.18D).

Table 3.5: Statistical significance (χ^2) of the P-wave model based on the numbers of observed travel time picks (n) and the estimated uncertainties (t_{est}) for the different layers. The residual time (t_{RMS}) represents the misfit between the observed and the calculated travel times.

Layer	n	t_{est} [ms]	t_{RMS} [s]	χ^2
Sediment	1961	50 – 175	0.083	1.831
Upper Cont. Crust/Oc. Layer 2	4539	75 – 185	0.108	1.054
Lower Cont. Crust/Oc. Layer 3	9442	110 – 220	0.131	1.285
Mantle	2701	100 – 220	0.164	1.991
All	18643	50 – 220	0.126	1.388

3 Seismic Refraction Data

3.3.3 Discussion of Line 20090100

Crustal and Upper Mantle Structures in Kong Oscar Fjord and across Kolbeinsey Ridge

The seismic refraction line crosses two geological provinces: Kong Oscar Fjord and Kolbeinsey Ridge (Fig. 3.1C). This line represents the only well resolved available crustal information about the HVLC below Kong Oscar Fjord.

The P-wave model show that thick sediments cover the basement of the outer Kong Oscar Fjord (180–340 km, Fig. 3.17). Due to observed P-wave velocities of 4.4 km/s to 5.1 km/s (Fig. 3.16), and onshore geological as well as geophysical investigations, the sediments are most likely of Mesozoic age (Escher & Pulvertaft 1995, Schlindwein & Jokat 1999, Schlindwein & Meyer 1999). Furthermore, the observed shallow intrusions within the Mesozoic sediments are postulated from magnetic modelling results as well (Schlindwein & Jokat 1999).

The P-wave velocities of the continental crust are comparable with other results within the research area (Weigel et al. 1995, Schlindwein & Jokat 1999). The existence of the HVLC below the Mesozoic sediments support earlier results from Kong Oscar Fjord (Weigel et al. 1995, Schlindwein & Jokat 1999, Schlindwein & Meyer 1999). In contrast, the conjugate margin of East Greenland – the western margin of the Jan Mayen Micro-continent – shows no HVLC (Fig. 3.19; Kodaira et al. 1998a,b). In addition, the continental crust is 5 km thick and, therefore, 13 km less compared with the COT of the Kong Oscar Fjord area. These differences can be related to the geological evolution of the research area (Mjelde et al. 2008a; next paragraph).

The oceanic crust consists of four modelled sublayers (2A, 2B, 3A, 3B) along the seismic refraction line. The oceanic crustal thickness of 9 km and the low crustal P-wave velocities below the Kolbeinsey Ridge fit well with results of Kodaira et al. (1997, 1998b, 560–680 km, Fig. 3.19), although they did not divide the lower crust into oceanic layers 3A and 3B. In contrast, Weigel et al. (1995) modelled an oceanic crustal thickness of 13 km. Our identified location of the continent-ocean boundary is

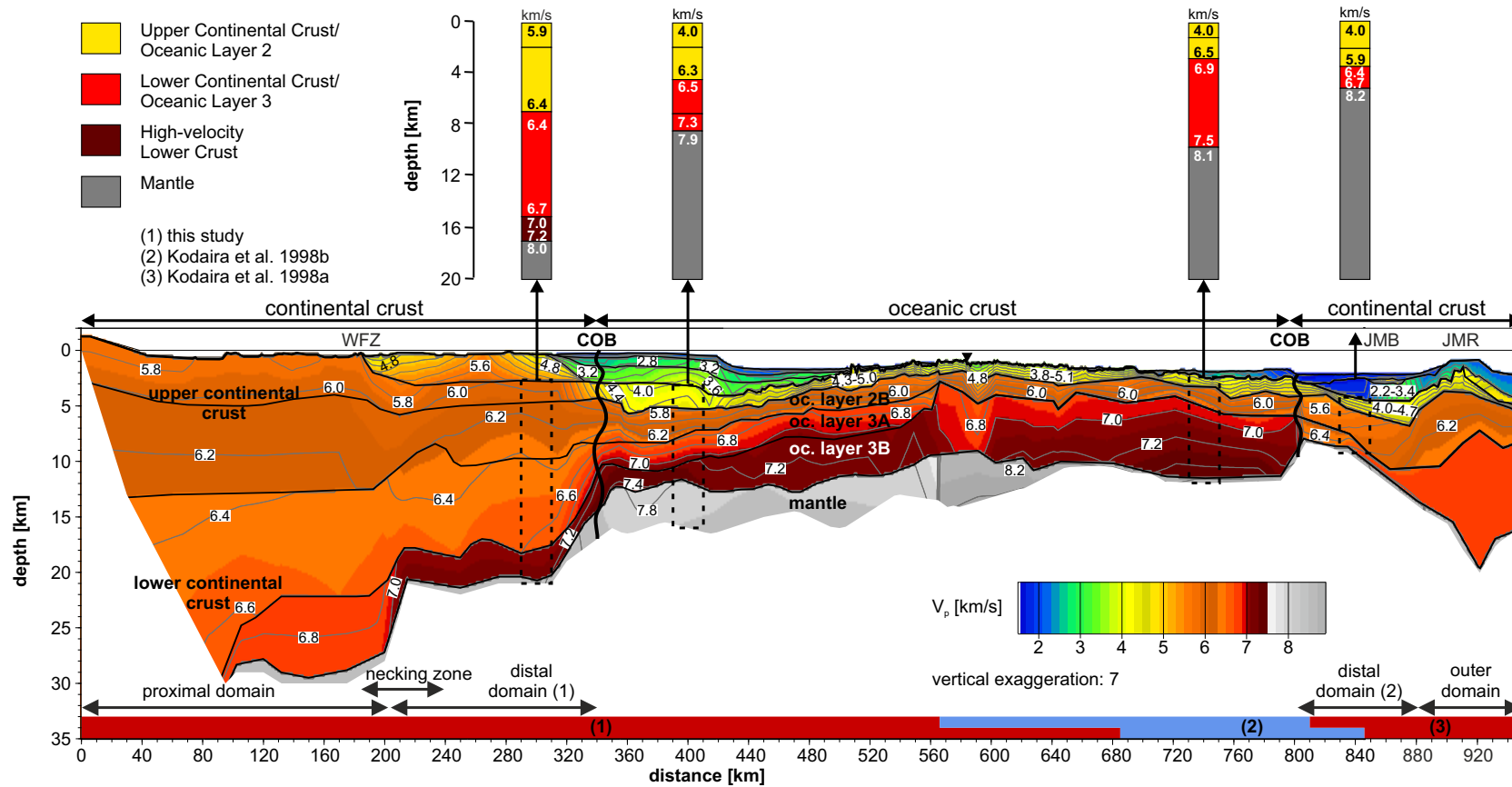


Figure 3.19: Combined crustal P-wave models running from the East Greenland margin to the Jan Mayen Micro-continent across the Kolbeinsey Ridge (Hermann & Jokat 2013b). The variations in crustal thickness and crustal P-wave velocities at both continent-ocean boundaries (COB) are shown in 1D-columns. For locations of the seismic refraction lines see Figure 2.2 (Chapter 2.1).

3 Seismic Refraction Data

in good agreement with the results of Weigel et al. (1995), despite a much larger receiver spacing (50 km), and a high noise level of their data based on heavy ice conditions.

Evolution of the high-velocity lower crust (HVLC)

The P-wave model indicate the presence of a HVLC in the COT with P-wave velocities higher than 7.0 km/s and a thickness of 3 km (Figs. 3.16 and 3.17; Holbrook et al. 1992). In general, the HVLC is associated with a volcanic margin, characterised by excess magmatism during continental breakup (Geoffroy 2005).

In total, HVLC was found at three locations in the Norwegian-Greenland Sea: (1) north of Kong Oscar Fjord along the East Greenland margin (Voss et al. 2009), (2) at the eastern margin of the Jan Mayen Micro-continent (Breivik et al. 2012), and (3) along the Mid-Norway margin (Figs. 3.19 and 3.20; Mjelde et al. 2001). At the East Greenland and Mid-Norway margin, the thickness of the HVLC decreases distal to the Jan Mayen Fracture Zone (Fig. 3.20; Mjelde et al. 2001, Voss et al. 2009). The East Greenland margin south of Kong Oscar Fjord and the western margin of the Jan Mayen Micro-continent show no HVLC (Figs. 3.19 and 3.20A, 800–900 km; Weigel et al. 1995, Kodaira et al. 1998a,b, Schlindwein & Jokat 1999, Schmidt-Aursch & Jokat 2005a).

The evolution of the HVLC can be related to episodically large melt production and magmatism along the Jan Mayen Fracture Zone since Mid Eocene time (~ 48 Ma, magnetic anomaly C21; Gernigon et al. 2009, Gradstein et al. 2012, Kandilarov et al. 2012), in particular, due to the separation of the Jan Mayen Micro-continent off East Greenland. Thereby, the Jan Mayen Fracture Zone (a leaky oceanic transform) acted as a lithospheric thin-spot (a long-lived magmatic pathway for melts) during the oceanic spreading rather than a lithospheric barrier (Gernigon et al. 2009). This suggestion is supported by numerical simulations of Huang et al. (2003), who shows that small-scale convection can develop beneath the transform itself. A rheology of brittle weakening of the lithosphere along the fracture zone can also explain regions of enhanced mantle upwelling as well as elevated temperatures beneath transform faults (Behn et al. 2007).

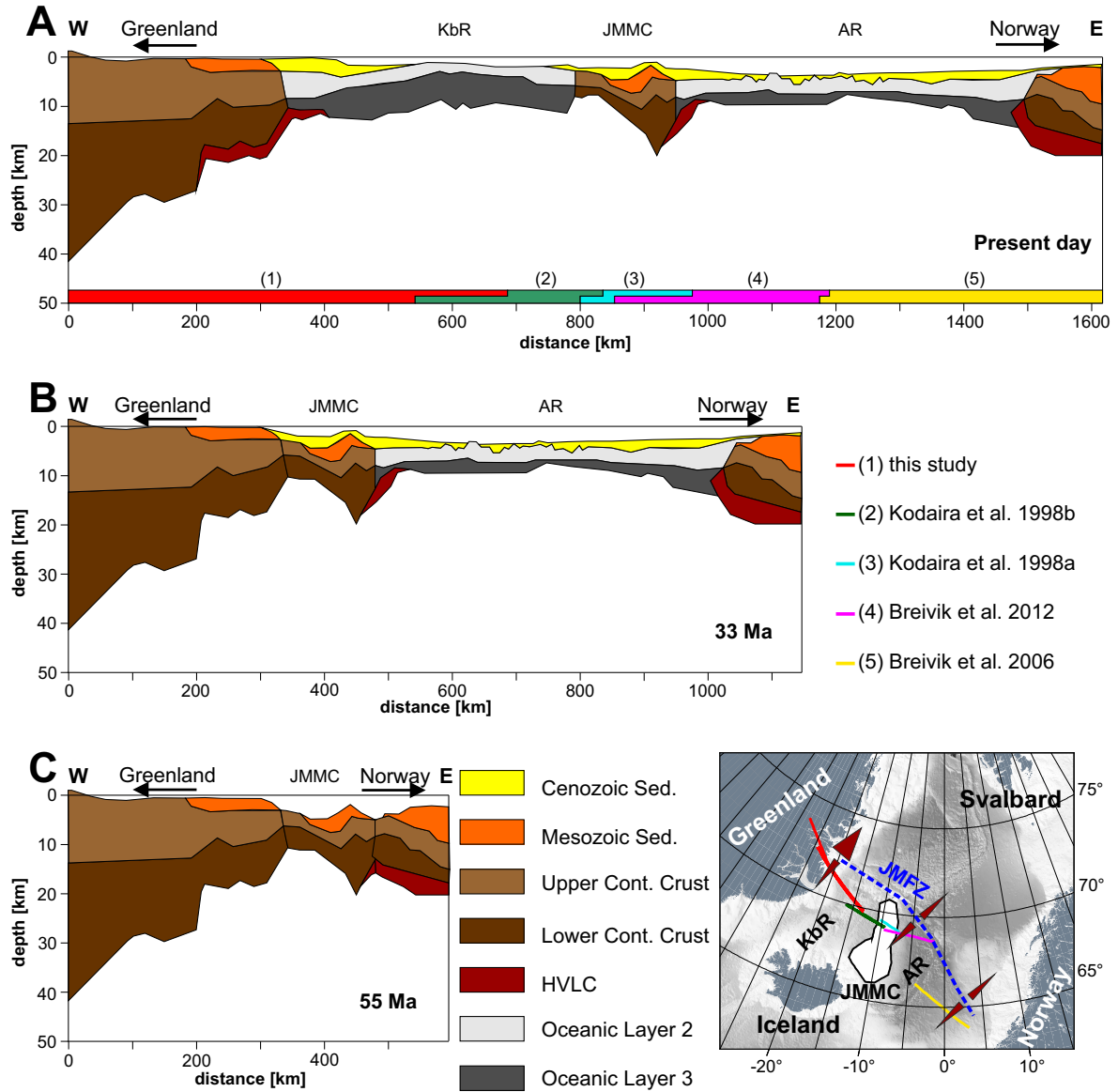


Figure 3.20: Crustal transect across the northern North Atlantic (Hermann & Jokat 2013b, modified after Mjelde et al. 2008a) for (A) present day, (B) ~33 Ma, and (C) ~55 Ma ago. The map shows the seismic refraction lines used for the crustal transect and triangles representing schematically decreasing HVLC thickness away from the Jan Mayen Fracture Zone. In contrast to Mjelde et al. (2008a), the HVLC below Kong Oscar Fjord evolved due to continental breakup of the Jan Mayen Micro-continent off East Greenland.

3 Seismic Refraction Data

According to Gernigon et al. (2009), a combination of these mechanisms could explain enhanced mantle upwelling along the Jan Mayen Fracture Zone. As a consequence, enhanced mantle decompression and partial melting along the Jan Mayen Fracture Zone occurred, compared with surrounding oceanic domains. Based on this, the HVLC below Kong Oscar Fjord evolved and likely increased the thickness of the existing HVLC north of the Jan Mayen Fracture Zone (Fig. 3.20; Voss et al. 2009).

The proposed evolution of the HVLC below Kong Oscar Fjord is first of all indicated by the extension of the HVLC below the COT and below the oceanic crust (Figs. 3.17 and 3.20A; Gaina et al. 2009). This observation implies the evolution of the HVLC during and after the breakup of the Jan Mayen Micro-continent off East Greenland (Fig. 3.20). The excess magmatism along the Jan Mayen Fracture Zone might further explain the evolution of Jan Mayen island as an oceanic plateau north of the Jan Mayen Micro-continent (Fig. 3.1; Kandilarov et al. 2012). Below the oceanic plateau a HVLC exists, too (Kandilarov et al. 2012), which might be the counterpart to the HVLC below Kong Oscar Fjord. The decreasing thickness of the HVLC (15 km) northwards of the Jan Mayen Fracture Zone (Voss et al. 2009) as well as the disappearance of the HVLC to the south of Kong Oscar Fjord (Fig. 3.20; Schmidt-Aursch & Jokat 2005a) support the interpretation of enhanced partial melting along the Jan Mayen Fracture Zone. The HVLC north of the Jan Mayen Fracture Zone evolved due to two magmatic events: (1) excess magmatism during the continental breakup between Europe and Greenland, and (2) a second magmatic event during the breakup of the Jan Mayen Micro-continent off East Greenland (Voss et al. 2009). The second magmatic event increased the thickness of the HVLC north of the Jan Mayen Fracture Zone, in contrast to the thinner HVLC below the conjugate margin off Norway (Fig. 3.20; Voss et al. 2009). Age dating of volcanic rocks along the Jan Mayen Fracture Zone indicate young volcanism to the west and to the north of Jan Mayen island (<1 Ma, Mertz et al. 2004), which supports our model of enhanced melting along the fracture zone.

We postulate that the HVLC below Kong Oscar Fjord was formed during the separation of the Jan Mayen Micro-continent off East Greenland (Fig. 3.20), and not during the

initial breakup between Greenland and Norway in the Early Eocene as proposed by Mjelde et al. (2008a). Facts supporting our interpretations are: (1) below the Scoresby Sund no HVLC is observed (Schmidt-Aursch & Jokat 2005a), and (2) below the western margin of the Jan Mayen Micro-continent no HVLC could be modelled (Figs. 3.19 and 3.20; Kodaira et al. 1998a,b).

Crustal structures of Kolbeinsey Ridge and conjugate margins

Passive continental margins, typically observed around the Atlantic Ocean, show similar crustal structures (Tab. 3.6; Peron-Pinvidic et al. 2012b, 2013). Using these structures for the description of Atlantic rifted margins, the Caledonides (0–200 km, Fig. 3.19) corresponds to the proximal, and the Western Fault Zone (200 km, Fig. 3.19) to the necking domain. These domains are characterised by about 30 km thick continental crust and by a drastic crustal thinning, respectively (Tab. 3.6). However, Peron-Pinvidic et al. (2012b) could not describe a well defined distal and outer domain for the Kong Oscar Fjord margin and the Jan Mayen Micro-continent margin for the present day tectonic situation using the data of Weigel et al. (1995) (Fig. 3.20A). Instead, they described the Kong Oscar Fjord and the Jan Mayen Micro-continent margins separately. Narrow distal and outer domains along the margins of Kong Oscar Fjord and the Jan Mayen Micro-continent are interpreted.

Following our interpretation, we assume the tectonic situation before the Jan Mayen Micro-continent break up off East Greenland (Fig. 3.20B). The Jan Mayen Basin (hyper-extended crust) corresponds to the distal domain of the former continental margin, and the Jan Mayen Ridge is related to the outer domain (Fig. 3.19). These two domains are mainly characterised by transitional and hyper-extended crust (distal domain) as well as by an outer high and significant top basement topography (outer domain) (Tab. 3.6). Comparing our classification of the former East Greenland margin with the conjugate southern Vøring margin (VM), significant similarities are found (Tab. 3.6, Fig. 3.21). The proximal and necking domain of the Vøring margin are related to the Trøndelag platform (TP) and the Bremstein-Vingleia Fault Complex (BVFC), respectively

3 Seismic Refraction Data

(Tab. 3.6, Fig. 3.21; Peron-Pinvidic et al. 2012b, 2013). The 30 km thick continental crust of the Trøndelag platform significantly thins at the Bremstein-Vingleia Fault Complex and reaches its minimum thickness of 8 km within the Vøring Basin (VB, Fig. 3.21). The hyper-extended continental crust of the Vøring Basin corresponds to the distal domain (Tab. 3.6, Fig. 3.21). The outer domain is associated with the Vøring Marginal High (VMH), which is an outer high of the Vøring margin (Tab. 3.6, Fig. 3.21; Peron-Pinvidic et al. 2012b, 2013). The classification of both conjugate margins support the interpretation of the Jan Mayen Ridge as an outer high of the former East Greenland margin during the initial separation in the Early Eocene.

Table 3.6: Domains of Atlantic rifted margins and their main characteristics (Peron-Pinvidic et al. 2012b, 2013) compared with corresponding structures of Kong Oscar Fjord–Jan Mayen margin (Fig. 3.19) and Vøring margin (Fig. 3.21).

Domain	Characteristic	Kong Oscar Fjord- Jan Mayen Margin	Vøring Margin
Proximal	~30 km thick continental crust	Caledonides	Trøndelag Platform
Necking	major thinning of conti- nental crust, Moho uplift	Western Fault Zone	Bremstein-Vingleia Fault Complex
Distal	hyper-extended or transitional crust (COT)	COT Kong Oscar Fjord, Jan Mayen Basin	Vøring Basin
Outer	significant outer basement high	Jan Mayen Ridge	Vøring Marginal High
Oceanic	oceanic crust	Kolbeinsey Basin	Norway Basin

Hence, our interpretation has significant consequences for the crustal accretion: the Kolbeinsey Ridge developed in the area of hyper-extended continental crust (distal domain) of the former East Greenland margin, and initiated the formation of the Jan Mayen Micro-continent due to changes in "far field forces" (named after Peron-Pinvidic

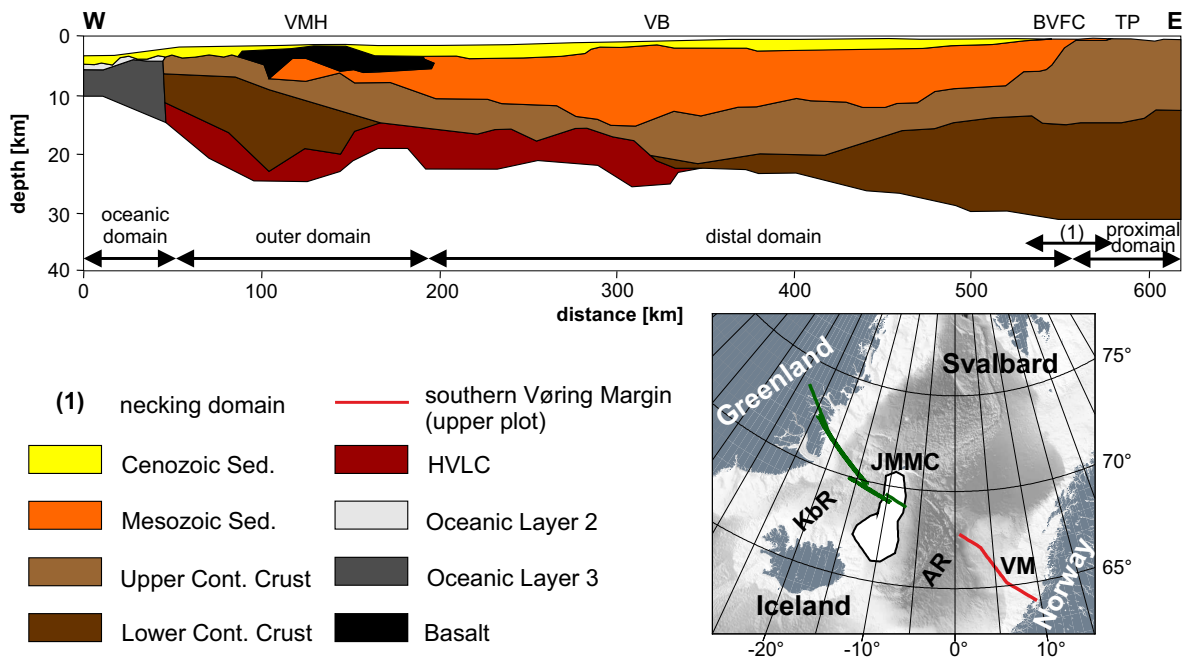


Figure 3.21: Schematic crustal structure of the southern Vøring margin (conjugate margin (red line in small map) to the East Greenland-Jan Mayen margin (green line in small map); Mjelde et al. 2009). The map shows the location of the crustal transects of the Kong Oscar Fjord-Jan Mayen margin (Fig. 3.19) and the conjugate southern Vøring margin.

et al. 2012b). The result is a thicker oceanic crust, compared with normal oceanic crust (Juteau & Maury 1999). Especially oceanic layer 3 is approximately two kilometres thicker than a normal oceanic layer 3 (Fig. 3.22).

In general, thick oceanic crust is associated with higher mantle temperatures, for example +40°C below the Kolbeinsey Basin (Kodaira et al. 1998b, Hooft et al. 2006). In contrast, Armitage et al. (2009, 2010) showed that a thick oceanic crust additionally depends on the rift history of the lithosphere. The rift history includes considerable extension of the lithosphere prior to the impact of a thermal anomaly within the mantle. The combination of thinned lithosphere and higher temperature results in an enhanced melt production at the oceanic ridge. This model explains the thick oceanic crust at the Kolbeinsey Ridge. In addition, the model also explains the thin oceanic crust north of the Jan Mayen Fracture Zone due to the different rift history.

3 Seismic Refraction Data

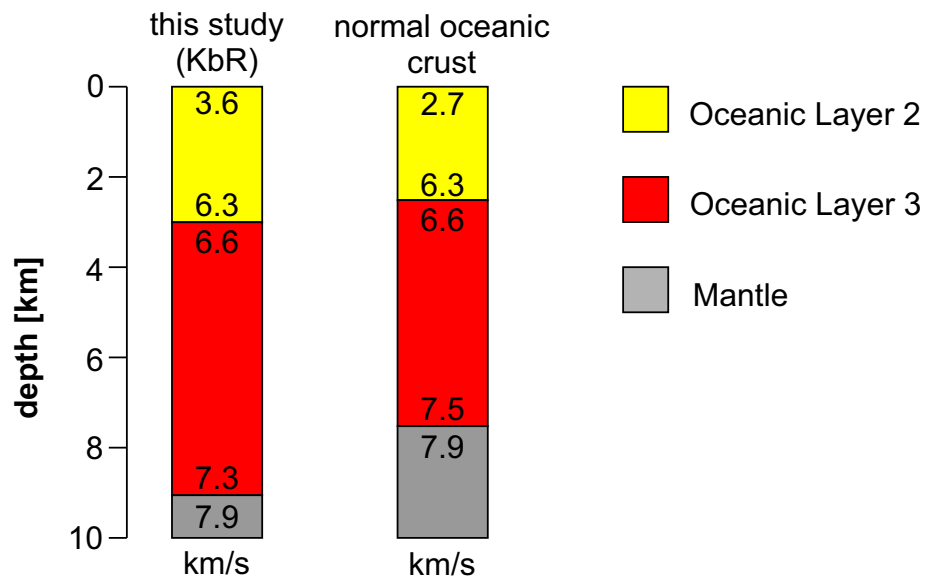


Figure 3.22: Comparison of oceanic crustal thickness at Kolbeinsey Ridge with normal oceanic crust (Juteau & Maury 1999).

4 Gravity Data

4.1 Gravimetric 2.5D Modelling

The results of the seismic refraction models (Chapter 3) were further verified by 2.5D gravity modelling. The 2.5D gravity modelling provides additional information about sedimentary, crustal and upper mantle densities within the research area. Finally, for the compilation of a 3D gravity model, our seismic and 2.5D gravity results are used as boundary conditions (Chapter 4.2.2).

4.1.1 Data Acquisition, Processing and Modelling

Parallel to both seismic refraction lines (Chapter 3), gravity data were continuously recorded with a sample rate of 10 s using a KSS31 gravimeter developed by Bodensee-werke (Jokat et al. 2010). Based on an average ship velocity of 2.5 m/s, the resulting sampling distance was approximately 25 m. For the integration of the relative sea measurements into the International Gravity Standardisation Network (IGSN) as well as for the instrumental drift correction, tie measurements with a LaCoste & Romberg gravimeter (model no. G-1031) were done. The drift of the KSS31 gravimeter is nearly linear with a drift rate less than $30 \mu\text{m}/\text{s}^2$ per month and the accuracy of the marine gravity data is approximately $25 \mu\text{m}/\text{s}^2$ (BGGs 2011).

Processing of the gravity data included: determination of instrumental drift ($\sim 23 \mu\text{m}/\text{s}^2$ per month), latitude correction ($< 1470 \mu\text{m}/\text{s}^2$), Eötvös correction ($< 219 \mu\text{m}/\text{s}^2$), and free-air correction (Torge 1989, Blakely 1995). Finally, the free-air anomaly values were low-pass filtered with a cut-off wavelength of 80 s in order to suppress the ship noise (Voss & Jokat 2007).

2.5D gravity modelling was done using the software package *IGMAS* (Götze & Lahmeyer 1988). Therefore, our two P-wave models were converted into a preliminary density model by applying the empirical velocity-density relation of Ludwig et al. (1970)

$$\rho = -0.00283V_P^4 + 0.0704V_P^3 - 0.598V_P^2 + 2.23V_P - 0.7 \quad (4.1)$$

4 Gravity Data

with ρ the density in g/cm^3 and V_P the P-wave velocity in km/s (Fig. 4.1). Using the P-wave models as boundary conditions, the ambiguity associated with potential methods was significantly limited (Blakely 1995). For the 2.5D gravity modelling, the P-wave model layers were split into several polygons with constant densities and were extended by five times the line length perpendicular to the line orientation (Figs. 4.2 and 4.3). During the modelling, the layer boundaries were kept constant by only slightly changing the density values. A reasonable fit between modelled and observed gravity data was reached by minor variations of the sedimentary and crustal densities and significant modifications of the mantle densities. The modelled density values are within the error bars of the applied velocity-density relation of Ludwig et al. (1970) (Fig. 4.1).

The density uncertainties were estimated by model perturbations (density variations) of single polygons until the residuals are greater than the uncertainty of the marine gravity data. The uncertainties were estimated with $\pm 10 \text{ kg/m}^3$. However, the ambiguity of potential methods (Blakely 1995) is not included in the uncertainty investigations. Therefore, the modelled densities represent rather relative density values than absolute density values.

4.1.2 Line Boreas Basin – Knipovich Ridge (20090200)

The following results of the 2.5D gravity modelling of line 20090200 and its interpretation are published by Hermann & Jokat (2013a).

Gravity Model

The free-air anomaly along line 20090200 ranges between $-150 \mu\text{m/s}^2$ and $800 \mu\text{m/s}^2$ (Fig. 4.2). At the Knipovich Ridge rift valley a significant, symmetric gravity low with an amplitude of approximately $800 \mu\text{m/s}^2$ can be observed (Fig. 4.2). This negative gravity anomaly is typical for mid-ocean spreading centres (Chapter 4.2.1, Fig. 4.4).

The sedimentary densities increase with depth from 1720 kg/m^3 to 2230 kg/m^3 . The densities of the oceanic crust vary between 2300 kg/m^3 and 2400 kg/m^3 for layer 2A,

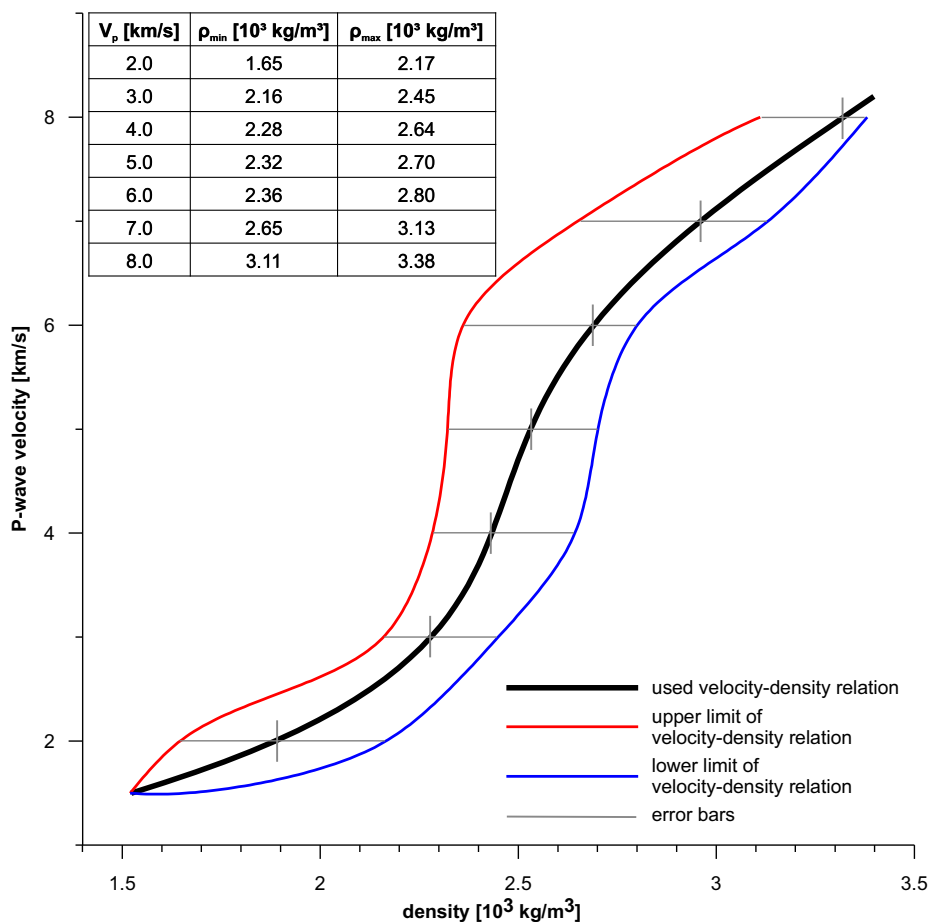


Figure 4.1: Empirical velocity-density relation of Ludwig et al. (1970) with its error bars (small table).

2500 kg/m 3 and 2600 kg/m 3 for layer 2B, and 2700 kg/m 3 and 2900 kg/m 3 for layer 2C. Below the Knipovich Ridge rift valley, the crustal densities are decreased and vary between 2300 kg/m 3 and 2700 kg/m 3 (Fig. 4.2). In accordance with our seismic results, no oceanic layer 3 has to be modelled, to achieve a reasonable fit between the observed and calculated gravity data. The mantle densities vary between 3300 kg/m 3 , close to the Northeast Greenland Shelf, and 3170 kg/m 3 , below the Knipovich Ridge rift valley (Fig. 4.2).

Error Analysis

In general, the gravity model is consistent with our seismic refraction model. The standard deviation is 60 $\mu\text{m/s}^2$ relative to the observed free-air anomaly, which is within

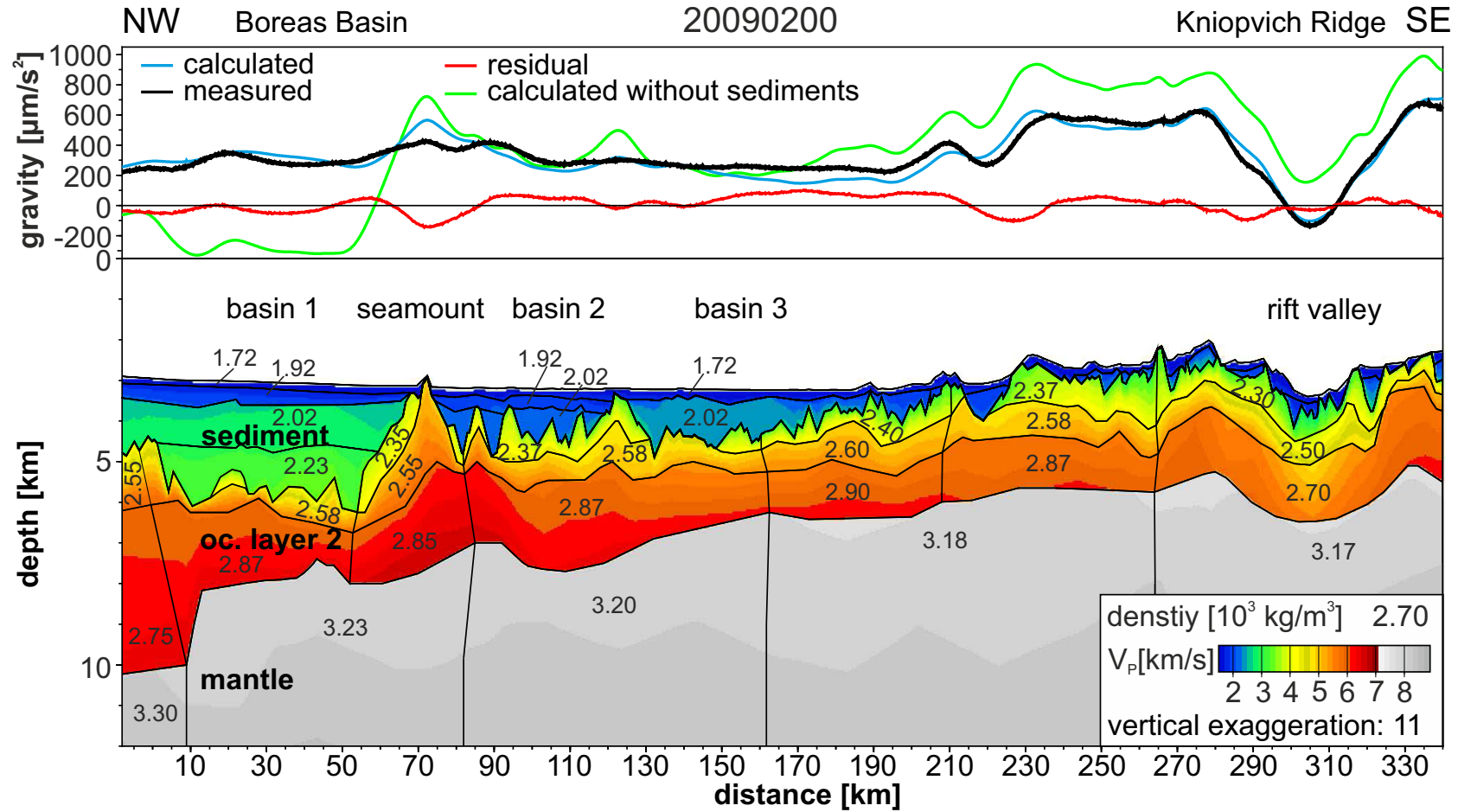


Figure 4.2: 2.5D gravity model based on the gravity data acquired parallel to line 20090200. The upper panel shows the observed and calculated free-air anomaly, the free-air anomaly without sediments, and the residuals (Hermann & Jokat 2013a).

the uncertainty of the used modelling method ($\pm 100 \mu\text{m/s}^2$, Ljones et al. 2004). The maximum residual between the modelled and the measured gravity values is $-160 \mu\text{m/s}^2$. This value is caused by the 3D effect of the seamount at 70 km line distance (Fig. 4.2), since the true 3D shape of the seamount is not known.

Comparison of gravity and seismic model

The sediments along line 20090200 show increasing density values and decreasing V_P/V_S ratios with depth (Chapter 3.2, Fig. 3.10), indicating a growing consolidation of the sediments with depth. Based on our seismic model (Chapter 3.2, Fig. 3.10), the Mid Miocene reflector was interpreted inbetween the sediments, where the P-wave velocities significant changed from 2.2 km/s to 2.7 km/s. However, such a boundary could not be identified in the gravity model, because of a constant increase of the density values with depth (Fig. 4.2).

The crustal densities are in good accordance with oceanic layer 2 densities of the Atlantic ocean (2490–2870 kg/m³, Carlson & Raskin 1984). Small lateral density variations up to 500 kg/m³ (Fig. 4.2) indicate no significant variations in the composition of oceanic crust as well as thermal density variations. At the Knipovich Ridge rift valley significant reduced crustal densities (2300–2700 kg/m³, Fig. 4.2) reveal open fissures and cracks in the basaltic layers (Grevemeyer & Weigel 1996). Northwest of 360 km, no reduced crustal densities are found (Fig. 4.2), since fissures and cracks are closing with age. Close to the Northeast Greenland Shelf, reduced crustal densities (2550–2750 kg/m³, Fig. 4.2) are modelled. However, this region is not well constrained by seismic refraction waves (Chapter 3, Fig. 3.1B), because heavy sea ice conditions prevented the prolongation of the seismic refraction line onto the shelf, and therefore, across the suggested continent-ocean transition zone (Engen et al. 2008). Consequently, it remains speculative, if the reduced crustal densities indicate the oceanward limit of the continent-ocean transition zone of the Northeast Greenland margin.

Lateral density variations of the upper mantle range between 3170 kg/m³ and 3300 kg/m³ along our entire line (Fig. 4.2). The lateral variations are not observed in the P-wave

4 Gravity Data

model (Chapter 3.2, Fig. 3.10). Therefore, the increasing mantle densities from the Knipovich Ridge towards the East Greenland margin can be explained by decreasing mantle temperatures and thickening of the lithosphere (Breivik et al. 1999, Engen et al. 2006).

Existence of an extinct spreading centre in the Boreas Basin

Mosar et al. (2002b) suggested an extinct spreading centre in the Boreas Basin. It is located in the area between 0 km and 80 km (Fig. 4.2). Following Mosar et al. (2002b), an early spreading segment was linked to the Mohns Ridge segment via the Greenland Fracture Zone. Unfortunately, the aeromagnetic data of Ehlers & Jokat (2009) does not cover the area northwest of the seamount (70 km, Fig. 4.2). Therefore, no magnetic spreading anomalies could be identified in this area. An extinct spreading centre would produce a symmetric gravity low between 20 km and 50 km (Fig. 4.2), flanked by two gravity highs at 0 km and 70 km after removing the gravity effect of sediments (Fig. 4.2). However, no symmetric gravity low is evident (blue line, Fig. 4.2). Thus, we conclude that no extinct spreading centre exists. Hence, the Boreas Basin was formed along the ultraslow spreading Knipovich Ridge during its entire history.

4.1.3 Line Kong Oscar Fjord – Kolbeinsey Ridge (20090100)

The following results of the 2.5D gravity modelling of line 20090100 and its interpretation are submitted by Hermann & Jokat (2013a).

Gravity Model

The free-air anomaly values range between $-1030 \mu\text{m/s}^2$ and $710 \mu\text{m/s}^2$ along the entire line (Fig. 4.3). In general, the anomaly values are typical for passive continental margins (Fig. 4.3; Worzel 1968, Rabinowitz 1982, Watts & Fairhead 1999): (1) free-air gravity highs over the shelf break (at 400 km), (2) free-air gravity lows over the continental slope (at 440 km), and (3) a free-air gravity high farther seaward (>520 km). At the Kolbeinsey Ridge rift valley a symmetric gravity low with an amplitude of approxi-

mately $200 \mu\text{m}/\text{s}^2$ can be observed (580 km, Fig. 4.3). The densities of the continental crust increase with depth from $2750 \text{ kg}/\text{m}^3$ to $3150 \text{ kg}/\text{m}^3$ (<200 km, Fig. 4.3).

In the continent-ocean transition zone, the Mesozoic sediment cover has a density of $2540 \text{ kg}/\text{m}^3$ (190–310 km, Fig. 4.3). Higher densities of $2620 \text{ kg}/\text{m}^3$ within the Mesozoic sediments are based on intrusions of Lower Tertiary basalt sills and dykes (Escher & Pulvertaft 1995, Schlindwein & Meyer 1999). The upper layer densities of the transitional crust vary between $2680 \text{ kg}/\text{m}^3$ and $2910 \text{ kg}/\text{m}^3$ (200–340 km, Fig. 4.3). The deepest crustal layer has a density of $3180 \text{ kg}/\text{m}^3$, indicating the HVLC (200–390 km, Fig. 4.3).

In the oceanic domain, the Cenozoic sediments have densities between $1990 \text{ kg}/\text{m}^3$ and $2310 \text{ kg}/\text{m}^3$, which increase with depth (Fig. 4.3). The oceanic crustal densities are $2370 \text{ kg}/\text{m}^3$ for oceanic layer 2A, $2730 \text{ kg}/\text{m}^3$ for oceanic layer 2B, $2930 \text{ kg}/\text{m}^3$ for oceanic layer 3A, and $3050 \text{ kg}/\text{m}^3$ for oceanic layer 3B (>340 km, Fig. 4.3). Below the Kolbeinsey Ridge rift valley, the reduced crustal densities range between $2330 \text{ kg}/\text{m}^3$ and $3040 \text{ kg}/\text{m}^3$ (580 km, Fig. 4.3), indicating high porosity and higher temperatures of the young oceanic crust (Grevemeyer & Weigel 1996, Kodaira et al. 1997).

The mantle densities vary between $3220 \text{ kg}/\text{m}^3$ and $3300 \text{ kg}/\text{m}^3$ (Fig. 4.3). Low mantle densities can be found below the Kolbeinsey Ridge rift valley ($3220 \text{ kg}/\text{m}^3$) and further southeast ($3250 \text{ kg}/\text{m}^3$, >640 km, Fig. 4.3) representing thermal anomalies within the upper mantle (Kodaira et al. 1997, Schmidt-Aursch & Jokat 2005b).

Error Analysis

In general, the gravity model is consistent with our seismic refraction model. The standard deviation relative to the observed free-air anomaly is $70 \mu\text{m}/\text{s}^2$. Hence, the residuals are within the uncertainty of the gravity modelling method of $\pm 100 \mu\text{m}/\text{s}^2$ (Ljones et al. 2004). High residual values between the modelled and measured free-air anomaly of $-340 \mu\text{m}/\text{s}^2$ and $330 \mu\text{m}/\text{s}^2$ exist between 110 km and 200 km (Fig. 4.3). These residuals are the result of the pronounced non-straight geometry of line 94340, which experience difficulties in modelling (Chapter 3, Fig. 3.1C; Schlindwein 1998).

4 Gravity Data

Hence, the seismic rays do not travel along the projected seismic refraction line, and therefore sample different structures compared with the acquired gravity data. The maximum residual value of line 20090100 is $190 \mu\text{m}/\text{s}^2$ at 580 km (Fig. 4.3). This value corresponds to highly variable structures in the lower crust along the Kolbeinsey Ridge rift valley (Kodaira et al. 1997).

Comparison of gravity and seismic model

Regarding the P-wave and gravity model, thick sediments cover the basement offshore Kong Oscar Fjord (Chapter 3.3, Fig. 3.17). The sediment density of $2540 \text{ kg}/\text{m}^3$ is typical for Devonian rocks (180–340 km, Fig. 4.3; Schlindwein 1998). However, typical Devonian P-wave velocities of 5.5 km/s are not observed (Chapter 3.3, Fig. 3.17). Shallow intrusions within the sediments produce significant higher average densities of about $80 \text{ kg}/\text{m}^3$ compared with the surrounding sediment density values (240–280 km, Fig. 4.3). Based on geological investigations, the sediments are of Mesozoic age (Escher & Pulvertaft 1995, Schlindwein & Jokat 1999, Schlindwein & Meyer 1999).

Our densities of the continental crust are comparable with other results within the research area (Weigel et al. 1995, Schmidt-Aursch & Jokat 2005b). Small density differences of up to $100 \text{ kg}/\text{m}^3$ exist for the HVLC, which is within the error bars of the velocity-density relation (Figs. 3.16 and 4.3; Weigel et al. 1995, Schlindwein 1998, Schmidt-Aursch & Jokat 2005b, Voss & Jokat 2007).

The gravity low at the Kolbeinsey Ridge rift valley ($200 \mu\text{m}/\text{s}^2$) is smaller than at the Knipovich Ridge rift valley ($800 \mu\text{m}/\text{s}^2$, Chapter 4.1.2). Following Hall et al. (1986), this observation corresponds to a faster spreading at the Kolbeinsey Ridge compared with the Knipovich Ridge. Therefore, the amplitude and the wavelength of a mid-ocean free-air anomaly low decreases with increasing spreading rate of mid-ocean ridges. The result is a smooth topography of the mid-ocean rift valley and a small low-density root extending vertical into the mantle (Hall et al. 1986). At the Kolbeinsey Ridge, no pronounced mid-ocean rift valley and no low-density root exist (Fig. 4.3). In contrast, the Knipovich Ridge rift valley has a rough topography and a low-density

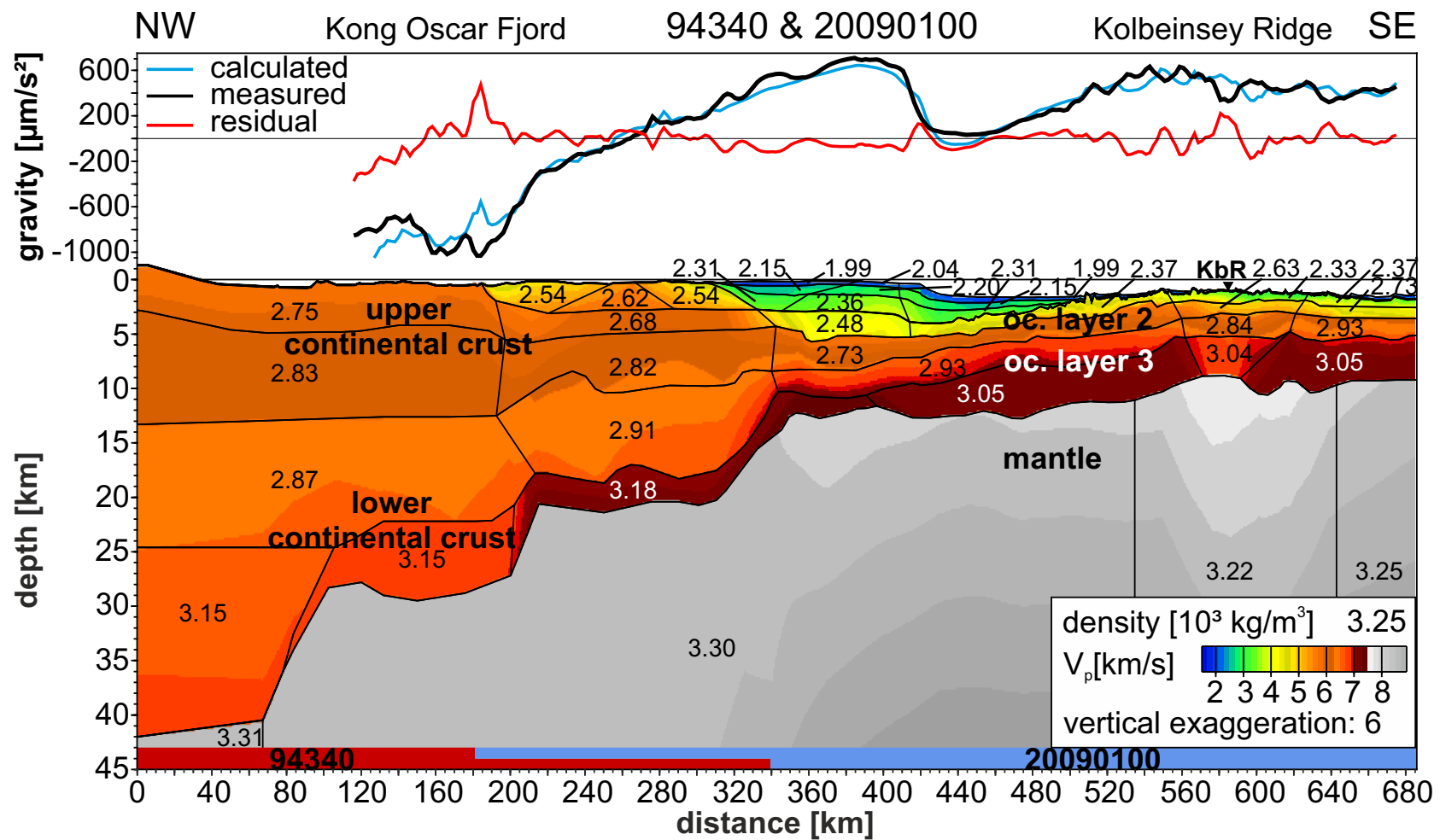


Figure 4.3: 2.5D gravity model based on the gravity data acquired parallel to lines 20090100 and 94340. The upper panel shows the observed and calculated free-air anomaly as well as the residuals (Hermann & Jokat 2013b).

4 Gravity Data

root extending into the mantle (Fig. 4.2). These facts describe the main differences between the ultraslow (Knipovich Ridge) and the slow spreading ridges (Kolbeinsey Ridge; Dick et al. 2003).

4.2 Gravimetric 3D Modelling

Combining all seismic refraction and 2D or 2.5D gravity models, a consistent 3D crustal model along the East Greenland margin can be achieved. The 3D gravity model of the research area was calculated using the software package *IGMAS+* (Götze & Lahmeyer 1988).

4.2.1 The Arctic Gravity Project (ArcGP)

For calculating the 3D gravity model of the eastern Norwegian-Greenland Sea, the public-domain Arctic Gravity Project grid (ArcGP, Kenyon et al. 2008) was used. The ArcGP is a compilation of the gravity field onto a 5'x5' grid of the free-air anomaly north of 64°N (Fig. 4.4; Kenyon et al. 2008). This database incorporates data from different measuring platforms: surface (e.g. Boebel 2000), airborne (Brozena et al. 1997, Forsberg et al. 2002), submarine (Edwards & Coakley 2003), and satellite (Laxon & McAdoo 1994, Forsberg & Skourup 2005). Following Forsberg & Kenyon (2004), the ArcGP includes atmospheric corrected free-air anomalies with reference to the World Geodetic System from 1984 (WGS84). The error of the ArcGP gravity grid can be estimated with approximately 20 $\mu\text{m}/\text{s}^2$ RMS and a resolution of 6 km (Forsberg & Kenyon 2001). For the subsequent 3D modelling, the latest ArcGP grid version (updated: March 19th, 2008) was used.

4.2.2 Boundary Conditions

Boundary conditions for 3D gravity modelling are necessary to reduce the ambiguity of potential methods (Blakely 1995). Thus, additional information of geology, tectonic, well logs, seismic lines, gravity models, and further geophysical datasets were used as boundary conditions (Tab. 4.1, Fig. 4.5).

Hence, the bathymetry (IBCAO, Jakobsson et al. 2012) and crustal structures like: (1) basement depth, (2) horizontal extension of continental crust, (3) boundary depth between upper and lower continental crust, (4) horizontal extension and thickness of

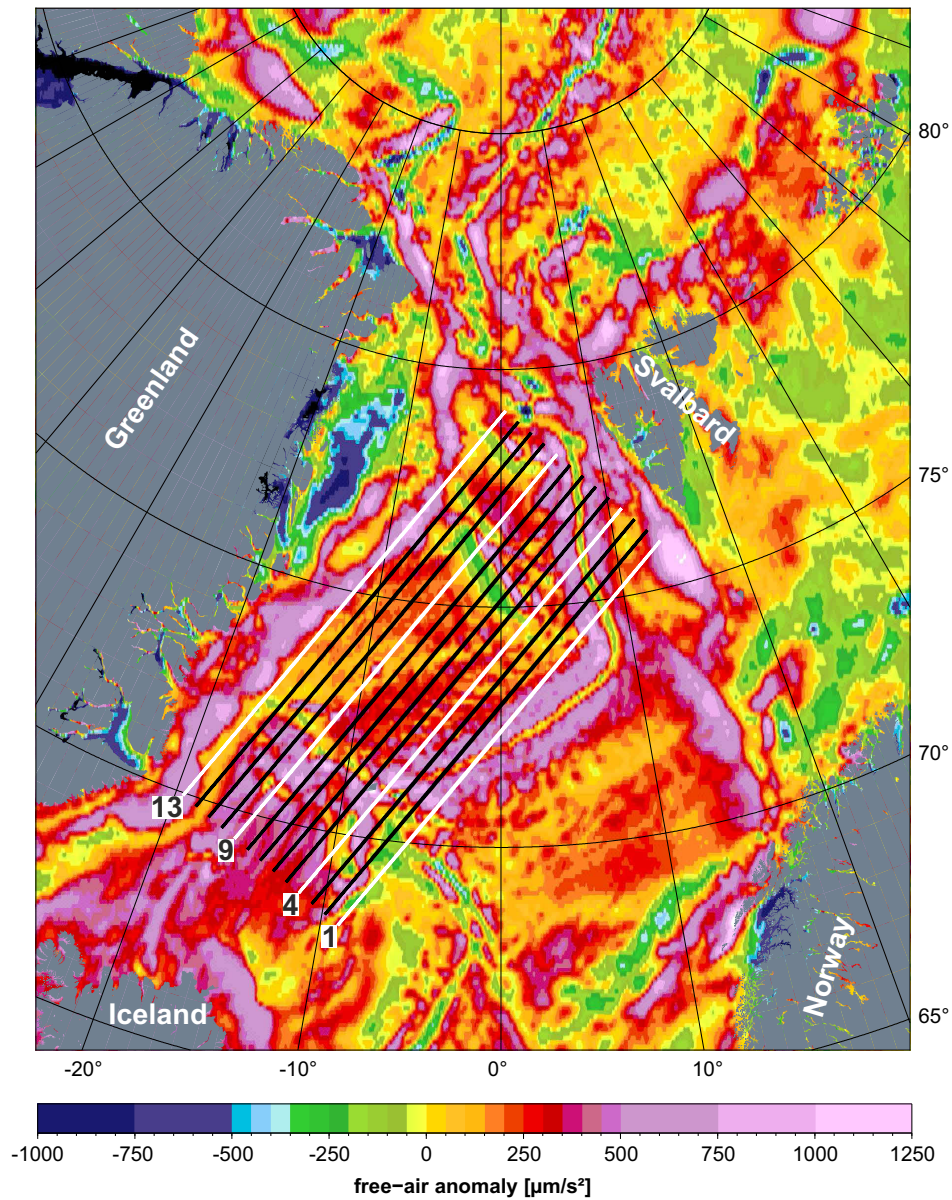





Figure 4.4: Free-air anomaly map of northern North Atlantic with a resolution of $5' \times 5'$ (ArcGP, Kenyon et al. 2008). The 13 sections of our 3D gravity model are shown. The four annotated white sections are presented in Chapter 4.2.3.

the HVLC, and (5) Mohorovičić (Moho) depth are available (Tab. 4.1, Fig. 4.5). Especially, depth-converted seismic reflection lines and well logs of the Ocean Drilling Programme (ODP) provide additional constraints for the basement depth. In addition, reconstructed plate boundaries of the Jan Mayen Micro-continent and the East Greenland margin indicate the horizontal extension of the continental crust.




Density information were gathered from: (1) our 2.5D gravity models (Chapter 4.1), (2) other 2D gravity models, (3) 3D gravity models next to the research area, and (4) bulk density logs of 14 ODP wells, drilled in the Norwegian-Greenland Sea (Tab. 4.1, Fig. 4.5). Based on these information, the sediments were divided into three layers and the continental crust into two layers (Tab. 4.2).

For deciding the distance between each section, a spectral analysis of the free-air anomaly was calculated (Fig. 4.6). The smallest significant peak within the power spectral density (PSD) of the free-air anomaly is at 80 km. To avoid alias effects, the distance between each section was set to 40 km. Hence, we focus on the interested large-scale gravity anomalies. Following Blakely (1995), these gravity anomalies have their source depths in the lower crust and upper mantle in the research area (4–66 km depth).

Table 4.1: Boundary conditions used for our 3D gravity model (Fig. 4.5). The boundary conditions for continental crust include the horizontal extension of the crust, and the depth of the boundary layer between upper and lower crust.

Data	Author	Feature in Fig. 4.5	Boundary Condition for ...
seismic refraction lines	Weigel et al. (1995), Kodaira et al. (1997) Kodaira et al. (1998a), Kodaira et al. (1998b) Schlindwein & Jokat (1999), Klingelhöfer et al. (2000) Ritzmann et al. (2002), Ljones et al. (2004) Ritzmann et al. (2004), Czuba et al. (2005) Voss & Jokat (2007), Døssing et al. (2008) Kandilarov et al. (2008), Voss et al. (2009) Kandilarov et al. (2010), Breivik et al. (2012) Jokat et al. (2012a), Kandilarov et al. (2012) line 20090200 (Chapter 3.2), line 20090100 (Chapter 3.3)		basement and Moho depth, horizontal extension and thickness of HVLC, horizontal extension and depth of boundary layer upper–lower continental crust
2D/2.5D gravity models (along seismic refraction lines)	Weigel et al. (1995), Schlindwein & Jokat (2000) Ritzmann et al. (2002), Ljones et al. (2004) Ritzmann et al. (2004), Mjelde et al. (2007) Voss & Jokat (2007), Døssing et al. (2008) Kandilarov et al. (2008), Voss et al. (2009) Kandilarov et al. (2010), Kandilarov et al. (2012) line 20090200 (Chapter 4.1.2), line 20090100 (Chapter 4.1.3)		density of sediments, crust, HVLC, and mantle
seismic reflection lines	Berger & Jokat (2008), Berger & Jokat (2009)		basement depth

Continued on the next page

Data	Author	Feature in Fig. 4.5	Boundary Condition for ...
3D gravity models	Schmidt-Aursch & Jokat (2005b), Winter (2011)	 (1), (2)	basement and Moho depth, horizontal extension and thickness of HVLC, horizontal extension and depth of boundary layer upper–lower continental crust, density of sediments, crust, HVLC, and mantle
bathymetry (IBCAO)	Jakobsson et al. (2012)	grey scale	bathymetry
bulk density logs (ODP)	Myhre et al. (1995a,b,c,d) Jansen et al. (1996a,b,c,d) Talwani et al. (1976a,b,c,d,e)	 907–909, 913 907, 985–987 344–348, 350	density of sediments, basement depth
modelled plate boundaries	Escher & Pulvertaft (1995), Scott (2000) Tsikalas et al. (2002), Gaina et al. (2009)	 (a), (b) (c), (d)	horizontal extension of continental crust

4 Gravity Data

Table 4.2: Densities of the 10 geological model bodies applied in our 3D gravity model. The reference body surrounds the entire 3D model.

Model Body	Density [kg/m ³]
Water	1030
Upper Sediments	1900
Middle Sediments	2100
Lower Sediments	2400
Upper Continental Crust	2700
Lower Continental Crust	2950
HVLC	3100
Oceanic Crust	2900
Mantle	3300
Reference	2670

4.2.3 The 3D Model

The 3D gravity model has an extension of 480 km x 1200 km x 50 km and consists of 13 sections (Fig. 4.5). The model area is extended by 2400 km in each direction to avoid boundary effects. The sections are NE–SW oriented, to cross the important geological provinces and ocean basins perpendicular (Fig. 4.5). The distance between each section is 40 km. The station spacing along each section is 10 km. Therefore, modelling of gravity anomalies with wavelengths > 20 km along the sections is possible.

The modelled mantle densities vary between 3200 kg/m³ and 3350 kg/m³ (Tab. 4.3). Higher densities of 3350 kg/m³, compared with the average mantle density of 3300 kg/m³, exist below the Greenland Basin and the Boreas Basin. In contrast, below the Knipovich Ridge, the Mohns Ridge, and the Kolbeinsey Ridge as well as below the Kolbeinsey Basin low mantle densities are observed (3200–3270 kg/m³, Tab. 4.3). The modelled mantle is shown in four exemplary sections from our 3D gravity model (Fig. 4.4): section 1 (Fig. 4.7), section 4 (Fig. 4.8), section 9 (Fig. 4.9), and section 13 (Fig. 4.10).

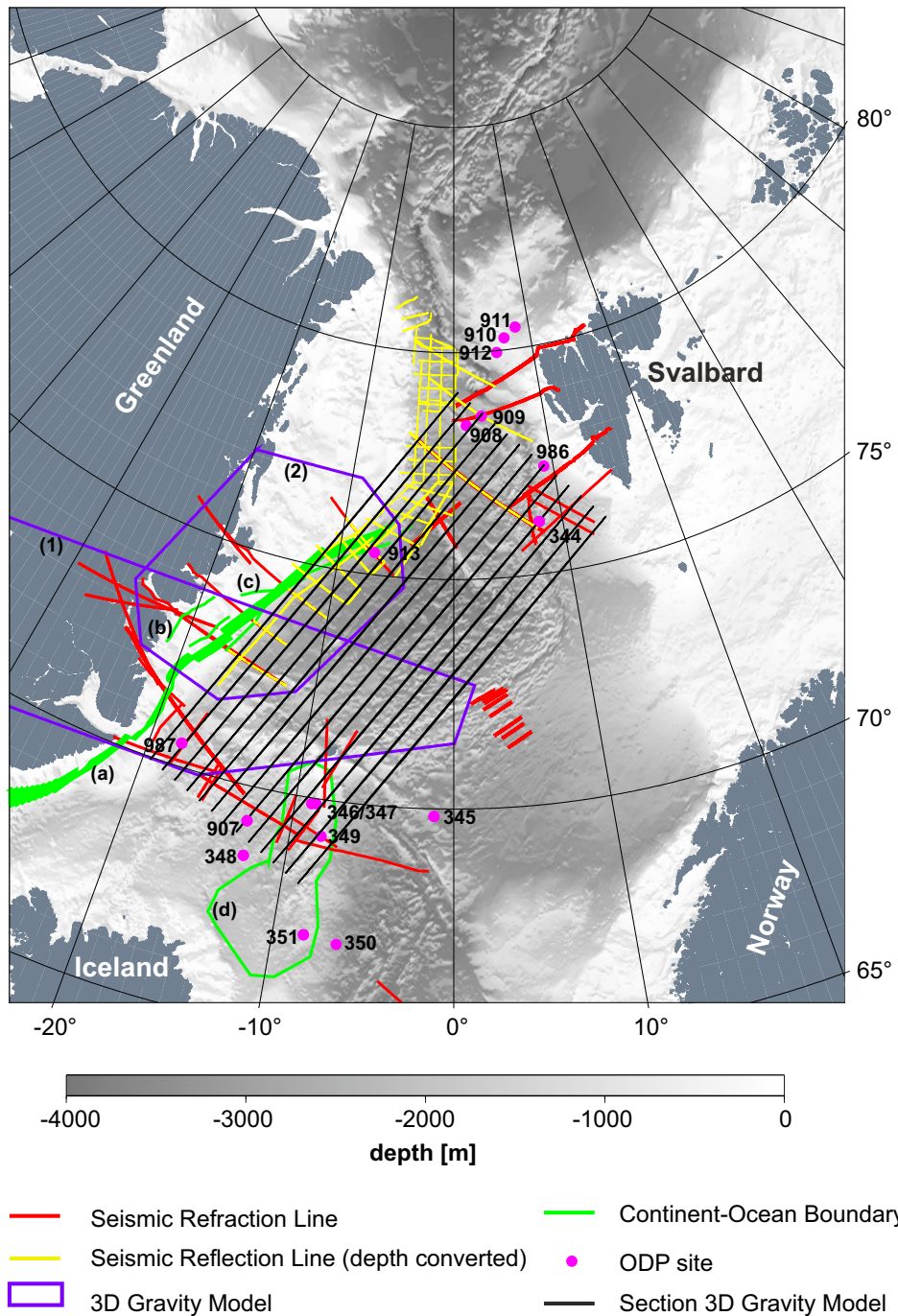


Figure 4.5: Boundary conditions used for the 3D gravity modelling. References for the used and shown data see Figure 2.2 and Table 4.1. The black lines show the 13 sections of our 3D gravity model.

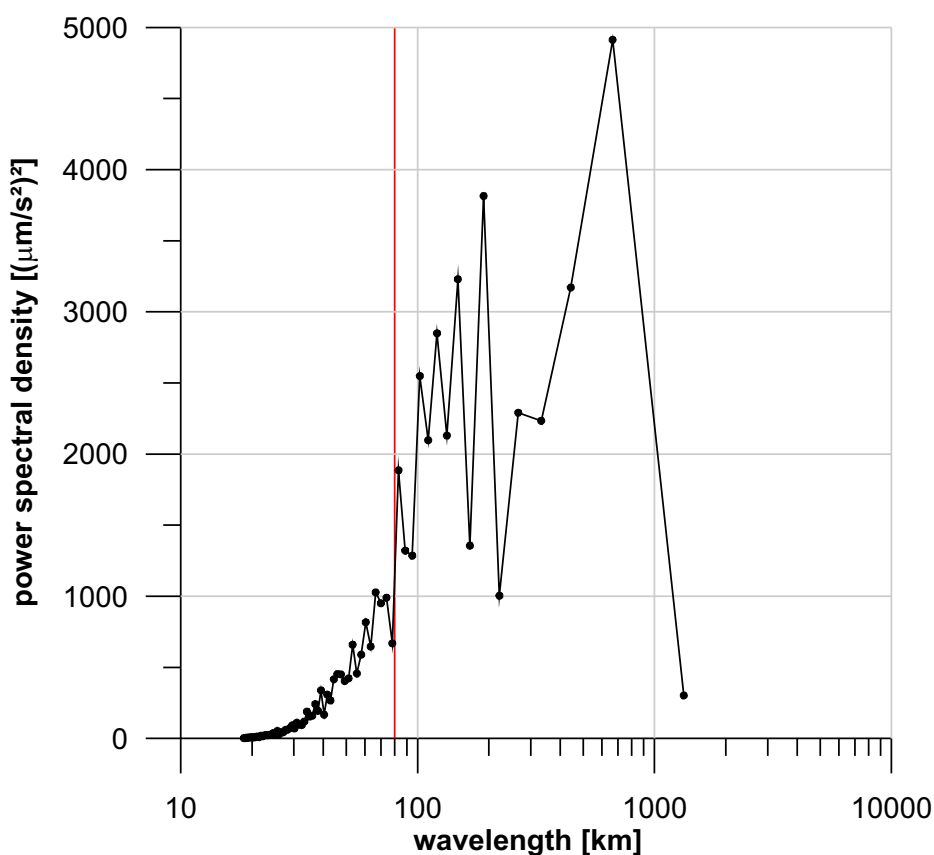


Figure 4.6: Power spectral density of the Greenland Sea free-air anomaly against the wavelength. The red line indicates the onset of the first significant local maximum at 80 km.

Table 4.3: Densities of the 6 mantle model bodies applied in the 3D gravity model. The mantle body "Mantle" represents normal mantle densities.

Model Body	Density [kg/m ³]
Mantle	3300
Greenland Basin & Boreas Basin	3350
Knipovich Ridge	3250
Kolbeinsey Basin	3250
Kolbeinsey Ridge	3200
Mohns Ridge	3270

Section 1

Section 1 is located in the middle of the Norwegian-Greenland Sea and crosses the eastern margin of the Jan Mayen Micro-continent, the Mohns Ridge, and the Knipovich Ridge (Fig. 4.7). To the north, the section terminates on the Barents Sea Shelf. The free-air anomaly varies between $-260 \mu\text{m/s}^2$ and $830 \mu\text{m/s}^2$. At the Mohns Ridge, a symmetric gravity low of $600 \mu\text{m/s}^2$ is observed (450–600 km, Fig. 4.7).

Thin sediments of less than 1 km thickness are modelled along the entire section, excluding the Barents Sea Shelf. Here, the sediments are 3 km to 4 km thick (>1050 km, Fig. 4.7). Above the Jan Mayen Micro-continent, the sediment thickness is 1 km (<100 km, Fig. 4.7). The continental crust of the Jan Mayen Micro-continent has a thickness of 9 km, increasing to 14 km below the Jan Mayen Ridge (50–150 km, Fig. 4.7). Below the Jan Mayen Micro-continent, a 2 km thick HVLC can be found (100–150 km, Fig. 4.7). The remaining part of section 1 shows oceanic crust with 3 km to 5 km in thickness. At the Jan Mayen Fracture Zone and at the Mohns Ridge, the crust is 5 km thick. Around the Knipovich Ridge area, the crust has an average thickness of 3 km (Fig. 4.7). The mantle near Mohns Ridge and Knipovich Ridge shows a low density of 3270 kg/m^3 compared with a normal mantle densities of 3300 kg/m^3 .

Section 4

Section 4 crosses the Jan Mayen Micro-continent and the eastern part of the Greenland Basin (Fig. 4.8). In addition, the most eastern point of the East Greenland Ridge and the Knipovich Ridge are passed. The free-air anomaly ranges between $-110 \mu\text{m/s}^2$ and $950 \mu\text{m/s}^2$. Two significant gravity lows are found along section 4 (Fig. 4.8): (1) at the Jan Mayen Fracture Zone with a value of $600 \mu\text{m/s}^2$ (300–350 km), and (2) at the Knipovich Ridge with a value of $700 \mu\text{m/s}^2$ (1000–1100 km).

The sediment thickness is similar to section 1 (less than 1 km), excluding the western Svalbard margin at the northern end of section 4. Here, the sediments are up to 3 km thick (>1150 km, Fig. 4.8). Below the Jan Mayen Micro-continent, continental crust is modelled (100–330 km, Fig. 4.8). In detail, below the Jan Mayen Basin, the

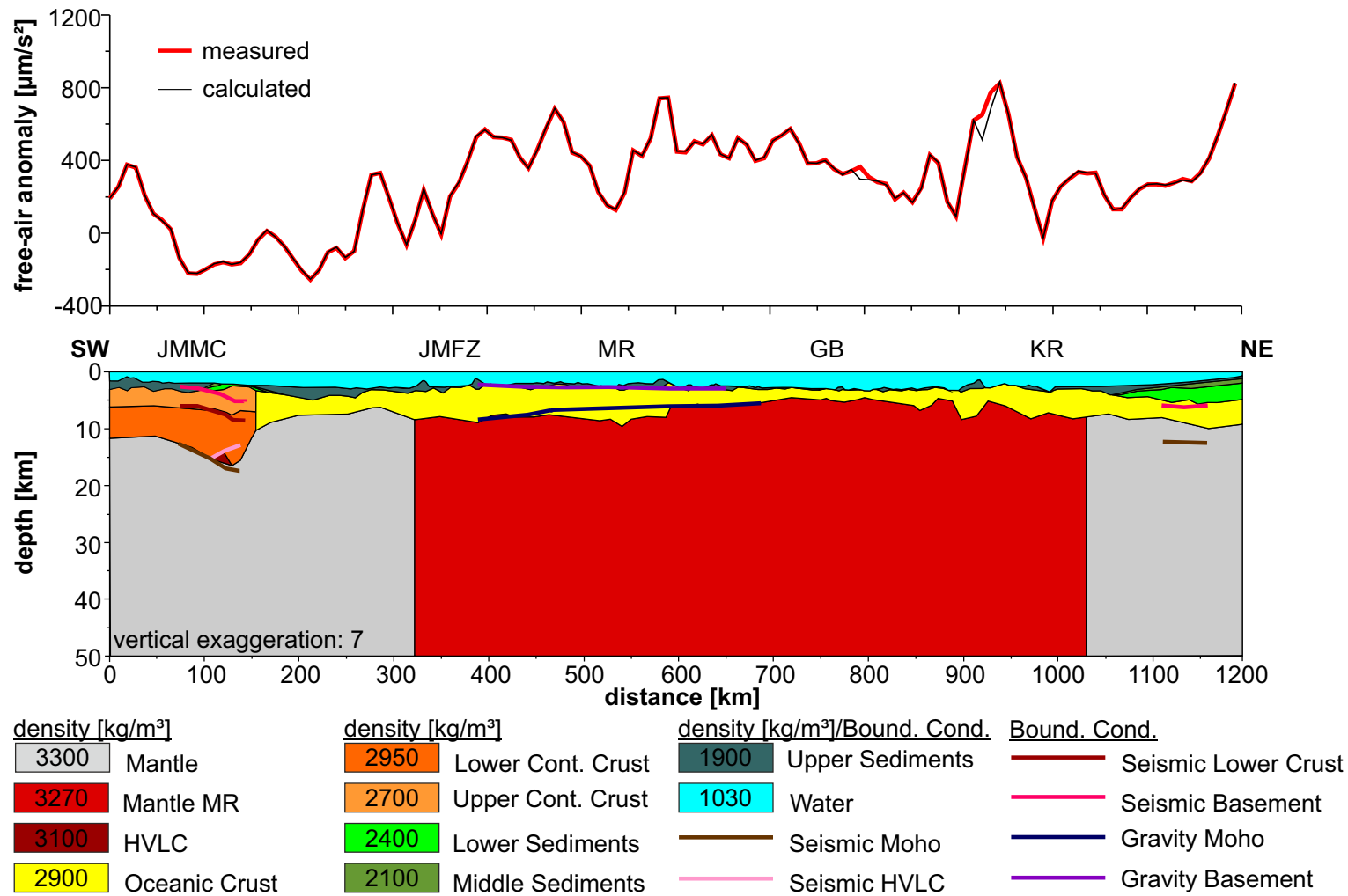


Figure 4.7: Section 1 crosses the Jan Mayen Micro-continent, the Mohns Ridge, and the Knipovich Ridge (Fig. 4.4). The lines in the lower panel show the boundary conditions based on seismic and gravity data (Fig. 4.5).

continental crust is 6 km thick, and increases to 25 km below the Jan Mayen Ridge. South of the Jan Mayen Micro-continent, the oceanic crust has a thickness of 9 km. In the the Greenland Basin and the Boreas Basin, the thickness of the oceanic crust varies between 3 km and 4 km. Below the Knipovich Ridge, the crustal thickness is 3 km (1030–1080 km, Fig. 4.8). The mantle density below the Mohns Ridge is 3270 kg/m^3 , and below the Knipovich Ridge 3250 kg/m^3 (Fig. 4.8).

Section 9

Section 9 starts at the Kolbeinsey Ridge and crosses the Greenland Basin, the East Greenland Ridge, and the Boreas Basin (Fig. 4.5). At 550 km (Fig. 4.9), the Vesteris Seamount is located in the Greenland Basin. The free-air anomaly varies between $-260 \mu\text{m/s}^2$ and $770 \mu\text{m/s}^2$. A symmetric gravity low of $400 \mu\text{m/s}^2$ and a width of 60 km is observed at the Proto-Jan Mayen Fracture Zone (PJMFZ, 160–200 km, Fig. 4.9). At the Jan Mayen Fracture Zone (260–380 km), a 120 km wide gravity low of $500 \mu\text{m/s}^2$ is found. In contrast, the Vesteris Seamount is characterised by a gravity high of $600 \mu\text{m/s}^2$ (500–550 km, Fig. 4.9). The East Greenland Ridge (900–950 km) is characterised by a gravity high of $800 \mu\text{m/s}^2$ and is flanked by two gravity lows of approximately $400 \mu\text{m/s}^2$.

The sediments have a thickness of less than 1 km along the entire section. Below the East Greenland Ridge, continental crust with a crustal thickness of 5 km exists (900–950 km, Fig. 4.9). Along the remaining part of section 9, oceanic crust is modelled. The thickness of the oceanic crust varies between 9 km in the Kolbeinsey Basin (0–300 km, Fig. 4.9), 5 km in the Greenland Basin (400–900 km), and 3 km to 4 km in the Boreas Basin (950–1200 km). At the Proto-Jan Mayen Fracture Zone the thickness decreases to 4 km (150 km, Fig. 4.9). The modelled mantle densities range between 3200 kg/m^3 and 3350 kg/m^3 along section 9. Increased densities of 3350 kg/m^3 are modelled below the Greenland Basin, the East Greenland Ridge, and the southern Boreas Basin (Fig. 4.9). In contrast, the mantle below the Kolbeinsey Basin (3250 kg/m^3) and below the Kolbeinsey Ridge (3200 kg/m^3) shows lower densities.

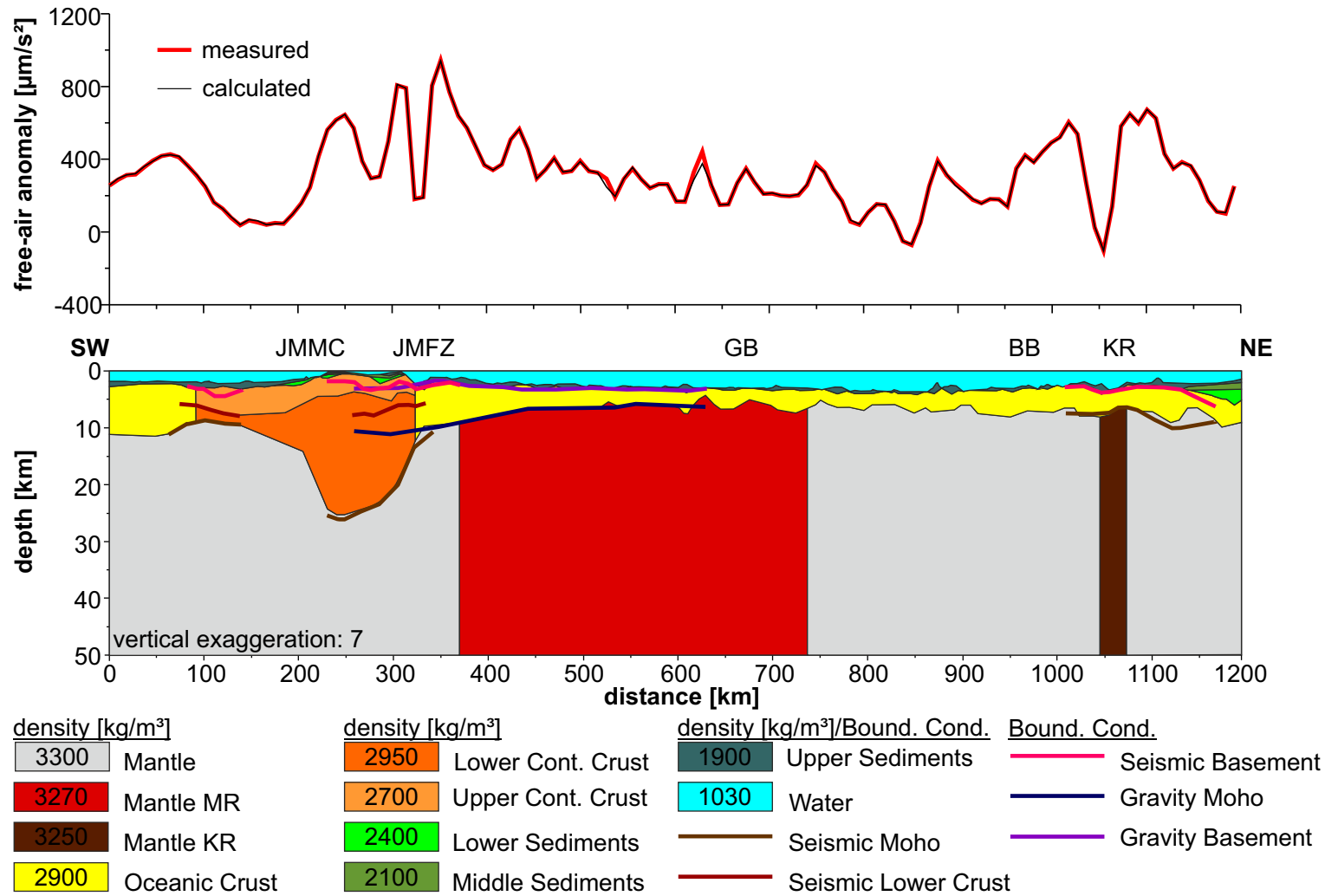


Figure 4.8: Section 4 crosses the Jan Mayen Micro-continent, the eastern part of the Greenland Basin, and the Knipovich Ridge (Fig. 4.4). The lines in the lower panel show the boundary conditions based on seismic and gravity data (Fig. 4.5).

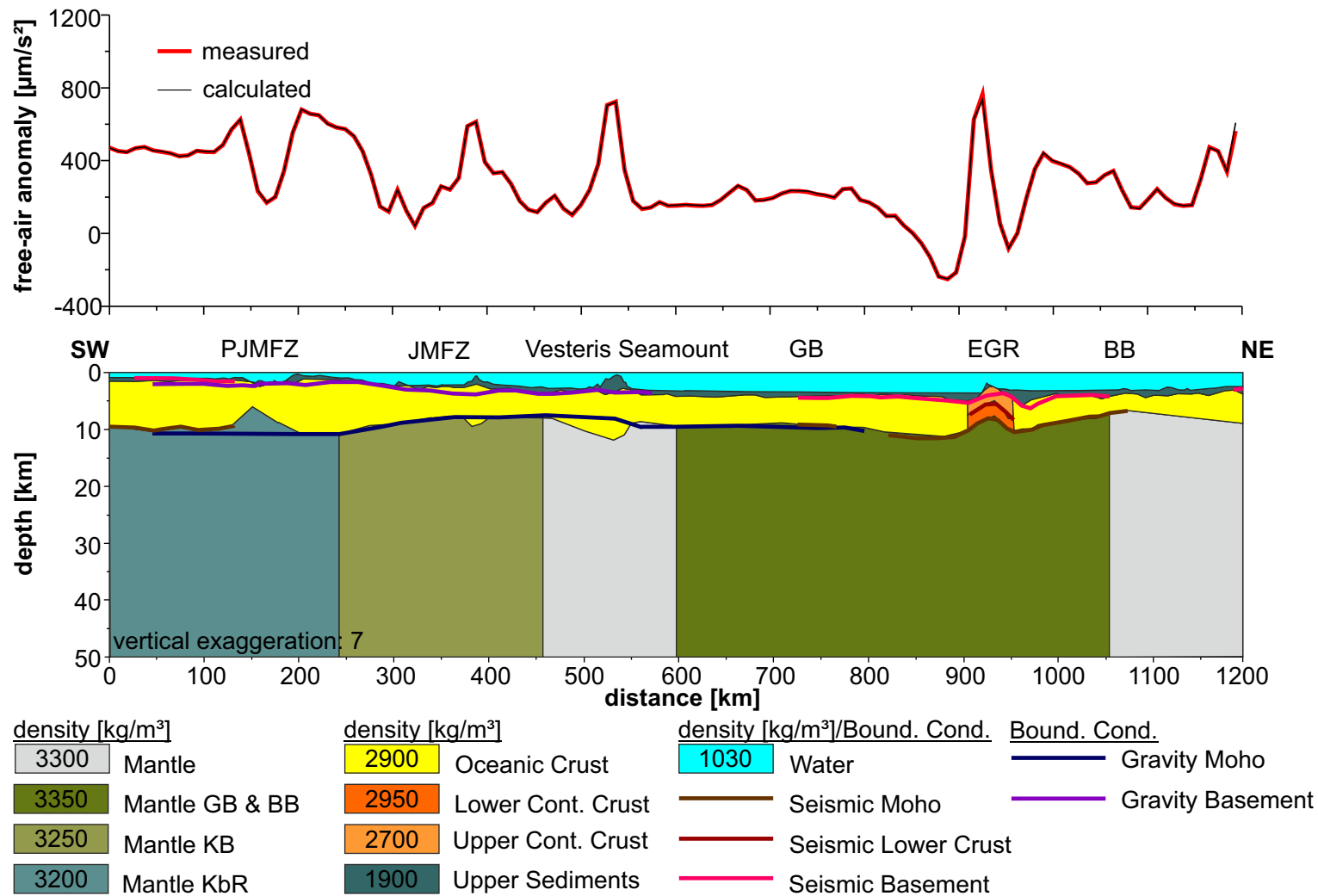


Figure 4.9: Section 9 starts at the Kolbeinsey Ridge and crosses the Greenland Basin, the East Greenland Ridge, and the Boreas Basin (Fig. 4.4). The lines in the lower panel show the boundary conditions based on seismic and gravity data (Fig. 4.5).

4 Gravity Data

Section 13

Section 13 starts offshore Scoresby Sund, runs along the East Greenland Shelf and across the Northeast Greenland Shelf to the Boreas Basin (Fig. 4.5). The free-air anomaly ranges between $-90 \mu\text{m/s}^2$ and $1020 \mu\text{m/s}^2$ (Fig. 4.10). At the Scoresby Sund Shelf, a gravity high of $600 \mu\text{m/s}^2$ is observed (<100 km, Fig. 4.10). On the Northeast Greenland Shelf (NEGS, 700–1000 km, Fig. 4.10), free-air anomaly values are larger than $500 \mu\text{m/s}^2$.

The thickness of the sediments varies between 1 km and 6 km (Fig. 4.10). Offshore Scoresby Sund, 6 km thick sediments are modelled (<70 km, Fig. 4.10). In the Greenland Basin and the Boreas Basin, the sediments are 1 km to 2 km thick. Above the Northeast Greenland Shelf, the sediment thickness is about 3 km (700–1000 km, Fig. 4.10). The continental crust below the Northeast Greenland Shelf shows a crustal thickness of 15 km to 18 km and has a rough basement topography. The thickness of the oceanic crust along the remaining part of section 13, range between 2 km and 14 km. Below the Scoresby Sund Shelf, the crustal thickness is 4 km (<70 km, Fig. 4.10). In contrast, below the Kolbeinsey Basin the oceanic crust is 10 km thick (70–300 km, Fig. 4.10). At the Jan Mayen Fracture Zone the crustal thickness increase to 14 km (290 km, Fig. 4.10). In the Greenland Basin the thickness of the oceanic crust is 8 km to 9 km (330–700 km, Fig. 4.10). In addition, the Greenland Basin is underlain by a 2 km to 3 km thick HVLC. Below the Boreas Basin, the oceanic crust has a thickness of 7 km to 9 km (1000–1200 km, Fig. 4.10). The mantle densities range between 3300 kg/m^3 and 3350 kg/m^3 . Higher densities of 3350 kg/m^3 are modelled below the Northeast Greenland Shelf and below the Boreas Basin (>580 km, Fig. 4.10).

Sediment thickness

The sediment thickness of our 3D gravity model ranges between 0 km and 6 km (Fig. 4.11). In the Kolbeinsey Basin, the Greenland Basin, and the Boreas Basin, the sediment thickness is less than 1 km, decreasing towards the active spreading mid-ocean ridges. In contrast, near the shelf and on the Jan Mayen Micro-continent, higher

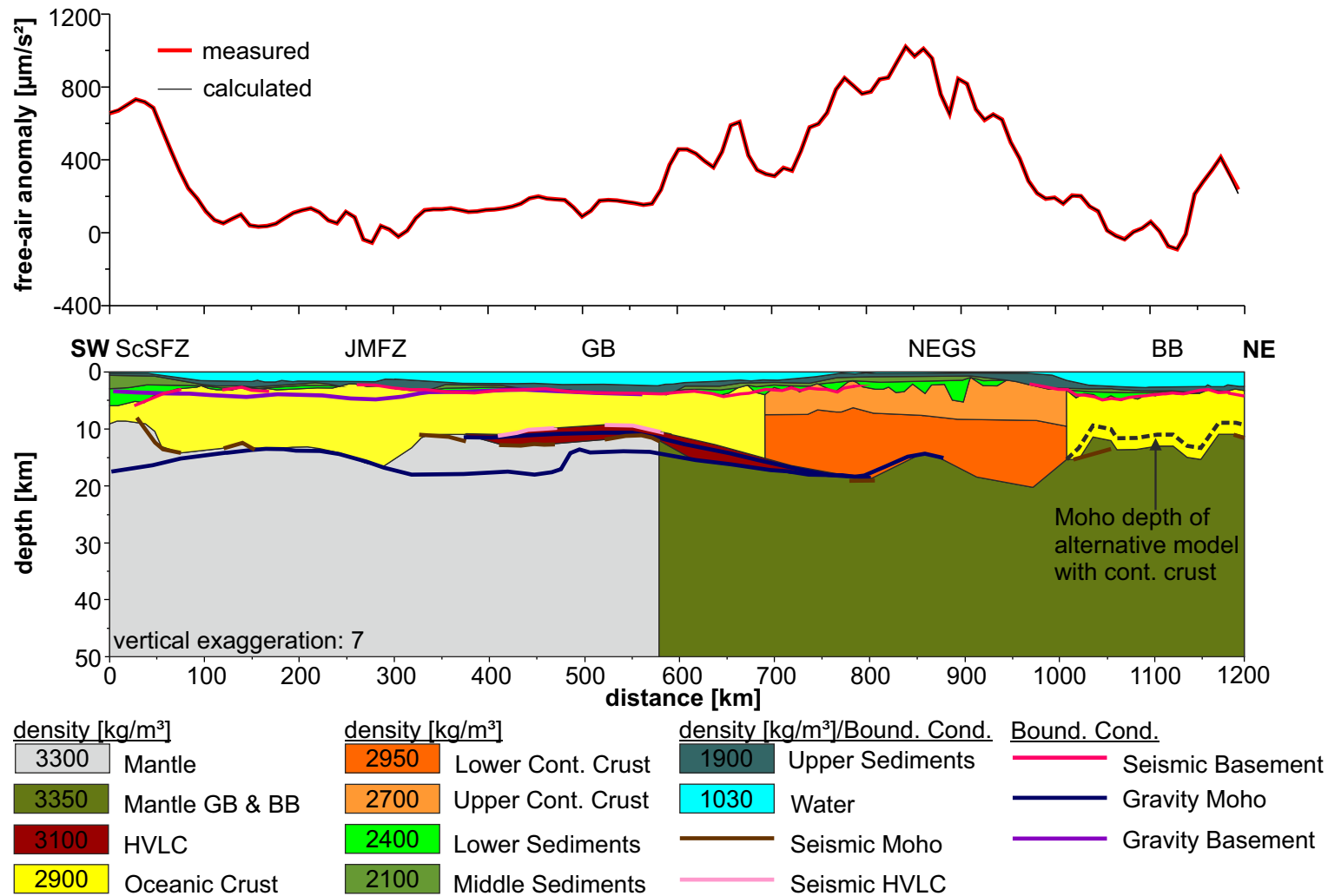


Figure 4.10: Section 13 starts offshore Scoresby Sund, runs along the East Greenland Shelf and across the Northeast Greenland Shelf to the Boreas Basin (Fig. 4.4). The lines in the lower panel show the boundary conditions based on seismic and gravity data (Fig. 4.5). The dashed line shows the Moho depth of an alternative model with continental crust in the Boreas Basin.

4 Gravity Data

sediment thicknesses are modelled (Fig. 4.11). Towards Svalbard and the Barents Sea Shelf, the sediment thickness is greater than 4 km. At the East Greenland Shelf, offshore Scoresby Sund, a sediment fan with up to 6 km thick sediments is located. Above the Northeast Greenland Shelf and in the western part of the Boreas Basin, the sediments are 3 km thick (Fig. 4.11). Near the Jan Mayen Micro-continent, the sediment thickness is about 2 km, especially in the area of the Jan Mayen Basin (western part of the Jan Mayen Micro-continent). In the western part of the Boreas Basin, N–S to NW–SE running, narrow, linear depocentres are found (Fig. 4.11). The depocentres have a sediment thickness of approximately 1 km.

Crustal thickness

The crustal thickness of our 3D gravity model ranges between 2 km and 23 km (Fig. 4.12). The oceanic crust in the Greenland Basin and the Boreas Basin, is consistently thin with values between 3 km and 4 km. At the Jan Mayen Fracture Zone, the thickness of the oceanic crust significantly increases within 50 km (from 4 km to 9 km). South of the Jan Mayen Fracture Zone, in the the Kolbeinsey Basin, 8 km to 9 km thick oceanic crust are modelled (Fig. 4.12). Furthermore, thick oceanic crust exists towards the Northeast Greenland Shelf with a maximum value of 10 km.

The continental crust at the Northeast Greenland Shelf is modelled with a thickness of 15 km maximum (Fig. 4.12). The Jan Mayen Micro-continent has a crustal thickness of 7 km to 13 km below the Jan Mayen Basin and below the Jan Mayen Ridge, respectively. To the southeast of Jan Mayen island, the crustal thickness of the Jan Mayen Micro-continent has its local maximum of 23 km.

4.2.4 Residuals

The modelled free-air anomaly match closely with the observed gravity values (Figs. 4.13A, B). The quality of a 3D gravity model can be evaluated by residuals which are defined as the deviation between modelled and observed free-air anomalies. For our 3D gravity model the residuals range between $-240 \mu\text{m/s}^2$ and $70 \mu\text{m/s}^2$ (Fig. 4.13C). The stan-

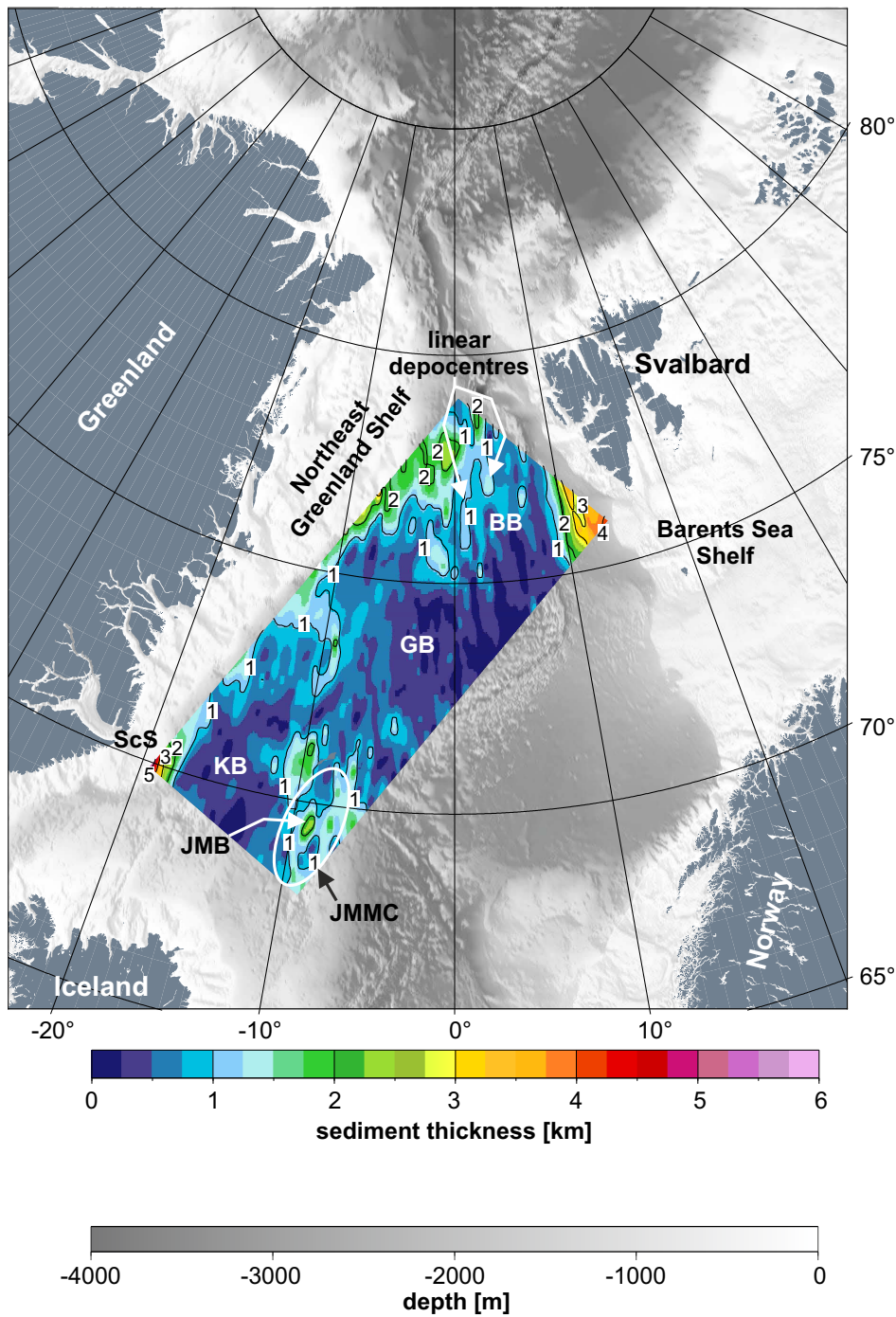


Figure 4.11: Sediment thickness resulting from our 3D gravity model.

4 Gravity Data

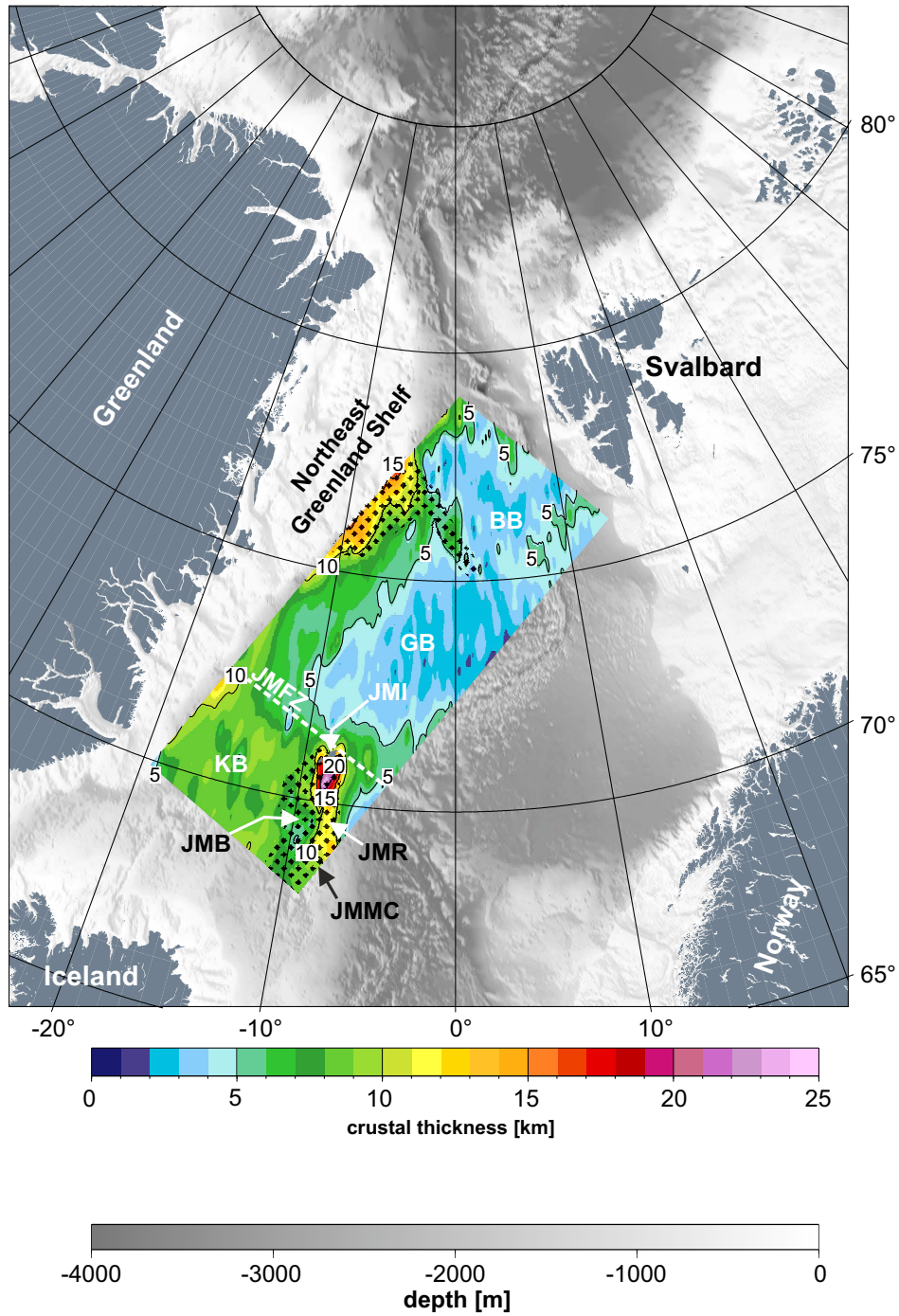


Figure 4.12: Crustal thickness resulting from our 3D gravity model. Dotted areas mark continental crust.

standard deviation (SD) for our 3D gravity model is $\pm 10 \mu\text{m/s}^2$. In most regions of our model, the residuals are less than $\pm 5 \mu\text{m/s}^2$. The results are comparable with other gravity models in Arctic regions (Tab. 4.4). In detail, our residuals are 10-fold smaller than these published by Schmidt-Aursch & Jokat (2005b) and Winter (2011), because we used more boundary conditions for our 3D gravity model (Tab. 4.4). In contrast, the 3D gravity model of Hegewald (2012) from the high Arctic Ocean show similar residuals.

Table 4.4: Comparison of different 3D gravity models in the Arctic region (Schmidt-Aursch & Jokat 2005b, Maystrenko & Scheck-Wenderoth 2009, Winter 2011, Hegewald 2012) regarding data uncertainties and model residuals. For modelling either the free-air anomaly (FA), the bouguer anomaly (BA), or a combination of both was used.

Reference	Data [$\mu\text{m/s}^2$]	Gravity Model		Remarks
		Range [$\mu\text{m/s}^2$]	SD [$\mu\text{m/s}^2$]	
Schmidt-Aursch & Jokat (2005b)	± 500	-700...500	± 100 (ocean.) ± 250 (cont.) ± 200 (overall)	BA without topographical correction
Maystrenko & Scheck-Wenderoth (2009)	± 70	-400...500	± 100	BA (onshore), FA (offshore)
Winter (2011)	± 9	0...4000	± 1250	BA
Hegewald (2012)	± 20	-30...30	± 5	FA (ArcGP)
our study	± 20	-240...70	± 10	FA (ArcGP)

Locally, large residuals exist due to short-wavelength structures, for example near the Jan Mayen Micro-continent, at the Vesteris Seamount, and at the Hovgård Ridge (Fig. 4.13C). In addition, short-wavelength residuals in the eastern part of our 3D gravity model indicate a rough basement topography. Larger residuals are concentrated at the northern and eastern boundary of our 3D gravity model, showing boundary effects due to the homogeneous model extension.

The model uncertainties were estimated by model perturbations (variations in depth)

of single boundary nodes until the residuals are greater than the uncertainty of the observed free-air anomaly. This method is similar to estimations of uncertainties for seismic refraction models (Chapter 3.1.4). The uncertainties were estimated with ± 0.3 km for the basement and ± 1.0 km for the crust-mantle boundary. However, the ambiguity of potential methods (Blakely 1995) is not included in the uncertainty investigation.

4.2.5 Discussion of the 3D Gravity Model

Comparison of Crustal Structures from Boundary Conditions and 3D Gravity Model

In general, the results of our 3D gravity model match well with the crustal structures from the used boundary conditions. However, some deviations of crustal structures between boundary conditions and our 3D gravity model exist. Near the Jan Mayen Micro-continent, the basement topography deviation is up to 2 km (Fig. 4.8). At the eastern margin of the Jan Mayen Micro-continent, the basement is 1 km shallower in our 3D gravity model than in the seismic refraction data of Kodaira et al. (1998a, 100–150 km, Fig. 4.8). The 2.5D gravity model of Mjelde et al. (2007) indicates locally high sediment densities of about 2600 kg/m^3 , resulting in a shallower basement topography in our 3D gravity model. At the western margin of the Jan Mayen Micro-continent, the basement is 2 km shallower in the 3D gravity model than in the seismic refraction lines (100–150 km, Fig. 4.7; Breivik et al. 2012). This can be explained by seaward-dipping reflectors and intrusions with higher densities of 2500 kg/m^3 to 2600 kg/m^3 (Mjelde et al. 2007, Peron-Pinvidic et al. 2012a,b). Hence, the shallower basement in our 3D gravity model compared with the seismic refraction data of Kandilarov et al. (2012), at the northern boundary of the Jan Mayen Micro-continent (230–330 km, Fig. 4.8), can be explained.

In the Greenland Basin, significant crust-mantle boundary deviations between our 3D gravity model and the 3D gravity model of Schmidt-Aursch & Jokat (2005b) exist. The deviations have maximum values of 5 km (300–600 km, Fig. 4.10). The new seismic refraction lines of Voss & Jokat (2007) and Voss et al. (2009) show detailed information

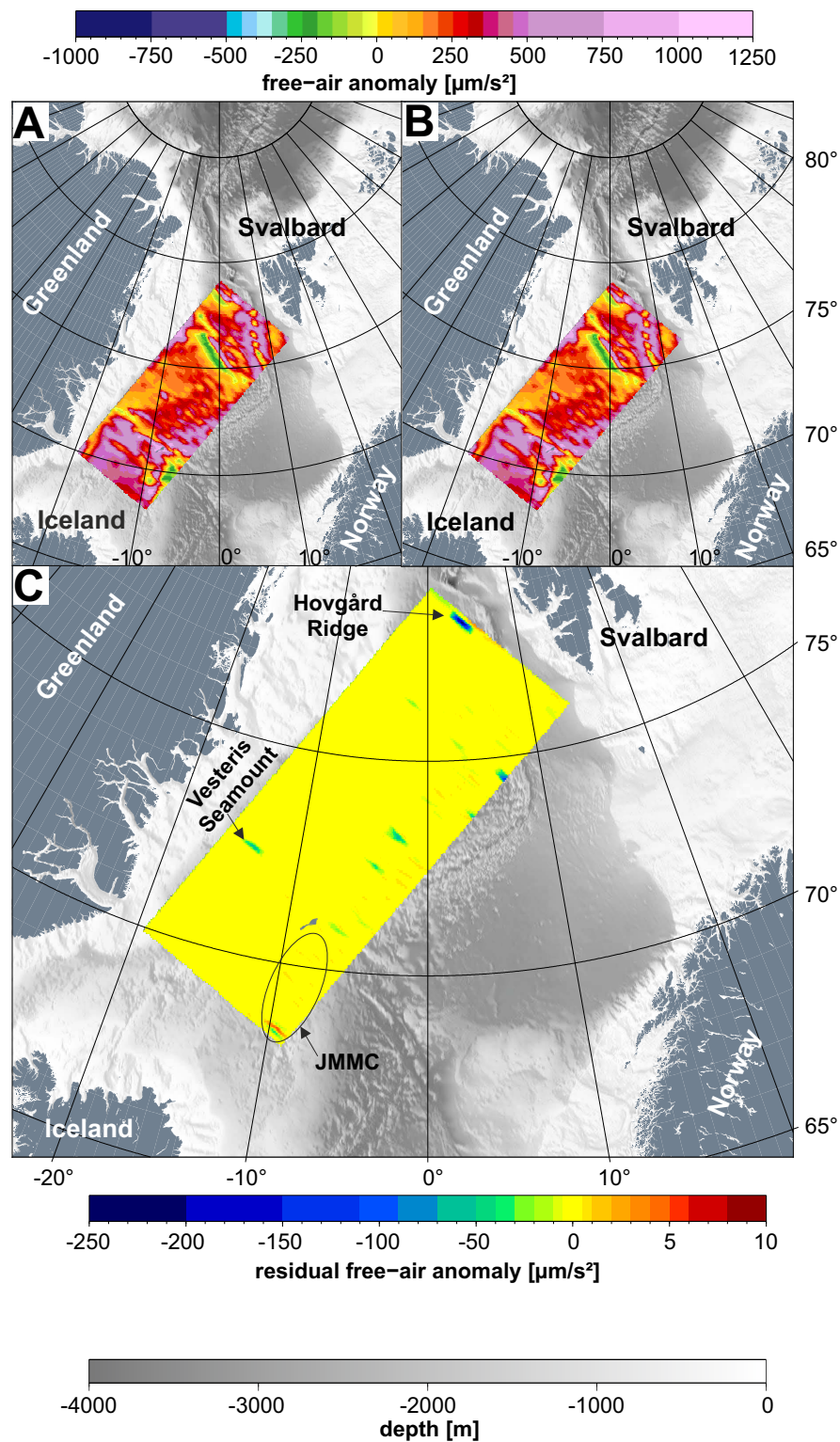


Figure 4.13: (A) Measured, (B) calculated, and (C) residual free-air anomaly of our 3D gravity model. Yellow areas indicate residuals of less than $\pm 5 \mu\text{m/s}^2$.

4 Gravity Data

about the Greenland Basin. These seismic refraction lines we used as boundary conditions for our modelling. Furthermore, small-scale crust-mantle boundary deviations up to 1 km between the 3D gravity model of Schmidt-Aursch & Jokat (2005b) and our 3D gravity model exist: (1) at the Vesteris Seamount (500–550 km, Fig. 4.9), and (2) at the Proto-Jan Mayen Fracture Zone (125–175 km, Fig. 4.9). These small-scale structures could not be modelled by Schmidt-Aursch & Jokat (2005b), because of the section parallel location of the structures. Below the Mohns Ridge, the crust-mantle boundary is approximately 2 km deeper in our 3D gravity model than by Schmidt-Aursch & Jokat (2005b, 450–600 km, Fig. 4.7). Reason for this is the location of the Mohns Ridge at the boundary of our 3D gravity model, and therefore, a detailed modelling of the crust-mantle boundary was not possible.

At the East Greenland Ridge, the basement in the seismic refraction data (Døssing et al. 2008) is about 1 km deeper than in our 3D gravity model (925–950 km, Fig. 4.9). In contrast, Døssing et al. (2008) also show basement outcrops in their seismic reflection data supporting our modelling results.

At the western margin of the Boreas Basin, the crust-mantle boundary is 2 km shallower in our 3D gravity model than in our seismic refraction line 20090200 (1025–1075 km, Fig. 4.10; Hermann & Jokat 2013a). The deviation is the result of the locally low ray coverage at the most western point of line 20090200. Therefore, less seismic waves of the crust-mantle boundary are gathered and uncertainties up to 2 km are possible. However, if continental crust instead of oceanic crust is modelled in the most western part of the Boreas Basin, as suggested by Engen et al. (2008), the crustal thickness would decrease by 2 km (1025–1200 km, Fig. 4.10). East of the Boreas Basin and at the Knipovich Ridge, the modelled crust-mantle boundary is approximately 2 km shallower in our 3D gravity model than in the seismic refraction lines of Kandilarov et al. (2008, 2010, 1100–1150 km, Fig. 4.7; 1125–1175 km, Fig. 4.8). The deviations can be explained by higher crustal and mantle densities of 3250 kg/m^3 and 3500 kg/m^3 , respectively, used by Kandilarov et al. (2008, 2010), compared with our density values (Tabs. 4.2 and 4.3).

Regarding the mantle densities, variations are generally related to thermal variations in the upper mantle (e. g. Breivik et al. 1999, Engen et al. 2006, Greenhalgh & Kuszniir 2007). In our 3D gravity model, the mantle densities reveal significant differences between the Kolbeinsey Basin and the area north of the Jan Mayen Fracture Zone, namely the Greenland Basin and the Boreas Basin (Fig. 4.14). Thus, indicating that crustal accretion at the Kolbeinsey Ridge is affected by the rift history and high mantle temperatures (Chapter 3.3).

Another explanation for the low mantle densities below the Kolbeinsey Basin might be isostatic anomalies (Menke 1999). However, Hooft et al. (2006) showed that the Kolbeinsey Basin is isostatically compensated because the topography directly depends on the crustal thickness. Hence, different seafloor elevations are due to different crustal thicknesses. Only below Iceland isostatical anomalies are existent (Hooft et al. 2006). Consequently, isostatical anomalies in the Kolbeinsey Basin might have minor influences and can be neglected.

Small-scale Segmentation in the Boreas Basin

The deviations between the crust-mantle boundary of our 3D gravity model and seismic refraction lines at the Knipovich Ridge (Ljones et al. 2004, Kandilarov et al. 2008, 2010) can also be explained by small-scale segmentation along ultraslow spreading ridges, as discussed along our seismic refraction line 20090200 (Chapter 3.2). Hence, thicker oceanic crust, which is produced at magmatic centres, is not sampled in our 3D gravity model due to the model configuration (section orientation of NE–SW, section spacing of 40 km, station spacing of 10 km). Based on this, the modelling of the small-scale segmentation along the Knipovich Ridge (segmentation length ~ 25 km; Okino et al. 2002) is not possible.

The segmentation at ultraslow spreading ridges can explain the observed linear depocentres in the western part of the Boreas Basin (Fig. 4.11). Periods of low magmatic activity produce amagmatic sections with smooth basement topography and thin crust. During this period, small sediment basins evolve (Fig. 3.11) and linear depocentres

4 Gravity Data

emerge parallel to the spreading direction along the track of magmatic segments or parallel to the active mid-ocean ridge. Following Engen et al. (2006) and Døssing et al. (2008), more linear depocentres in the Boreas Basin exist.

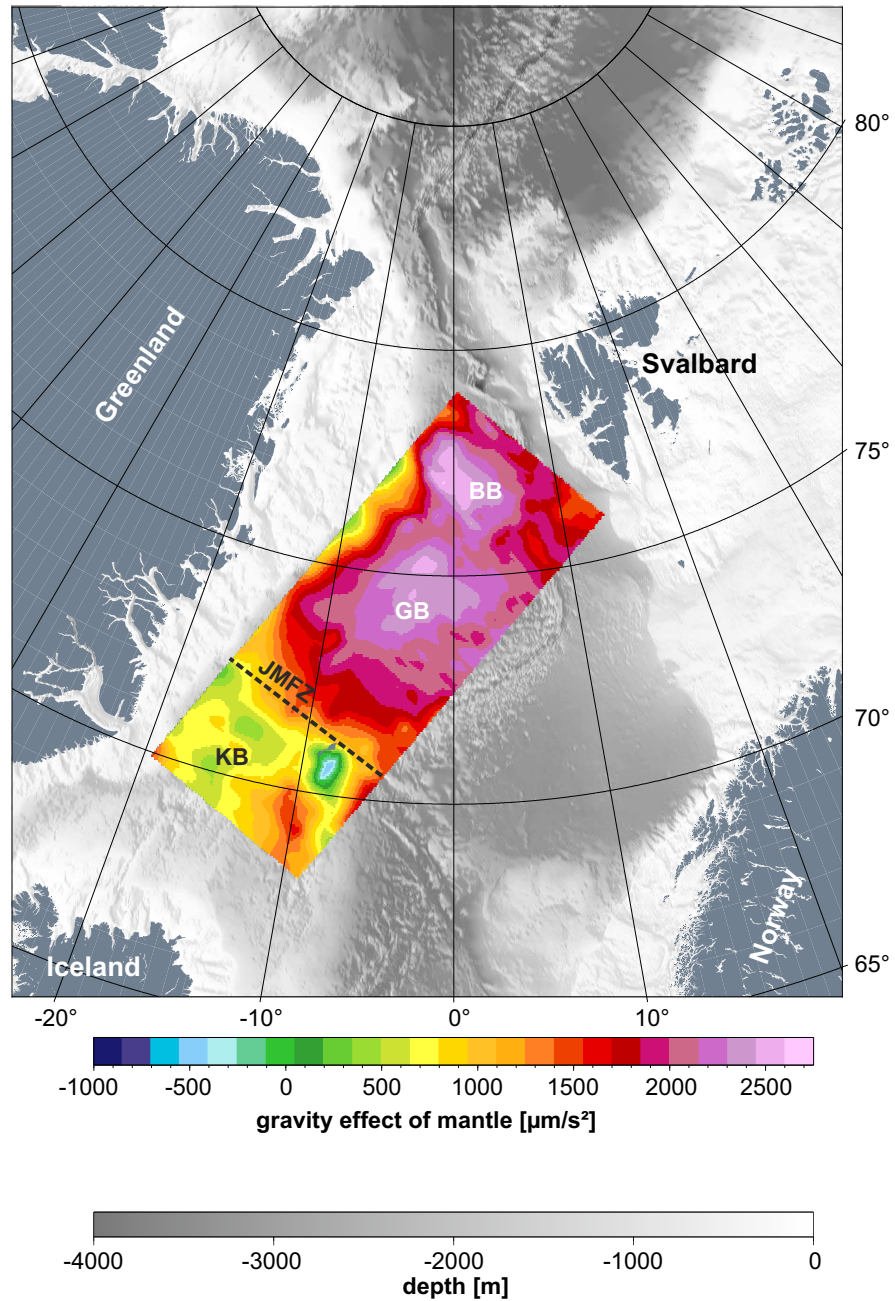


Figure 4.14: Gravity effect of the mantle. Smaller values are modelled in the Kolbensey Basin compared with the Greenland Basin and Boreas Basin.

5 Crustal Variations along the Northeast Greenland Margin

The three ocean basins within our research area – Boreas Basin, Greenland Basin, and Kolbeinsey Basin – evolved at ultraslow to slow spreading mid-ocean ridges. For the Boreas Basin and the Greenland Basin, the relation of oceanic crustal thickness to spreading rate fits well (Fig. 5.1). However, the Kolbeinsey Basin does not fit the general trend of this relation. In contrast, the conjugate Norway Basin, east of the Jan Mayen Micro-continent, is within the general oceanic crustal thickness to spreading rate trend (Breivik et al. 2006).

Interpreting the results, the oceanic crustal accretion at the Kolbeinsey Ridge is significantly influenced by processes in the mantle. However, the Iceland Hotspot and the subsequent high mantle temperatures might not be the main reason for these processes (Chapter 3.3.3). This is supported by the thin crust of the Norway Basin, which is typical for reduced melt generation.

5.1 Iceland Hotspot

In general, the accretion of thick oceanic crust and the formation of volcanic rifted margins are related to hotspots (e. g. White & McKenzie 1989, White et al. 1992). Hotspots are regions of long-lived voluminous volcanism and enhanced melt generation. They are located on mid-ocean ridges (like Iceland) or on lithospheric plates (like Hawaii; Sleep 2006). A popular model for the Iceland Hotspot assumes that it is caused by a deep mantle plume (e. g. White & McKenzie 1989, White et al. 1992). Deep mantle plumes are of simple cylindrical geometry (100–400 km in diameter) consisting of hot material, which ascend buoyantly (Morgan 1971, Sleep 2006). The mantle plumes start from "Plume Generation Zones" (named after Burke et al. 2008) which are located at the core-mantle boundary. Here, "Low S-wave Velocity Provinces" exist, which are defined as regions with reduced S-wave velocities. The mantle plumes ascend

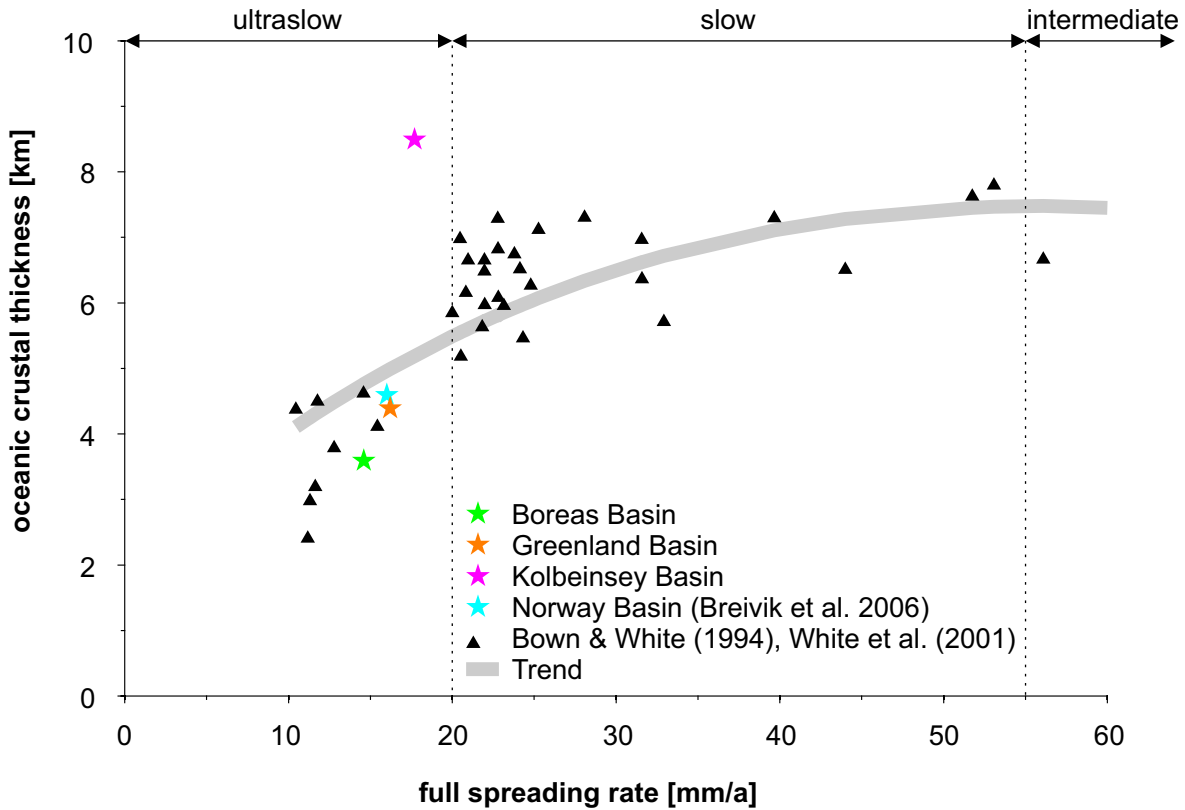


Figure 5.1: Crustal thickness versus spreading rate for ultraslow and slow spreading mid-ocean ridges (Dick et al. 2003). The Kolbeinsey Basin does not fit the general trend of this relation.

from the boundaries of these low S-wave velocity provinces, which are defined by the 1% reduced S-wave velocity contour line ($\delta V_s \approx -1\%$; Burke & Torsvik 2004). Here, subducted slabs can trigger starting mantle plumes as described in popular models (e. g. Steinberger & Torsvik 2012). When the head of the mantle plume arrives the base of the lithosphere, a brief episode of flood basalts, mafic crustal intrusions, and radial dyke swarms occur (Sleep 2006).

The subsequent formation of volcanic margins and thick oceanic crust can also be explained by alternative models, including: (1) delamination, (2) dynamic rifting (active upwelling), (3) small-scale rift related convection, and (4) chemical mantle heterogeneities (see Meyer et al. 2007 and Voss et al. 2009 for review). Based on this and unexplained aspects of all models, the existence and the influence of a deep mantle

plume below Iceland remains controversial (e. g. Foulger & Anderson 2005, Meyer et al. 2007, Mjelde et al. 2008b, Voss et al. 2009).

Based on our results, we can give some new information about the Iceland Hotspot, regarding: (1) the Boreas Basin and the Knipovich Ridge, (2) the Jan Mayen Fracture Zone, and (3) the Kolbeinsey Basin and the Kolbeinsey Ridge. In the Boreas Basin and at the Knipovich Ridge, thin oceanic crust without a significant oceanic layer 3 does not show any influence of the Iceland Hotspot on the crustal accretion.

At the Jan Mayen Fracture Zone, the thickness of the high-velocity lower crust (HVLC) decreases away from the fracture zone. This observation indicates that enhanced melt generation along the Jan Mayen Fracture Zone formed the HVLC below Kong Oscar Fjord and thickened the HVLC north of the fracture zone. Hence, the enhanced melt generation along the Jan Mayen Fracture Zone is unrelated to the Iceland Hotspot.

In the Kolbeinsey Basin, thick oceanic crust is based on the rift history and high mantle temperatures. In general, high mantle temperatures are associated with low S-wave velocities in the mantle (e. g. Burke & Torsvik 2004, Rickers et al. 2013). Hence, the area of thick oceanic crust in the Kolbeinsey Basin is compared with a global seismic tomography model (Fig. 5.2; Ritsema et al. 2011). Following the $\delta V_s = -1.25\%$ contour lines for various depths (200–700 km depth), the contour lines run in parallel to the boundaries of the Kolbeinsey Basin, especially the Jan Mayen Fracture Zone and the eastern margin of the Jan Mayen Micro-continent (Fig. 5.2). Therefore, high mantle temperatures might be present below the entire Kolbeinsey Basin. However, low S-wave velocities in the mantle are also observed west of Svalbard (300–600 km depth), indicating that the rift history is more important than higher temperatures. This conclusion is based on the accretion of thin crust at the Knipovich Ridge, even though low S-wave velocities are observed in the mantle.

Regarding our conclusion, the Iceland Hotspot is not the main origin for the accretion of thick oceanic crust, which results in a smaller influence of the Iceland Hotspot on the evolution of the research area than previously thought.

5 Crustal Variations along the Northeast Greenland Margin

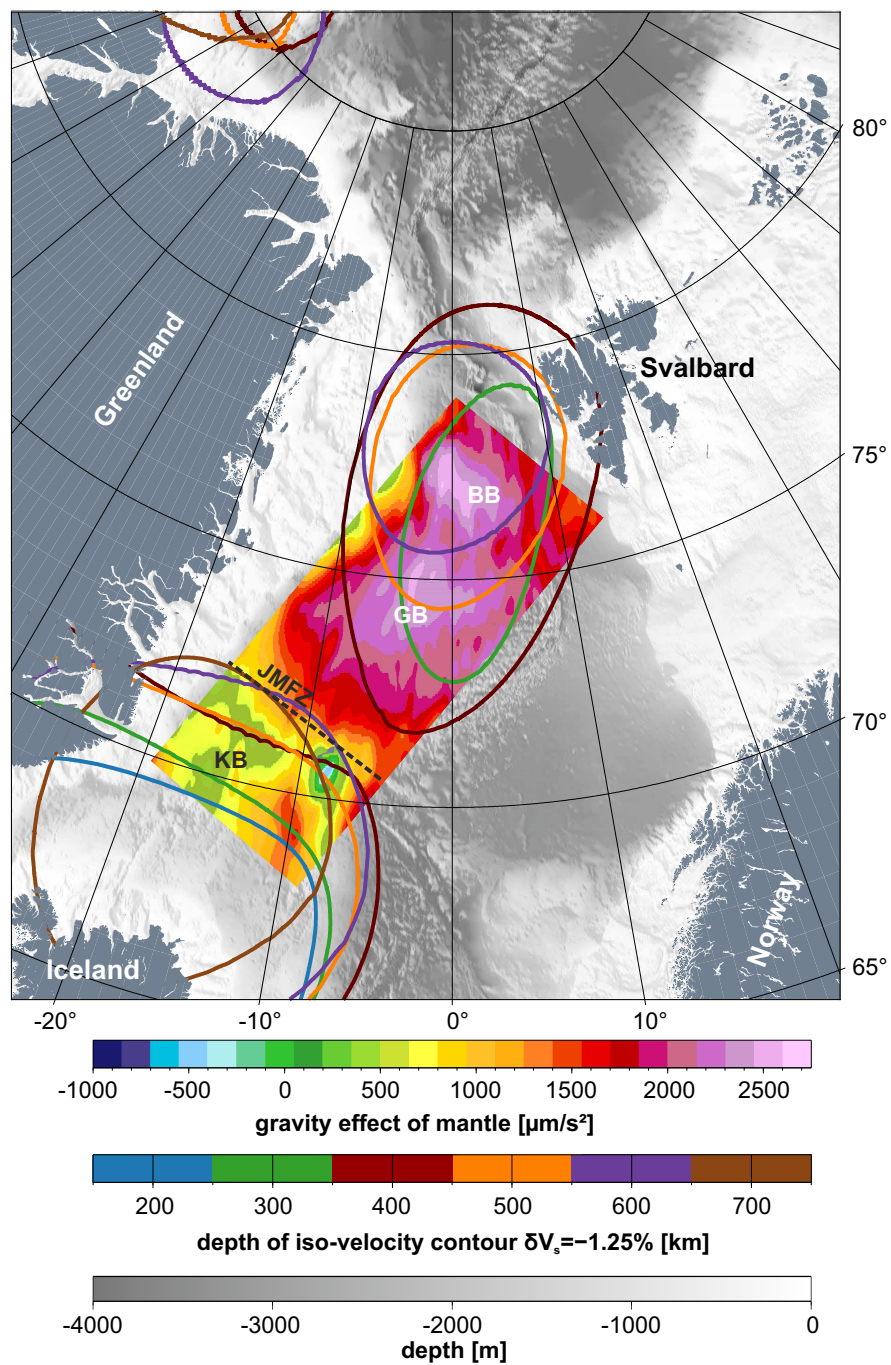


Figure 5.2: Iso-velocity contours based on global S-wave tomography (Ritsema et al. 2011) superimposed on the gravity effect of the upper mantle. The $\delta V_s = -1.25\%$ contour lines run in parallel to the boundaries of the Kolbeinsey Basin (200–700 km depth), especially the Jan Mayen Fracture Zone and the eastern margin of the Jan Mayen Micro-continent.

5.2 An Evolution Model for the East Greenland Margin

In Devonian and Mesozoic times extensive rifting, including significant lithospheric thinning, occurred primarily south of 76°N along the present East Greenland margin (Schlindwein & Jokat 1999, Schlindwein & Jokat 2000). In most tectonic models it is accepted that in Paleocene times, about 62 Ma ago, the supposed Iceland Mantle Plume impinged below (East?) Greenland (Brooks 2011). Simultaneously, a brief period of flood basalts, dyke swarms, and mafic intrusions occurred (Sleep 2006), which is related to massive pre- (62–60 Ma) and breakup (57–55 Ma) flood basalts in East Greenland and West Greenland (Brooks 2011). The following geological evolution, in particular the influence of the supposed Iceland Mantle Plume on the North Atlantic continental breakup, is still under discussion.

In the following paragraphs we present three evolution models and describe necessary modifications based on our new results. Model (1) suggests the formation of thick HVLC below the continental margin and thick oceanic crust without high mantle temperatures (van Wijk et al. 2001, Schmeling 2010). During rifting and continental breakup, shallow melting below the mid-ocean rift valley and deep melting below the continental margin are calculated in a realistic numerical model (Schmeling 2010). Thereby, below the continental margin a larger volume of melt is produced than below the mid-ocean rift valley. Hence, a HVLC as well as a volcanic margin evolved without the existence of a mantle plume or of high mantle temperatures (van Wijk et al. 2001, Schmeling 2010). A HVLC would evolve due to extensive lithospheric thinning during rifting. Model (1) further shows, that the initial plate separation rate is an important parameter for the amount of produced melt at continental margins (Collier et al. 2009, Schmeling 2010). Slow initial plate separation rates of 10 mm/a results in large melt volumes, which produce a thick HVLC below continental margins. In addition to slow initial plate separation rates, moderate higher mantle temperatures are necessary to produce a thick HVLC as observed, for example at the Ethiopian rift (Schmeling 2010). Regarding our results, model (1) would explain the existence

5 Crustal Variations along the Northeast Greenland Margin

of the HVLC below the entire East Greenland margin south of 76°N, including the eastern Jan Mayen Micro-continent margin (66-72°N). However, to the north we could not observe a HVLC. Using the correlation between a thick HVLC below a continental margin and slow initial plate separation rates, the existence of a thick HVLC parallel to the Mohns Ridge and the Aegir Ridge can be explained.

Model (2) is based on active upwelling of the mantle rather than high mantle temperatures (Korenaga et al. 2000, Holbrook et al. 2001). Active upwelling describes rapid vertical movement of material compared with horizontal lithospheric spreading. Passive upwelling describes reduced vertical movement of material compared with rapid horizontal lithospheric spreading. Model (2) suggests, that active upwelling takes place during the initial rifting episode and changes to passive upwelling in the post-rift episode. For the Southeast Greenland margin, normal oceanic crust is produced in distal areas (>500 km away from hotspot) since 45 Ma. Thereby, the influence of the supposed Iceland Mantle Plume is spatially restricted to an area of 400 km in diameter (around hotspot). The surrounding area shows normal mantle temperatures.

Model (3) describes the evolution of thick oceanic crust and a HVLC as the result of passive upwelling and anomalously high mantle temperatures, produced by the supposed Iceland Mantle Plume (White 1988, White & McKenzie 1989). The model assumes a plume head of up to 2000 km in diameter and a increased mantle temperature of 100°C to 200°C. Based on our results, the rifting history is more important than high mantle temperatures for the accretion of thick oceanic crust at the Kolbeinsey Ridge (Chapter 3.3). Hence, the crustal accretion took place following model (2), rather than model (3). This might indicate the minor effect of the supposed Iceland Mantle Plume on the crustal accretion within our research area. We reject model (3), because of the thin oceanic crust which was produced a few million years after the continental breakup along the Mohns Ridge and the Aegir Ridge. At this time, the proposed Iceland Mantle Plume was located below East Greenland and did not influence the crustal accretion along both ridges.

Following our interpretation of the 2009 seismic data, the geological evolution has to be

modified as follows: during rifting and continental breakup, a HVLC and thick oceanic crust evolved due to: (1) extensive lithospheric thinning, (2) slow initial plate separation rates, and (3) slightly higher mantle temperatures (model 1). Around 33 Ma ago, plate reorganisation (Talwani & Eldholm 1977) in combination with the passing of the Iceland Hotspot of the East Greenland margin, resulted in: (1) the Jan Mayen Micro-continent breakup off East Greenland (Gudlaugsson et al. 1988), (2) the formation of the HVLC below Kong Oscar Fjord and the thickening of the HVLC north of the Jan Mayen Fracture Zone, (3) the initiation of spreading along the Kolbeinsey Ridge, and (4) the following extinction of the Aegir Ridge (Gaina et al. 2009). Based on our results, the accretion of thick oceanic crust at the Kolbeinsey Ridge is mainly based on: (1) significant previous extension between the East Greenland margin and the Jan Mayen Micro-continent, and (2) higher mantle temperatures below the Kolbeinsey Basin compared with normal mantle temperatures (Chapter 3.3, Hermann & Jokat 2013b). Hence, the rift history is more important for the Kolbeinsey Basin than the high mantle temperature due to the Iceland Hotspot. Therefore, the Iceland Hotspot has a smaller area of influence on the oceanic crustal accretion than previously thought.

5.3 Comparison with South Atlantic Margin

In general, the evolution of the South Atlantic volcanic margins is closely connected to the Tristan da Cunha Hotspot (e. g. Gladzzenko et al. 1997, O'Connor et al. 2012), which might be explained by a deep mantle plume, rising from the core mantle boundary (e. g. O'Connor et al. 2012). Here, we focus on the Walvis Ridge of the African continental margin, showing: (1) that enhanced melt generation might occur along fracture zones, and (2) that the area of influence of hotspots on crustal accretion is concentrated on a small area.

The Walvis Ridge originated as hotspot track of the Tristan da Cunha Hotspot (O'Connor & Duncan 1990) and is bounded by a major transform fault to the north (Fromm et al. 2013). Along the ridge, recent magmatic activity, unrelated to the Tristan da Cunha

5 Crustal Variations along the Northeast Greenland Margin

Hotspot, is observed (Haxel & Dziak 2005, Elliott et al. 2009). Regarding our model of enhanced melt generation along fracture zones, it is suggested that the recent magmatic activity is explained by accumulated melt along the fracture zone (Jokat et al. 2012b). Hence, the fracture zone acted as magmatic pathway for melts similar to the Jan Mayen Fracture Zone.

Regarding the area of influence of hotspots on crustal accretion, the Walvis Ridge has a maximum width of 360 km and is bounded by normal oceanic crust (7 km thick) on both sides (Fromm et al. 2013). This value might be similar to suggested values for the Iceland Hotspot and indicates the reduced influence on crustal accretion.

6 Conclusion and Discussion

The main research area during the ARK-XXIV/3 summer expedition of the RV Polarstern in 2009 was the continental margin of Northeast Greenland. Focus of the expedition was the acquisition of new information about the tectonic history and the crustal variations along the margin. For these purposes, different datasets – including two seismic refraction lines and parallel onboard gravity measurements – were recorded. The first seismic refraction line is located in the Boreas Basin and runs from the ultraslow spreading Knipovich Ridge to the Northeast Greenland margin. The second seismic refraction line starts in the Kong Oscar Fjord and crosses the Kolbeinsey Ridge. In addition to the recorded gravity data, public-domain gravity data from the ArcGP are available within the research area.

Summarising our results, both seismic refraction lines provide detailed new facts about the crustal and upper mantle structures below the Boreas Basin, the Knipovich Ridge, Kong Oscar Fjord, and the Kolbeinsey Ridge as follows: (1) thin oceanic crust below the Boreas Basin and the Knipovich Ridge, (2) no significant oceanic layer 3 within the Boreas Basin, (3) small-scale segmentation along the Knipovich Ridge, (4) thick oceanic crust below the Kolbeinsey Ridge, and (5) a HVLC below Kong Oscar Fjord. Based on the gravity data, two 2.5D gravity models were calculated to verify the seismic models by an independent geophysical method. Both models confirmed the seismic models and were used as boundary conditions for a 3D gravity model. The 3D gravity model represents a consistent crustal and upper mantle model along the Northeast Greenland margin including our results as well as further published information. Hence, the 3D gravity model showed that: (1) the oceanic crustal thickness changed significantly across the narrow Jan Mayen Fracture Zone, and (2) the upper mantle densities below the Kolbeinsey Basin are significant lower than below the Greenland Basin and the Boreas Basin. Using all information, we could give some new statements for the evolution model of the Northeast Greenland continental margin and the crustal accretion within the research area. Most important new statements based on our results

are: (1) the structure of oceanic crust (crustal thickness, absence of oceanic layer 3) along the ultraslow spreading Knipovich Ridge is more heterogeneous than previously thought, (2) for the accretion of thick oceanic crust at the Kolbeinsey Ridge, the rift history of Northeast Greenland (extensive thinning before continental breakup) is more important than high mantle temperatures, and (3) the Iceland Hotspot has a smaller area of influence on the oceanic crustal accretion than previously thought.

The following discussion focuses on the key statements concerning our results from the Northeast Greenland margin.

Does hyper-extended continental crust exist within the Boreas Basin?

The ambiguous and weak magnetic spreading anomalies as well as non-reversed seismic refraction results (Døssing et al. 2008) lead to the conclusion of hyper-extended continental crust within the Boreas Basin. However, our results of seismic refraction line 20090200 show that the crust within the Boreas Basin is of oceanic origin. This conclusion based on the consistent crustal structures along our seismic refraction line from the active spreading Knipovich Ridge towards the Northeast Greenland margin. Furthermore, the rough basement topography and the 3 km thin crust, typical for oceanic crust along ultraslow spreading ridges, speak for an oceanic crust. Therefore, we conclude that the postulated hyper-extended continental crust within the Boreas Basin has to be changed into a thin oceanic crust.

Does the ultraslow spreading Knipovich Ridge produce thin oceanic crust without oceanic layer 3?

The Knipovich Ridge has a full spreading rate of 14.6 mm/a, and therefore, it can be classified as ultraslow spreading ridge (Dick et al. 2003). Compared with other ultraslow spreading ridges (e. g. Gakkel Ridge; Jokat et al. 2003, Jokat & Schmidt-Aursch 2007) the Knipovich Ridge produces also no oceanic layer 3, based on our seismic refraction line 20090200 (crustal thickness of 3 km, crustal velocities <6.3 km/s). However, seismic refraction lines east of the Knipovich Ridge show a thin oceanic

layer 3 with crustal velocities above 6.3 km/s (Ljones et al. 2004, Kandilarov et al. 2008, 2010). These seismic refraction lines are located within magmatic segments, which are characterised by centres of high magmatic productivity. Therefore, a thick oceanic crust including an oceanic layer 3 is formed. The melt delivered from the magmatic segments to the magmatically starved, amagmatic segments by lateral dyke propagation. The amagmatic segments are characterised by thin oceanic crust. This leads to the conclusion that the crustal structure, including segmentation, along the ultraslow spreading Knipovich Ridge is more heterogeneous than previously thought based on former seismic refraction results. Along the Knipovich Ridge an oceanic layer 3 is produced within magmatic segments and within amagmatic segments no oceanic layer 3 exists.

Does the HVLC below Kong Oscar Fjord extends below the oceanic crust?

The older published seismic refraction line 94340 within Kong Oscar Fjord shows a HVLC below the continental crust (Schlindwein & Jokat 1999). However, the seaward extension of the HVLC could not be verified because the seismic refraction line 94340 does not cross the continent-ocean boundary. Our seismic refraction line 20090100 crosses the proposed continent-ocean boundary and shows a 3 km thick HVLC with seismic P-wave velocities between 7.0 km/s and 7.4 km/s. Therefore, the HVLC evolved during the separation of the Jan Mayen Micro-continent off East Greenland, and not during the Early Eocene breakup of the northern North Atlantic, due to the extension of the HVLC below the oceanic crust. In addition, we suggest a large melt production along the Jan Mayen Fracture Zone which caused the HVLC below Kong Oscar Fjord.

Is the accretion of thick oceanic crust at the Kolbeinsey Ridge only caused by high mantle temperatures?

At the Kolbeinsey Ridge thick oceanic crust of approximately 9 km exists. In general, normal oceanic crust has a thickness of 7 km (White et al. 1992, Juteau & Maury 1999). Furthermore, a thick oceanic crust relates to high mantle temperatures (White

6 Conclusion and Discussion

& McKenzie 1989, Kodaira et al. 1998b), which could be caused by the proposed Iceland Mantle Plume. However, these interpretations neglected the rift history of the Kolbeinsey Basin when explaining the accretion of thick oceanic crust. Following our interpretation of the Jan Mayen Ridge (eastern part of the Jan Mayen Micro-continent) as an outer basement high of the East Greenland margin, extensive lithospheric thinning occurred before the continental breakup of the Jan Mayen Micro-continent off East Greenland. In addition to the extensive lithospheric thinning, subsequent high mantle temperatures resulted in accretion of thick oceanic crust (Armitage et al. 2009, 2010). Hence, the rift history is more important for the accretion of thick oceanic crust at the Kolbeinsey Ridge than high mantle temperatures. In addition, our model explains the crustal thinning to the north across the narrow Jan Mayen Fracture Zone.

Does a simple Iceland Hotspot model explain the crustal variations along the Northeast Greenland margin?

Along the Northeast Greenland margin significant crustal variations are observable. The crustal variations – thick and thin oceanic crust, existence and non-existence of a HVLC – indicate that the Northeast Greenland margin is more heterogeneous compared with the Southeast Greenland margin. Regarding the HVLC on both sides of the Jan Mayen Fracture Zone, the evolution is difficult to explain by a simple model of the Iceland Hotspot. Furthermore, the Iceland Hotspot has a minor area of influence than previously thought, based on: (1) our model of melt generation along the Jan Mayen Fracture Zone for the formation of the HVLC below Kong Oscar Fjord, and (2) the greater importance of the rift history (extensive lithospheric thinning before continental breakup) compared with high mantle temperatures for the crustal accretion in the Kolbeinsey Basin.

7 Outlook

This thesis includes the interpretation of: (1) seismic refraction models along two lines, (2) 2.5D gravity models along both seismic refraction lines, and (3) a 3D gravity model of the Northeast Greenland margin. Based on our results, many questions remain open and offering potential for further investigations.

Within local scale, some crustal structures in the Boreas Basin and offshore Kong Oscar Fjord are still unknown. Therefore, the seismic refraction line 20090200 should be extended onto the Northeast Greenland Shelf (Fig. 7.1), to seismically determine the continent-ocean boundary as well as the crustal thickness of the continental crust. Hence, our suggested non-volcanic margin can be proved. Furthermore, two seismic refraction lines across the Jan Mayen Fracture Zone are suggested and displayed in Figure 7.1. Hence, the variation of the HVLC across the fracture zone and our model of enhanced melt generation along the fracture zone can be proved.

At regional scale, the crustal and sedimentary thicknesses of the Northeast Greenland Shelf are less well known. Therefore, our 3D gravity model should be extended onto the Northeast Greenland Shelf (Fig. 7.1). Based on our 3D gravity model, a thermal model using measured heat flow data from the 2009 summer expedition provides new information about the mantle structures. In addition, the proposed higher mantle temperatures below the Kolbeinsey Basin can be tested which will give more new ideas about crustal accretion and the structure of the Iceland Hotspot.

At global scale, the area of influence of the Iceland Hotspot is still unknown. Therefore, a numerical geodynamic model of the Iceland Hotspot and northern North Atlantic, including the local plate tectonic situation, should be developed. Hence, the area of influence of the Iceland Hotspot can be estimated, using the observed heat flow data, reconstructed uplift values of the lithosphere, and observed isostatic anomalies. The results might give new information for the reconstruction of the opening of the northern North Atlantic, which represents the only deep-water connection into the Arctic Ocean and, therefore, is important for the global Thermohaline Circulation.

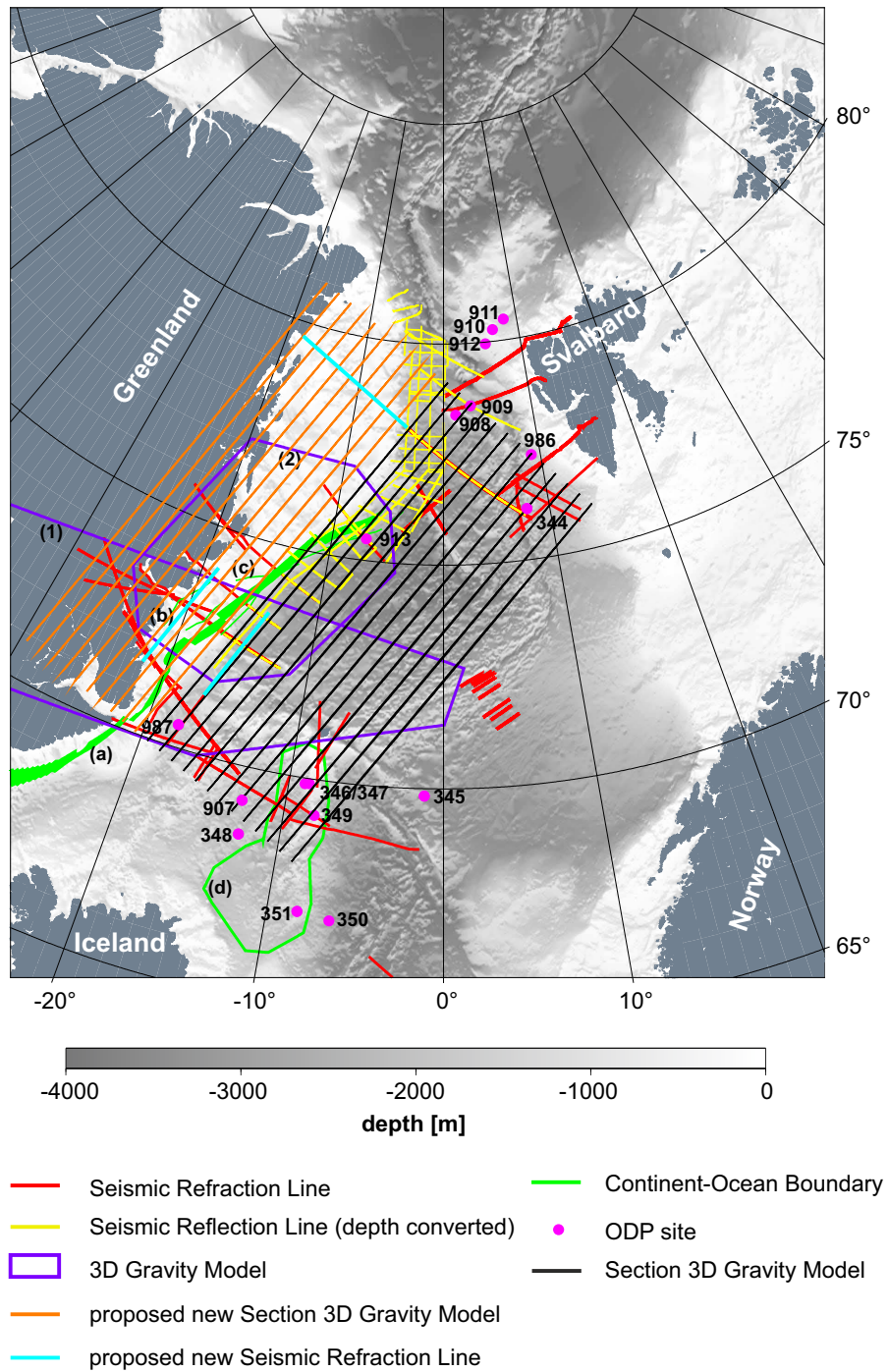


Figure 7.1: Proposed new seismic refraction lines and new sections for the 3D gravity model. References for the shown data see Figure 2.2 and Table 4.1. The black lines show the 13 sections of our 3D gravity model.

8 References

- Armitage, J. J., Henstock, T. J., Minshull, T. A. & Hopper, J. R. Lithospheric controls on melt production during continental breakup at slow rates of extension: Application to the North Atlantic. *Geochemistry, Geophysics, Geosystems* **10**, pp. 20 (2009), doi:10.1029/2009gc002404.
- Armitage, J. J., Collier, J. S. & Minshull, T. A. The importance of rift history for volcanic margin formation. *Nature* **465**, 913–917 (2010), doi:10.1038/nature09063.
- Behn, M. D., Boettcher, M. S. & Hirth, G. Thermal structure of oceanic transform faults. *Geology* **35**, 307–310 (2007), doi:10.1130/g23112a.1.
- Berger, D. & Jokat, W. A seismic study along the East Greenland margin from 72°N to 77°N. *Geophysical Journal International* **174**, 733–748 (2008), doi:10.1111/j.1365-246X.2008.03794.x.
- Berger, D. & Jokat, W. Sediment deposition in the northern basins of the North Atlantic and characteristic variations in shelf sedimentation along the East Greenland margin. *Marine and Petroleum Geology* **26**, 1321–1337 (2009), doi:10.1016/marpetgeo.2009.04.005.
- BGGS – Bodensee Gravimeter Geosystem GmbH. *Marine Gravity Meter KSS 32-M, Instruction Manual, Vol. 2, Hardware*. pp. 50 (2011), Bodensee Gravimeter Geosystem GmbH, Überlingen.
- Blakely, R. J. *Potential Theory in Gravity & Magnetic Applications*. pp. 441 (1995), Cambridge University Press, Cambridge, ISBN:052141508X.
- Boebel, T. Flugzeuggestützte Topographie- und Schweremessung: Meßsystem und Anwendung auf die Region Framstraße, Spitsbergen und Nordostgrönland=Airborne topography and gravimetry: system and application to Fram Strait, Svalbard and northeast Greenland. *Berichte zur Polar- und Meeresforschung (Reports on Polar*

8 References

- and Marine Research*) **366**, pp. 129 (2000), Alfred Wegener Institute for Polar and Marine Research, Bremerhaven, hdl:10013/epic.10370.d001.
- Bown, J. W. & White, R. S. Variation with spreading rate of oceanic crustal thickness and geochemistry. *Earth and Planetary Science Letters* **121**, 435–449 (1994), doi:10.1016/0012-821X(94)90082-5.
- Breivik, A. J., Verhoef, J. & Faleide, J. I. Effect of thermal contrasts on gravity modeling at passive margins: Results from the western Barents Sea. *Journal of Geophysical Research* **104**, 15293–15311 (1999), doi:10.1029/1998jb900022.
- Breivik, A. J., Mjelde, R., Faleide, J. I. & Murai, Y. Rates of continental breakup magmatism and seafloor spreading in the Norway Basin–Iceland plume interaction. *Journal of Geophysical Research* **111**, pp. 17 (2006), doi:10.1029/2005jb004004.
- Breivik, A. J., Mjelde, R., Faleide, J. I. & Murai, Y. The eastern Jan Mayen microcontinent volcanic margin. *Geophysical Journal International* **188**, 798–818 (2012), doi:10.1111/j.1365-246X.2011.05307.x.
- Brooks, C. K. The East Greenland rifted volcanic margin. *Geological Survey of Denmark and Greenland Bulletin* **24**, pp. 96 (2011), ISBN:9788778713223.
- Brozena, J. M., Peters, M. F. & Salman, R. Arctic airborne gravity measurement program. In *Gravity, Geoid and Marine Geodesy, International Association of Geodesy Symposia Vol. 117* (eds Segawa, J., Fujimoto, H. & Okubo, S.), 131–139 (1997), Springer, New York, ISBN:9783540633525.
- Burke, K. & Torsvik, T. H. Derivation of Large Igneous Provinces of the past 200 million years from long-term heterogeneities in the deep mantle. *Earth and Planetary Science Letters* **227**, 531–538 (2004), doi:10.1016/j.epsl.2004.09.015.
- Burke, K., Steinberger, B., Torsvik, T. H. & Smethurst, M. A. Plume Generation Zones at the margins of Large Low Shear Velocity Provinces on the

- core–mantle boundary. *Earth and Planetary Science Letters* **265**, 49–60 (2008), doi:10.1016/j.epsl.2007.09.042.
- Carlson, R. L. & Raskin, G. S. Density of the ocean crust. *Nature* **311**, 555–558 (1984), doi:10.1038/311555a0.
- Christensen, N. I. Compressional Wave Velocities in Rocks at High Temperatures and Pressures, Critical Thermal Gradients, and Crustal Low-Velocity Zones. *Journal of Geophysical Research* **84**, 6849–6857 (1979), doi:10.1029/JB084iB12p06849.
- Christensen, N. I. & Mooney, W. D. Seismic velocity structure and composition of the continental crust: A global view. *Journal of Geophysical Research* **100**, 9761–9788 (1995), doi:10.1029/95JB00259.
- Christensen, N. I. Poisson’s ratio and crustal seismology. *Journal of Geophysical Research* **101**, 3139–3156 (1996), doi:10.1029/95JB03446.
- Christensen, N. I. Serpentinities, Peridotites, and Seismology. *International Geology Review* **46**, 795–816 (2004), doi:10.2747/0020-6814.46.9.795.
- Collier, J. S., Minshull, T. A., Hammond, J. O. S., Whitmarsh, R. B., Kendall, J.-M., Sansom, V., Lane, C. I. & Rumpker, G. Factors influencing magmatism during continental breakup: New insights from a wide-angle seismic experiment across the conjugate Seychelles-Indian margins. *Journal of Geophysical Research* **114**, pp. 25 (2009), doi:10.1029/2008JB005898.
- Czuba, W., Ritzmann, O., Nishimura, Y., Grad, M., Mjelde, R., Guterch, A. & Jokat, W. Crustal structure of northern Spitsbergen along the deep seismic transect between the Molloy Deep and Nordaustlandet. *Geophysical Journal International* **161**, 347–364 (2005), doi:10.1111/j.1365-246X.2005.02593.x.
- DeMets, C., Gordon, R. G., Argus, D. F. & Stein, S. Current plate motions. *Geophysical Journal International* **101**, 425–478 (1990), doi:10.1111/j.1365-246X.1990.tb06579.x.

8 References

- Dick, H. J. B., Lin, J. & Schouten, H. An ultraslow-spreading class of ocean ridge. *Nature* **426**, 405–412 (2003), doi:10.1038/nature02128.
- Domenico, S. N. Rock lithology and porosity determination from shear and compressional wave velocity. *Geophysics* **49**, 1188–1195 (1984), doi:10.1190/1.1441748.
- Døssing, A., Dahl-Jensen, T., Thybo, H., Mjelde, R. & Nishimura, Y. East Greenland Ridge in the North Atlantic Ocean: An integrated geophysical study of a continental sliver in a boundary transform fault setting. *Journal of Geophysical Research* **113**, pp. 33 (2008), doi:10.1029/2007/JB005536.
- Edwards, M. H. & Coakley, B. J. SCICEX Investigations of the Arctic Ocean System. *Chemie der Erde – Geochemistry* **63**, 281–328 (2003), doi:10.1078/0009-2819-00039.
- Ehlers, B. M. & Jokat, W. Subsidence and crustal roughness of ultra-slow spreading ridges in the northern North Atlantic and the Arctic Ocean. *Geophysical Journal International* **177**, 451–462 (2009), doi:10.1111/j.1365-246X.2009.04078.x.
- Eldholm, O., Skogseid, J., Sundvor, E. & Myhre, A. The Norwegian-Greenland Sea. In *The Arctic Ocean Region, The Geology of North America, Vol. L* (eds Grantz, A., Johnson, L. & Sweeney, J. F.), 351–364 (1990), The Geological Society of America, Boulder/Colorado, ISBN:0813752116.
- Elliott, G. M., Berndt, C. & Parson, L. M. The SW African volcanic rifted margin and the initiation of the Walvis Ridge, South Atlantic. *Marine Geophysical Researches* **30**, 207–214 (2009), doi:10.1007/s11001-009-9077-x.
- Engen, Ø., Frazer, L. N., Wessel, P. & Faleide, J. I. Prediction of sediment thickness in the Norwegian-Greenland Sea from gravity inversion. *Journal of Geophysical Research* **111**, pp. 18 (2006), doi:10.1029/2005jb003924.
- Engen, Ø., Faleide, J. I. & Dyreng, T. K. Opening of the Fram Strait gateway: A review of plate tectonic constraints. *Tectonophysics* **450**, 51–69 (2008), doi:10.1016/j.tecto.2008.01.002.

- Escher, J. C. & Pulvertaft, T. C. R. *Geological map of Greenland, 1:2 500 000*. pp. 93 (1995), Geological Survey of Greenland, Copenhagen, ISBN:8778710693.
- Faleide, J. I., Vågnes, E. & Gudlaugsson, S. T. Late Mesozoic–Cenozoic evolution of the south-western Barents Sea in a regional rift–shear tectonic setting. *Marine and Petroleum Geology* **10**, 186–214 (1993), doi:10.1016/0264-8172(93)90104-Z.
- Forsberg, R. & Kenyon, S. Arctic Gravity Project. In *Program and Abstracts of the 27th Annual Scientific Meeting of the Canadian Geophysical Union* (ed Pagiatakis, S.), pp. 4 (2001), Ottawa, Canada, URL:<http://earth-info.nga.mil/GandG/wgs84/agp/abstract.doc>.
- Forsberg, R., Olesen, A. V. & Keller, K. Airborne gravity survey of the North Greenland continental shelf. In *Gravity, Geoid and Geodynamics 2000, International Association of Geodesy Symposia* **123** (ed Sideris, M. G.), 235–240 (2002), Springer, New York, ISBN:9783540424697.
- Forsberg, R. & Kenyon, S. Gravity and Geoid in the Arctic Region – The Northern Polar Gap now Filled. In *GOCE, The Geoid and Oceanography, Proceedings of the Second International GOCE User Workshop, ESA SP-569* (ed Lacoste, H.), pp. 5 (2004), ESA Publication Division, Netherlands, ISBN:9290928808.
- Forsberg, R. & Skourup, H. Arctic Ocean gravity, geoid and sea-ice freeboard heights from ICESat and GRACE. *Geophysical Research Letters* **32**, pp. 4 (2005), doi:10.1029/2005GL023711.
- Foulger, G. R. & Anderson, D. L. A cool model for the Iceland hotspot. *Journal of Volcanology and Geothermal Research* **141**, 1–22 (2005), doi:10.1016/j.jvolgeores.2004.10.007.
- Fromm, T., Jokat, W., Behrmann, J. H., Ryberg, T. & Weber, M. Deep crustal structure of the Walvis Ridge at the junction with the Namibian coast. In

8 References

- SAMPLE Colloquium (11 June–14 June 2013, Talk)* (2013), Heidelberg/Germany, hdl:10013/epic.41683.
- Funck, T., Hopper, J. R., Larsen, H. C., Louden, K. E., Tucholke, B. E. & Holbrook, W. S. Crustal structure of the ocean-continent transition at Flemish Cap: Seismic refraction results. *Journal of Geophysical Research* **108**, pp. 20 (2003), doi:10.1029/2003JB002434.
- Gaina, C., Gernigon, L. & Ball, P. Palaeocene Recent plate boundaries in the NE Atlantic and the formation of the Jan Mayen microcontinent. *Journal of the Geological Society London* **166**, 601–616 (2009), doi:10.1144/0016-76492008-112.
- Geoffroy, L. Volcanic passive margins. *Comptes Rendus Geoscience* **337**, 1395–1408 (2005), doi:10.1016/j.crte.2005.10.006.
- Gernigon, L., Olesen, O., Ebbing, J., Wienecke, S., Gaina, C., Mogaard, J. O., Sand, M. & Myklebust, R. Geophysical insights and early spreading history in the vicinity of the Jan Mayen Fracture Zone, Norwegian–Greenland Sea. *Tectonophysics* **468**, 185–205 (2009), doi:10.1016/j.tecto.2008.04.025.
- Gladchenko, T. P., Hinz, K., Eldholm, O., Meyer, H., Neben, S. & Skogseid, J. South Atlantic volcanic margins. *Journal of the Geological Society, London* **154**, 465–470 (1997), doi:10.1144/gsjgs.154.3.0465.
- Götze, H.-J. & Lahmeyer, B. Application of three-dimensional interactive modeling in gravity and magnetics. *Geophysics* **53**, 1096–1108 (1988), doi:10.1190/1.1442546.
- Gradstein, F. M., Ogg, J. G., Schmitz, M. & Ogg, G. *The geologic time scale 2012*. pp. 1176 (2012), Elsevier, Amsterdam, ISBN:9780444594259.
- Greenhalgh, E. E. & Kuszniir, N. J. Evidence for thin oceanic crust on the extinct Aegir Ridge, Norwegian Basin, NE Atlantic derived from satellite gravity inversion. *Geophysical Research Letters* **34**, pp. 5 (2007), doi:10.1029/2007GL029440.

- Grevemeyer, I. & Weigel, W. Seismic velocities of the uppermost igneous crust versus age. *Geophysical Journal International* **124**, 631–635 (1996), doi:10.1111/j.1365-246X.1996.tb07041.x.
- Gudlaugsson, S. T., Gunnarsson, K., Sand, M. & Skogseid, J. Tectonic and volcanic events at the Jan Mayen Ridge microcontinent. *Geological Society, London, Special Publications* **39**, 85–93 (1988), doi:10.1144/GSL.SP.1988.039.01.09.
- Hall, S. A., Casey, J. F. & Elthon, D. L. A possible explanation of gravity anomalies over mid-ocean ridges. *Journal of Geophysical Research* **91**, 3724–3738 (1986), doi:10.1029/JB091iB03p03724.
- Haller, J. The East Greenland Caledonides – reviewed. In *The Caledonide Orogen – Scandinavia and Related Areas* (eds Gee, D. S. & Sturt, B. A.), 1031–1046 (1985), John Wiley & Sons Ltd, London, ISBN:9780471105046.
- Haxel, J. H. & Dziak, R. P. Evidence of explosive seafloor volcanic activity from the Walvis Ridge, South Atlantic Ocean. *Geophysical Research Letters* **32**, pp. 4 (2005), doi:10.1029/2005GL023205.
- Hegewald, A. The Chukchi Region - Arctic Ocean - Tectonic and Sedimentary Evolution. *PhD Thesis*, pp. 108 (2012), Friedrich Schiller University Jena.
- Henriksen, N., Higgins, A. K., Kalsbeek, F. & Pulvertaft, T.C.R. Greenland from Archaean to Quaternary. Descriptive text to the 1995 Geological map of Greenland, 1:2 500 000. 2nd edition. *Geological Survey of Denmark and Greenland Bulletin* **18**, pp. 126 (2009).
- Hermann, T. & Jokat, W. Crustal structures of the Boreas Basin and the Knipovich Ridge, North Atlantic. *Geophysical Journal International* **193**, 1399–1414 (2013a), doi:10.1093/gji/ggt048.
- Hermann, T. & Jokat, W. An evolution model for the high-velocity lower crust beneath Kong Oscar Fjord, East Greenland. (2013b, submitted)

8 References

- Hooft, E. E. E., Brandsdóttir, B., Mjelde, R., Shimamura, H. & Murai, Y. Asymmetric plume-ridge interaction around Iceland: The Kolbeinsey Ridge Iceland Seismic Experiment. *Geochemistry, Geophysics, Geosystems* **7**, pp. 26 (2006), doi:10.1029/2005gc001123.
- Holbrook, W. S., Mooney, W. D. & Christensen, N. J. The seismic velocity structure of the deep continental crust. In *Continental lower crust 1* (eds Fountain, D., Arculus, R. & Kay, R. W.), 451–464 (1992), Elsevier, Amsterdam, ISBN:0444882944.
- Holbrook, W. S., Larsen, H. C., Korenaga, J., Dahl-Jensen, T., Reid, I. D., Kelemen, P. B., Hopper, J. R., Kent, G. M., Lizarralde, D., Bernstein, S. & Detrick, R. S. Mantle thermal structure and active upwelling during continental breakup in the North Atlantic. *Earth and Planetary Science Letters* **190**, 251–266 (2001), doi:10.1016/S0012-821X(01)00392-2.
- Horen, H., Zamora, M. & Dubuisson, G. Seismic waves velocities and anisotropy in serpentinized peridotites from Xigaze ophiolite: Abundance of serpentine in slow spreading ridge. *Geophysical Research Letters* **23**, 9–12 (1996), doi:10.1029/95GL03594.
- Huang, J., Zhong, S. & van Hunen, J. Controls on sublithospheric small-scale convection. *Journal of Geophysical Research* **108**, pp. 13 (2003), doi:10.1029/2003jb002456.
- Jakobsson, M., Macnab, R., Mayer, L., Anderson, R., Edwards, M., Hatzky, J., Schenke, H. W. & Johnson, P. An improved bathymetric portrayal of the Arctic Ocean: Implications for ocean modeling and geological, geophysical and oceanographic analyses. *Geophysical Research Letters* **35**, pp. 5 (2008a), doi:10.1029/2008GL033520.
- Jakobsson, M., Mayer, L., Coakley, B., Dowdeswell, J. A., Forbes, S., Fridman, B., Hodnesdal, H., Noormets, R., Pedersen, R., Rebesco, M., Schenke, H. W., Zarayskaya, Y., Accettella, D., Armstrong, A., Anderson, R. M., Bienhoff, P., Camerlenghi, A., Church, I., Edwards, M., Gardner, J. V., Hall, J. K., Hell, B., Hestvik, O., Kristoffersen, Y., Marcussen, C., Mohammad, R., Mosher, D., Nghiem, S. V., Pedrosa, M.

-
- T., Travaglini, P. G. & Weatherall, P. The International Bathymetric Chart of the Arctic Ocean (IBCAO) Version 3.0. *Geophysical Research Letters* **39**, pp. 6 (2012), doi:10.1029/2012gl052219.
- Jansen, E., Raymo, M. E., Blum, P., Andersen, E. S., Austin, W. E. N., Baumann, K.-H., Bout-Roumazelles, V., Carter, S. J., Channell, J. E. T., Cullen, J. L., Flower, B., Higgins, S., Hodell, D. A., Hood, J. A., Hyun, S. M., Ikehara, M., King, T., Larter, R., Lehman, B., Locker, S., McIntyre, K., McManus, R., Meng, L. B., O'Connell, S., Ortiz, J. D., Rack, F. R., Solheim, A. & Wei, W. Site 907 (Revisited). In *Proceedings of the Ocean Drilling Program, Initial Reports* **162** (eds Blum, P.), 223–252 (1996a), College Station, Texas, doi:10.2973/odp.proc.ir.162.107.1996.
- Jansen, E., Raymo, M. E., Blum, P., Andersen, E. S., Austin, W. E. N., Baumann, K.-H., Bout-Roumazelles, V., Carter, S. J., Channell, J. E. T., Cullen, J. L., Flower, B., Higgins, S., Hodell, D. A., Hood, J. A., Hyun, S. M., Ikehara, M., King, T., Larter, R., Lehman, B., Locker, S., McIntyre, K., McManus, R., Meng, L. B., O'Connell, S., Ortiz, J. D., Rack, F. R., Solheim, A. & Wei, W. Site 985. In *Proceedings of the Ocean Drilling Program, Initial Reports* **162** (eds Blum, P.), 253–285 (1996b), College Station, Texas, doi:10.2973/odp.proc.ir.162.108.1996.
- Jansen, E., Raymo, M. E., Blum, P., Andersen, E. S., Austin, W. E. N., Baumann, K.-H., Bout-Roumazelles, V., Carter, S. J., Channell, J. E. T., Cullen, J. L., Flower, B., Higgins, S., Hodell, D. A., Hood, J. A., Hyun, S. M., Ikehara, M., King, T., Larter, R., Lehman, B., Locker, S., McIntyre, K., McManus, R., Meng, L. B., O'Connell, S., Ortiz, J. D., Rack, F. R., Solheim, A. & Wei, W. Site 986. In *Proceedings of the Ocean Drilling Program, Initial Reports* **162** (eds Blum, P.), 287–343 (1996c), College Station, Texas, doi:10.2973/odp.proc.ir.162.109.1996.
- Jansen, E., Raymo, M. E., Blum, P., Andersen, E. S., Austin, W. E. N., Baumann, K.-H., Bout-Roumazelles, V., Carter, S. J., Channell, J. E. T., Cullen, J. L., Flower, B., Higgins, S., Hodell, D. A., Hood, J. A., Hyun, S. M., Ikehara, M., King, T., Larter,

8 References

- R., Lehman, B., Locker, S., McIntyre, K., McManus, R., Meng, L. B., O'Connell, S., Ortiz, J. D., Rack, F. R., Solheim, A. & Wei, W. Site 987. In *Proceedings of the Ocean Drilling Program, Initial Reports* **162** (eds Blum, P.), 345–387 (1996d), College Station, Texas, doi:10.2973/odp.proc.ir.162.110.1996.
- Jokat, W., Ritzmann, O., Schmidt-Aursch, M. C., Drachev, S., Gauger, S. & Snow, J. Geophysical evidence for reduced melt production on the Arctic ultraslow Gakkel mid-ocean ridge. *Nature* **423**, 962–965 (2003), doi:10.1038/nature01706.
- Jokat, W. & Schmidt-Aursch, M. C. Geophysical characteristics of the ultraslow spreading Gakkel Ridge, Arctic Ocean. *Geophysical Journal International* **168**, 983–998 (2007), doi:10.1111/j.1365-246X.2006.03278.x.
- Jokat, W., Abramova, A., Beckert, U., Busche, C., Damaske, D., Feld, C., Geissler, W., Gossler, J., Hegewald, A., Jensen, L., Kollofrath, J., L"aderach, C., Lehmann, P., Leinweber, V., Martens, H., Penshorn, D., Prokoph, A., Sommer, M., Winkelmann, D. & Winter, F. Marine Geophysics. In *The Expedition of the Research Vessel "Polarstern" to the Arctic in 2009 (ARK-XXIV/3), Berichte zur Polar- und Meeresforschung (Reports on Polar and Marine Research)* **615** (eds Jokat, W. & the participants), 13–70 (2010), Alfred Wegener Institute for Polar and Marine Research, Bremerhaven, hdl:10013/epic.35320.d001.
- Jokat, W., Kollofrath, J., Geissler, W. H. & Jensen, L. Crustal thickness and earthquake distribution south of the Logachev Seamount, Knipovich Ridge. *Geophysical Research Letters* **39**, pp. 6 (2012a), doi:10.1029/2012gl051199.
- Jokat, W., Planert, L., Fromm, T., Ryberg, T., Weber, M. & Behrmann, J. Evolution of the South Atlantic: Consequences for the Walvis Ridge/Rio Grande Rise (hot spot?) volcanism. In *46th Brazilian Geological Congress (30 September–5 October 2012, Talk)* (2012b), Santos/Brazil, hdl:10013/epic.39836.
- Juteau, T. & Maury. *The Oceanic Crust, from Accretion to Mantle Recycling*. **1**, pp. 390 (1999), Springer, London, ISBN:185233116X.

-
- Kandilarov, A., Mjelde, R., Okino, K. & Murai, Y. Crustal structure of the ultra-slow spreading Knipovich Ridge, North Atlantic, along a presumed amagmatic portion of oceanic crustal formation. *Marine Geophysical Researches* **29**, 109–134 (2008), doi:10.1007/s11001-008-9050-0.
- Kandilarov, A., Landa, H., Mjelde, R., Pedersen, R. B., Okino, K. & Murai, Y. Crustal structure of the ultra-slow spreading Knipovich Ridge, North Atlantic, along a presumed ridge segment center. *Marine Geophysical Researches* **31**, 173–195 (2010), doi:10.1007/s11001-010-9095-8.
- Kandilarov, A., Mjelde, R., Pedersen, R. B., Hellevang, B., Papenberg, C., Petersen, C. J., Planert, L. & Flueh, E. The northern boundary of the Jan Mayen microcontinent, North Atlantic determined from ocean bottom seismic, multichannel seismic, and gravity data. *Marine Geophysical Researches* **33**, 55–76 (2012), doi:10.1007/S11001-012-9146-4.
- Kenyon, S., Forsberg, R. & Coakley, B. New Gravity Field for the Arctic. *EOS Transactions American Geophysical Union* **89**, 289–290 (2008), doi:10.1029/2008EO320002.
- Klingelhöfer, F., Géli, L., Matias, L., Steinsland, N. & Mohr, J. Crustal structure of a super-slow spreading centre: a seismic refraction study of Mohns Ridge, 72°N. *Geophysical Journal International* **141**, 509–526 (2000), doi:10.1046/j.1365-246x.2000.00098.x.
- Kodaira, S., Mjelde, R., Gunnarsson, K., Shiobara, H. & Shimamura, H. Crustal structure of the Kolbeinsey Ridge, North Atlantic, obtained by use of ocean bottom seismographs. *Journal of Geophysical Research* **102**, 3131–3151 (1997), doi:10.1029/96jb03487.
- Kodaira, S., Mjelde, R., Gunnarsson, K., Shiobara, H. & Shimamura, H. Structure of the Jan Mayen microcontinent and implications for its evolution. *Geophysical Journal International* **132**, 383–400 (1998a), doi:10.1046/j.1365-246x.1998.00444.x.

8 References

- Kodaira, S., Mjelde, R., Gunnarsson, K., Shiobara, H. & Shimamura, H. Evolution of oceanic crust on the Kolbeinsey Ridge, north of Iceland, over the past 22 Myr. *Terra Nova* **10**, 27–31 (1998b), doi:10.1046/j.1365-3121.1998.00166.x.
- Korenaga, J., Holbrook, W. S., Kent, G. M., Kelemen, P. B., Detrick, R. S., Larsen, H. C., Hopper, J. R. & Dahl-Jensen, T. Crustal structure of the southeast Greenland margin from joint refraction and reflection seismic tomography. *Journal of Geophysical Research* **105**, 21591–21614 (2000), doi:10.1029/2000JB900188.
- KUM – Umwelt- und Meerestechnik Kiel GmbH. *OBS-System LOBSTER, Longterm OBS for Tsunami and Earthquake Research*. pp. 4 (1997), K.U.M. Umwelt- und Meerestechnik Kiel GmbH, Kiel, URL:http://www.kum-kiel.de/eng/pdf/Lobster_eng.pdf (10 September 2013).
- Laxon, S. W. & McAdoo, D. Arctic Ocean Gravity Field Derived From ERS-1 Satellite Altimetry. *Science* **265**, 621–624 (1994), doi:10.1126/science.265.5172.621.
- Ljones, F., Kuwano, A., Mjelde, R., Breivik, A. J., Shimamura, H., Murai, Y. & Nishimura, Y. Crustal transect from the North Atlantic Knipovich Ridge to the Svalbard Margin west of Hornsund. *Tectonophysics* **378**, 17–41 (2004), doi:10.1016/j.tecto.2003.10.003.
- Ludwig, W. J., Nafe, J. E. & Drake, C. L. Seismic refraction. In *The Sea* **4, Part I** (eds Maxwell, A. E., Hill, M. N. & Robinson, A. R.), 53–84 (1970), Wiley-Interscience, New York, ISBN:0471579106.
- Lundin, E. R. & Doré, A. G. Mid-Cenozoic post-breakup deformation in the ‘passive’ margins bordering the Norwegian–Greenland Sea. *Marine and Petroleum Geology* **19**, 79–93 (2002), doi:10.1016/S0264-8172(01)00046-0.
- Lundin, E. R. & Doré, A. G. Hyperextension, serpentinitization, and weakening: A new paradigm for rifted margin compressional deformation. *Geology* **39**, 347–350 (2011), doi:10.1130/G31499.1.

- Maystrenko, Y. & Scheck-Wenderoth, M. Density contrasts in the upper mantle and lower crust across the continent–ocean transition: constraints from 3-D gravity modelling at the Norwegian margin. *Geophysical Journal International* **179**, 536–548 (2009), doi:10.1016/j.jog.2004.03.003.
- Menke W. Crustal isostasy indicates anomalous densities beneath Iceland. *Geophysical Research Letters* **26**, 1215–1218 (1999), doi:10.1029/1999GL900202.
- Mertz, D. F., Sharp, W. D. & Haase, K. M. Volcanism on the Eggvin Bank (Central Norwegian-Greenland Sea, latitude $\sim 71^\circ\text{N}$): age, source, and relationship to the Iceland and putative Jan Mayen plumes. *Journal of Geodynamics* **38**, 57–84 (2004), doi:10.1111/j.1365-246X.2009.04273.x.
- Meyer, R., van Wijk, J. & Gernigon, L. The North Atlantic Igneous Province: A review of models for its formation. *Geological Society of America Special Papers* **430**, 525–552 (2007), doi:10.1130/2007.2430(26).
- Michael, P. J., Langmuir, C. H., Dick, H. J. B., Snow, J. E., Goldstein, S. L., Graham, D. W., Lehnert, K., Kurras, G., Jokat, W., Mühe, R. & Edmonds, H. N. Magmatic and amagmatic seafloor generation at the ultraslow-spreading Gakkel ridge, Arctic Ocean. *Nature* **423**, 956–961 (2003), doi:10.1038/nature01704.
- Militzer, H. & Weber, F. *Angewandte Geophysik*, Band 3: Seismik. pp. 420 (1987), Springer, Wien, ISBN:3211817999.
- Minshull, T. A., Muller, M. R. & White, R. S. Crustal structure of the Southwest Indian Ridge at 66°E : seismic constraints. *Geophysical Journal International* **166**, 135–147 (2006), doi:10.1111/j.1365-246X.2006.03001.x.
- Mjelde, R., Digranes, P., Van Schaack, M., Shimamura, H., Shiobara, H., Kodaira, S., Naess, O., Sørenes, N. & Vågnes, E. Crustal structure of the outer Vøring Plateau, offshore Norway, from ocean bottom seismic and gravity data. *Journal of Geophysical Research* **106**, 6769–6791 (2001), doi:10.1029/2000JB900415.

8 References

- Mjelde, R., Aurvåg, R., Kodaira, S., Shimamura, H., Gunnarsson, K., Nakanishi, A. & Shiobara, H. V_P/V_S -ratios from the central Kolbeinsey Ridge to the Jan Mayen Basin, North Atlantic; implications for lithology, porosity and present-day stress field. *Marine Geophysical Researches* **23**, 125–145 (2002), doi:10.1023/A:1022439707307.
- Mjelde, R., Eckhoff, I., Solbakken, S., Kodaira, S., Shimamura, H., Gunnarsson, K., Nakanishi, A. & Shiobara, H. Gravity and S-wave modelling across the Jan Mayen Ridge, North Atlantic; implications for crustal lithology. *Marine Geophysical Researches* **28**, 27–41 (2007), doi:10.1007/s11001-006-9012-3.
- Mjelde, R., Raum, T., Breivik, A. J. & Faleide, J.I. Crustal transect across the North Atlantic. *Marine Geophysical Researches* **29**, 73–87 (2008a), doi:10.1007/S11001-008-9046-9.
- Mjelde, R., Breivik, A. J., Raum, T., Mittelstaedt, E., Ito, G. & Faleide, J.I. Magmatic and tectonic evolution of the North Atlantic. *Journal of the Geological Society, London* **165**, 31–42 (2008b), doi:10.1144/0016-76492007-018.
- Mjelde, R., Faleide, J. I., Breivik, A. J. & Raum, T. Lower crustal composition and crustal lineaments on the Vøring Margin, NE Atlantic: A review. *Tectonophysics* **472**, 183–193 (2009), doi:10.1016/j.tecto.2008.04.018.
- Morgan, W. J. Convection Plumes in the Lower Mantle. *Nature* **230**, 42–43 (1971), doi:10.1038/230042a0.
- Mosar, J., Eide, E. A., Osmundsen, P. T., Sommaruga, A. & Torsvik, T. H. Greenland – Norway separation: A geodynamic model for the North Atlantic. *Norwegian Journal of Geology* **82**, 281–298 (2002a), ISSN: 029196X.
- Mosar, J., Torsvik, T. H. & the BAT team. Opening of the Norwegian and Greenland Seas: Plate tectonics in mid Norway since the Late Permian. In *BATLAS. Mid Norway plate reconstruction atlas with global and Atlantic perspectives* (eds Eide, E. A.), 48–59 (2002b), Geological Survey of Norway, Trondheim, ISBN:8273851060.

- Muller, M. R., Minshull, T. A. & White, R. S. Segmentation and melt supply at the Southwest Indian Ridge. *Geology* **27**, 867–870 (1999), doi:10.1130/0091-7613(1999)027<0867:samsat>2.3.co;2.
- Müller, R. D., Sdrolias, M., Gaina, C. & Roest, W. R. Age, spreading rates, and spreading asymmetry of the world's ocean crust. *Geochemistry, Geophysics, Geosystems* **9**, pp. 19 (2008), doi:10.1029/2007GC001743.
- Müller-Michaelis, A., Uenzelmann-Neben, G. & Stein, R. A revised Early Miocene age for the instigation of the Eirik Drift, offshore southern Greenland: Evidence from high-resolution seismic reflection data *Marine Geology* **340**, 1–15 (2013), doi:10.1016/j.margeo.2013.04.012.
- Myhre, A. M., Thiede, J., Firth, J. V., Ahagon, N., Black, K. S., Bloemendal, J., Brass, G. W., Bristow, J. F., Chow, N., Cremer, M., Davis, L., Flower, B., Fronval, T., Hood, J., Hull, D., Koç, N., Larsen, B., Lyle, M. W., McManus, J., O'Connell, S., Osterman, L. E., Rack, F. R., Sato, T., Scherer, R. P., Spiegler, D., Stein, R., Tadross, M., Wells, S., Williamson, D., Witte, B. & Wolf-Welling, T. Site 907. In *Proceedings of the Ocean Drilling Program, Initial Reports* **151** (eds Firth, J. V.), 57–111 (1995a), College Station, Texas, doi:10.2973/odp.proc.ir.151.105.1995.
- Myhre, A. M., Thiede, J., Firth, J. V., Ahagon, N., Black, K. S., Bloemendal, J., Brass, G. W., Bristow, J. F., Chow, N., Cremer, M., Davis, L., Flower, B., Fronval, T., Hood, J., Hull, D., Koç, N., Larsen, B., Lyle, M. W., McManus, J., O'Connell, S., Osterman, L. E., Rack, F. R., Sato, T., Scherer, R. P., Spiegler, D., Stein, R., Tadross, M., Wells, S., Williamson, D., Witte, B. & Wolf-Welling, T. Site 908. In *Proceedings of the Ocean Drilling Program, Initial Reports* **151** (eds Firth, J. V.), 113–158 (1995b), College Station, Texas, doi:10.2973/odp.proc.ir.151.106.1995.
- Myhre, A. M., Thiede, J., Firth, J. V., Ahagon, N., Black, K. S., Bloemendal, J., Brass, G. W., Bristow, J. F., Chow, N., Cremer, M., Davis, L., Flower, B., Fronval, T., Hood, J., Hull, D., Koç, N., Larsen, B., Lyle, M. W., McManus, J., O'Connell,

8 References

- S., Osterman, L. E., Rack, F. R., Sato, T., Scherer, R. P., Spiegler, D., Stein, R., Tadross, M., Wells, S., Williamson, D., Witte, B. & Wolf-Welling, T. Site 909. In *Proceedings of the Ocean Drilling Program, Initial Reports* **151** (eds Firth, J. V.), 159–220 (1995c), College Station, Texas, doi:10.2973/odp.proc.ir.151.107.1995.
- Myhre, A. M., Thiede, J., Firth, J. V., Ahagon, N., Black, K. S., Bloemendal, J., Brass, G. W., Bristow, J. F., Chow, N., Cremer, M., Davis, L., Flower, B., Fronval, T., Hood, J., Hull, D., Koç, N., Larsen, B., Lyle, M. W., McManus, J., O'Connell, S., Osterman, L. E., Rack, F. R., Sato, T., Scherer, R. P., Spiegler, D., Stein, R., Tadross, M., Wells, S., Williamson, D., Witte, B. & Wolf-Welling, T. Site 913. In *Proceedings of the Ocean Drilling Program, Initial Reports* **151** (eds Firth, J. V.), 345–382 (1995d), College Station, Texas, doi:10.2973/odp.proc.ir.151.111.1995.
- O'Connor, J. M. & Duncan, R. A. Evolution of the Walvis Ridge-Rio Grande Rise Hot Spot System: Implications for African and South American Plate motions over plumes. *Journal of Geophysical Research* **95**, 17475–17502 (1990), doi:10.1029/JB095iB11p17475.
- O'Connor, J. M., Jokat, W., le Roex, A. P., Class, C., Wijbrans, J. R., Kefling, S., Kuiper, K. F. & Nebel, O. Hotspot trails in the South Atlantic controlled by plume and plate tectonic processes. *Nature Geoscience* **5**, 735–738 (2012), doi:10.1038/ngeo1583.
- Okino, K., Curewitz, D., Asada, M., Tamaki, K., Vogt, P. & Crane, K. Preliminary analysis of the Knipovich Ridge segmentation: influence of focused magmatism and ridge obliquity on an ultraslow spreading system. *Earth and Planetary Science Letters* **202**, 275–288 (2002), doi:10.1016/S0012-821X(02)00790-2.
- Peron-Pinvidic, G., Gernigon, L., Gaina, C. & Ball, P. Insights from the Jan Mayen system in the Norwegian–Greenland sea–I. Mapping of a microcontinent. *Geophysical Journal International* **191**, 385–412 (2012a), doi:10.1111/j.1365-246X.2012.05639.x.

-
- Peron-Pinvidic, G., Gernigon, L., Gaina, C. & Ball, P. Insights from the Jan Mayen system in the Norwegian–Greenland Sea–II. Architecture of a microcontinent. *Geophysical Journal International* **191**, 413–435 (2012b), doi:10.1111/j.1365-246X.2012.05623.x.
- Peron-Pinvidic, G., Manatschal, G. & Osmundsen, P. T. Structural comparison of archetypal Atlantic rifted margins: A review of observations and concepts. *Marine and Petroleum Geology* **43**, 21–47 (2013), doi:10.1016/j.marpetgeo.2013.02.002.
- Rabinowitz, P. D. Gravity measurements bordering passive continental margins. In *Dynamics of Passive Margins* **6** (eds Scrutton, R. A.), 91–115 (1982), American Geophysical Union, Washington, D.C., ISBN:0875905099, doi:10.1029/GD006p0091.
- Reid, I. & Jackson, H. R. Oceanic spreading rate and crustal thickness. *Marine Geophysical Researches* **5**, 165–172 (1981), doi:10.1007/BF00163477.
- Rickers, F., Fichtner, A. & Trampert, J. The Iceland–Jan Mayen plume system and its impact on mantle dynamics in the North Atlantic region: Evidence from full-waveform inversion. *Earth and Planetary Science Letters* **2013**, 39–51 (2013), doi:10.1016/j.epsl.2013.02.022.
- Ritsema, J., Deuss, A., van Heijst, H. J. & Woodhouse, J. H. S40RTS: a degree-40 shear-velocity model for the mantle from new Rayleigh wave dispersion, teleseismic traveltimes and normal-mode splitting function measurements. *Geophysical Journal International* **184**, 1223–1236 (2011), doi:10.1111/j.1365-246X.2010.04884.x.
- Ritzmann, O., Jokat, W., Mjelde, R. & Shimamura, H. Crustal structure between the Knipovich Ridge and the Van Mijenfjorden (Svalbard). *Marine Geophysical Researches* **23**, 379–401 (2002), doi:10.1023/B:MARI.0000018168.89762.a4.
- Ritzmann, O., Jokat, W., Czuba, W., Guterch, A., Mjelde, R. & Nishimura, Y. A deep seismic transect from Hovgård Ridge to northwestern Svalbard across the continental-

8 References

- ocean transition: A sheared margin study. *Geophysical Journal International* **157**, 683–702 (2004), doi:10.1111/j.1365-246X.2004.02204.x.
- Schindwein, V. Architecture and evolution of the continental crust of East Greenland from integrated geophysical studies=Aufbau und Entwicklungsgeschichte der kontinentalen Kruste Ostgrönlands aus integrierten geophysikalischen Untersuchungen. *Berichte zur Polar- und Meeresforschung (Reports on Polar and Marine Research)* **270**, pp. 148 (1998), Alfred Wegener Institute for Polar and Marine Research, Bremerhaven, hdl:10013/epic.10273.d001.
- Schindwein, V. & Jokat, W. Structure and evolution of the continental crust of northern east Greenland from integrated geophysical studies. *Journal of Geophysical Research* **104**, 15227–15245 (1999), doi:10.1029/1999jb900101.
- Schindwein, V. & Meyer, U. Aeromagnetic study of the continental crust of northeast Greenland. *Journal of Geophysical Research* **104**, 7527–7537 (1999), doi:10.1029/1998jb900114.
- Schindwein, V. & Jokat, W. Post-collisional extension of the East Greenland Caledonides: a geophysical perspective. *Geophysical Journal International* **140**, 559–567 (2000), doi:10.1046/j.1365-246X.2000.00036.x.
- Schmeling, H. Dynamic models of continental rifting with melt generation. *Tectonophysics* **480**, 33–47 (2010), doi:10.1016/j.tecto.2009.09.005.
- Schmidt-Aursch, M. C. & Jokat, W. The crustal structure of central East Greenland - I: From the Caledonian orogen to the tertiary igneous province. *Geophysical Journal International* **160**, 736–752 (2005a), doi:10.1111/j.1365-246X.2005.02514.x.
- Schmidt-Aursch, M. C. & Jokat, W. The crustal structure of central East Greenland—II: From the Precambrian shield to the recent mid-oceanic ridges. *Geophysical Journal International* **160**, 753–760 (2005b), doi:10.1111/j.1365-246X.2005.02515.x.

-
- Scott, R. A. Mesozoic-Cenozoic Evolution of East Greenland: Implications of a Reinterpreted Continent-Ocean Boundary Location. *Polarforschung* **68**, 83–91 (2000), hdl:10013/epic.29794.d001.
- Sleep, N. H. Mantle plumes from top to bottom. *Earth-Science Reviews* **77**, 231–271 (2006), doi:10.1016/j.earscirev.2006.03.007.
- Steinberger, B. & Torsvik, T. H. A geodynamic model of plumes from the margins of Large Low Shear Velocity Provinces. *Geochemistry, Geophysics, Geosystems* **13**, pp. 17 (2012), doi:10.1029/2011GC003808.
- Talwani, M., Udintsev, M., Bjorklund, K., Caston, V. N. D., Faas, R. W., Kharin, G. N., Morris, D. A., Müller, C., Nilsen, T. H., van Hinte, J., Warnke, D. A. & White, S. M. Site 344. In *Initial Reports of the Deep Sea Drilling Project* **38** (eds White, S. M.), 389–449 (1976a), U.S. Government Printing Office, Washington, doi:10.2973/dsdp.proc.38.105.1976.
- Talwani, M., Udintsev, M., Bjorklund, K., Caston, V. N. D., Faas, R. W., Kharin, G. N., Morris, D. A., Müller, C., Nilsen, T. H., van Hinte, J., Warnke, D. A. & White, S. M. Site 345. In *Initial Reports of the Deep Sea Drilling Project* **38** (eds White, S. M.), 451–519 (1976b), U.S. Government Printing Office, Washington, doi:10.2973/dsdp.proc.38.106.1976.
- Talwani, M., Udintsev, M., Bjorklund, K., Caston, V. N. D., Faas, R. W., Kharin, G. N., Morris, D. A., Müller, C., Nilsen, T. H., van Hinte, J., Warnke, D. A. & White, S. M. Sites 346, 347, and 349. In *Initial Reports of the Deep Sea Drilling Project* **38** (eds White, S. M.), 521–594 (1976c), U.S. Government Printing Office, Washington, doi:10.2973/dsdp.proc.38.107.1976.
- Talwani, M., Udintsev, M., Bjorklund, K., Caston, V. N. D., Faas, R. W., Kharin, G. N., Morris, D. A., Müller, C., Nilsen, T. H., van Hinte, J., Warnke, D. A. & White, S. M. Site 348. In *Initial Reports of the Deep Sea Drilling Project* **38**

8 References

- (eds White, S. M.), 595–654 (1976d), U.S. Government Printing Office, Washington, doi:10.2973/dsdp.proc.38.108.1976.
- Talwani, M., Udintsev, M., Bjorklund, K., Caston, V. N. D., Faas, R. W., Kharin, G. N., Morris, D. A., Müller, C., Nilsen, T. H., van Hinte, J., Warnke, D. A. & White, S. M. Site 350. In *Initial Reports of the Deep Sea Drilling Project* **38** (eds White, S. M.), 655–682 (1976e), U.S. Government Printing Office, Washington, doi:10.2973/dsdp.proc.38.109.1976.
- Talwani, M. & Eldholm, O. Evolution of the Norwegian-Greenland Sea. *Geological Society of America Bulletin* **88**, 969–999 (1977), doi:10.1130/0016-7606(1977)88<969:EOTNS>2.0.CO;2.
- Tolstoy, M., Bohnenstiel, D. R., Edwards, M. H. & Kurras, G. J. Seismic character of volcanic activity at the ultraslow-spreading Gakkel Ridge. *Geology* **29**, 1139–1142 (2001), doi:10.1130/0091-7613(2001)029<1139:scovaa>2.0.co;2.
- Torge, W. *Gravimetry*. pp. 465 (1989), de Gruyter, Berlin, ISBN:3110107023.
- Tsikalas, F., Eldholm, O. & Faleide, J. I. Early Eocene sea floor spreading and continent-ocean boundary between Jan Mayen and Senja fracture zones in the Norwegian-Greenland Sea. *Marine Geophysical Researches* **23**, 247–270 (2002), doi:10.1023/a:1023621228605.
- Voss, M. & Jokat, W. Continent-ocean transition and voluminous magmatic underplating derived from P-wave velocity modelling of the East Greenland continental margin. *Geophysical Journal International* **170**, 580–604 (2007), doi:10.1111/j.1365-246X.2007.03438.x.
- Voss, M., Schmidt-Aursch, M. C. & Jokat, W. Variations in magmatic processes along the East Greenland volcanic margin. *Geophysical Journal International* **177**, 755–782 (2009), doi:10.1111/j.1365-246X.2009.04077.x.

-
- Watts, A. B. & Fairhead, J. D. A process-oriented approach to modeling the gravity signature of continental margins. *The Leading Edge* **18**, 258–263 (1999).
- Weigel, W., Flüh, E. R., Miller, H., Butzke, A., Dehghani, G. A., Gebhardt, V., Harder, I., Hepper, J., Jokat, W., Kläschen, D., Kreymann, S., Schükler, S. & Zhao, Z. Investigations of the East Greenland Continental Margin between 70° and 72° N by Deep Seismic Sounding and Gravity Studies. *Marine Geophysical Researches* **17**, 167–199 (1995), doi:10.1007/bf01203425.
- Weigel, M., van Dam, T., Jäggi, A., Prange, L., Tourian, M. J., Keller, W. & Sneeuw, N. Time-Variable Gravity Signal in Greenland Revealed by High-Low Satellite-to-Satellite Tracking. *Journal of Geophysical Research* (2013, submitted).
- White, R. S. A hot-spot model for early Tertiary volcanism in the N Atlantic. *Geological Society, London, Special Publications* **39**, 3–13 (1988), doi:10.1029/JB094iB06p07685.
- White, R. & McKenzie, D. Magmatism at Rift Zones: The Generation of Volcanic Continental Margins and Flood Basalts. *Journal of Geophysical Research* **94**, 7685–7729 (1989), doi:10.1029/JB094iB06p07685.
- White, R. S., McKenzie, D. & Onions, R. K. Oceanic Crustal Thickness from Seismic Measurements and Rare Earth Element Inversions. *Journal of Geophysical Research* **97**, 19683–19715 (1992), doi:10.1029/92JB01749.
- White, R. S., Minshull, T. A., Bickle, M. J. & Robinson, C. J. Melt Generation at Very Slow-Spreading Oceanic Ridges: Constraints from Geochemical and Geophysical Data. *Journal of Petrology* **42**, 1171–1196 (2001), doi:10.1093/petrology/42.6.1171.
- White, R. S., Smith, L. K., Roberts, A. W., Christie, P. A. F., Kusznir, N. J. & the rest of the iSIMM Team. Lower-crustal intrusion on the North Atlantic continental margin. *Nature* **452**, 460–464 (2008), doi:10.1038/nature06687.

8 References

- Whitmarsh, R. B. & Miles, P. R. Models of the development of the West Iberia rifted continental margin at 40°30'N deduced from surface and deep-tow magnetic anomalies. *Journal of Geophysical Research* **100**, 3789–3806 (1995), doi:10.1029/94jb02877.
- Whitmarsh, R. B., White, R. S., Horsefield, S. J., Sibuet, J.-C., Recq, M. & Louvel, V. The ocean-continent boundary off the western continental margin of Iberia: Crustal structure west of Galicia Bank. *Journal of Geophysical Research* **101**, 28291–28314 (1996), doi:10.1029/96JB02579.
- van Wijk, J. W., Huismans, R. S., ter Voorde, M. & Cloetingh, S. A. P. L. Melt Generation at Volcanic Continental Margins: no Need for a Mantle Plume? *Geophysical Research Letters* **28**, 3995–3998 (2001), doi:10.1029/2000GL012848.
- Winter, F. North East Greenland Margin, Airborne Magnetics and Gravity. *Diploma Thesis*, pp. 111 (2011), Ludwigs-Maximilians-Universität München, unpublished.
- Worzel, J. L. Advances in marine geophysical research of continental margins. *Canadian Journal of Earth Sciences* **5**, 963–983 (1968), doi:10.1139/e68-095.
- Yamasaki, T. & Gernigon, L. Redistribution of the lithosphere deformation by the emplacement of underplated mafic bodies: implications for microcontinent formation. *Journal of the Geological Society, London* **167**, 961–971 (2010), doi:10.1144/0016-76492010-027.
- Yilmaz, Ö. *Seismic Data Analysis - Processing, Inversion and Interpretation of Seismic Data*. pp. 2027 (2001), Society of Exploration Geophysics, Tulsa/Oklahoma, ISBN:1560800984.
- Zelt, C. A. & Smith, R. B. Seismic traveltime inversion for 2-D crustal velocity structure. *Geophysical Journal International* **108**, 16–34 (1992), doi:10.1111/j.1365-246X.1992.tb00836.x.

- Zelt, C. A. Modelling strategies and model assessment for wide-angle seismic travelttime data. *Geophysical Journal International* **139**, 183–204 (1999), doi:10.1046/j.1365-246X.1999.00934.x.
- Zelt, B. C. *ZP – Software for plotting wide-angle seismic data in SEG-Y format*. pp. 37 (2004), Hawaii Institute of Geophysics and Planetology, School of Ocean and Earth Science and Technology, University of Hawaii.

8 References

A Appendix (Seismic Refraction Data)

Further examples of seismic refraction data, modelled ray coverage, and comparisons between modelled and picked travel times, are shown in the following figures. Concerning the P-waves of line 20090200, the following examples are presented: (1) OBS data with picked far offset waves (up to 150 km offset, Fig. A.1), and (2) an OBS station located in the Knipovich Ridge rift valley (Fig. A.2). For the S-wave modelling of line 20090200, Fig. A.5 shows observed and calculated P-wave as well as S-wave travel times for stations with: (1) thick sediments (station 202), (2) crust-mantle boundary reflections (stations 202, 207), (3) thin sediments (station 210), and (4) refractions of all three crustal layers (stations 212, 213, 217). P-wave examples of line 20090100 show: (1) an OBS station near the Kolbeinsey Ridge rift valley with no sediment cover (Fig. A.3), and (2) an OBS station near the shelf slope with thick sediments (Fig. A.4). The locations of the different stations are shown in Figure 3.1.

A Appendix (Seismic Refraction Data)

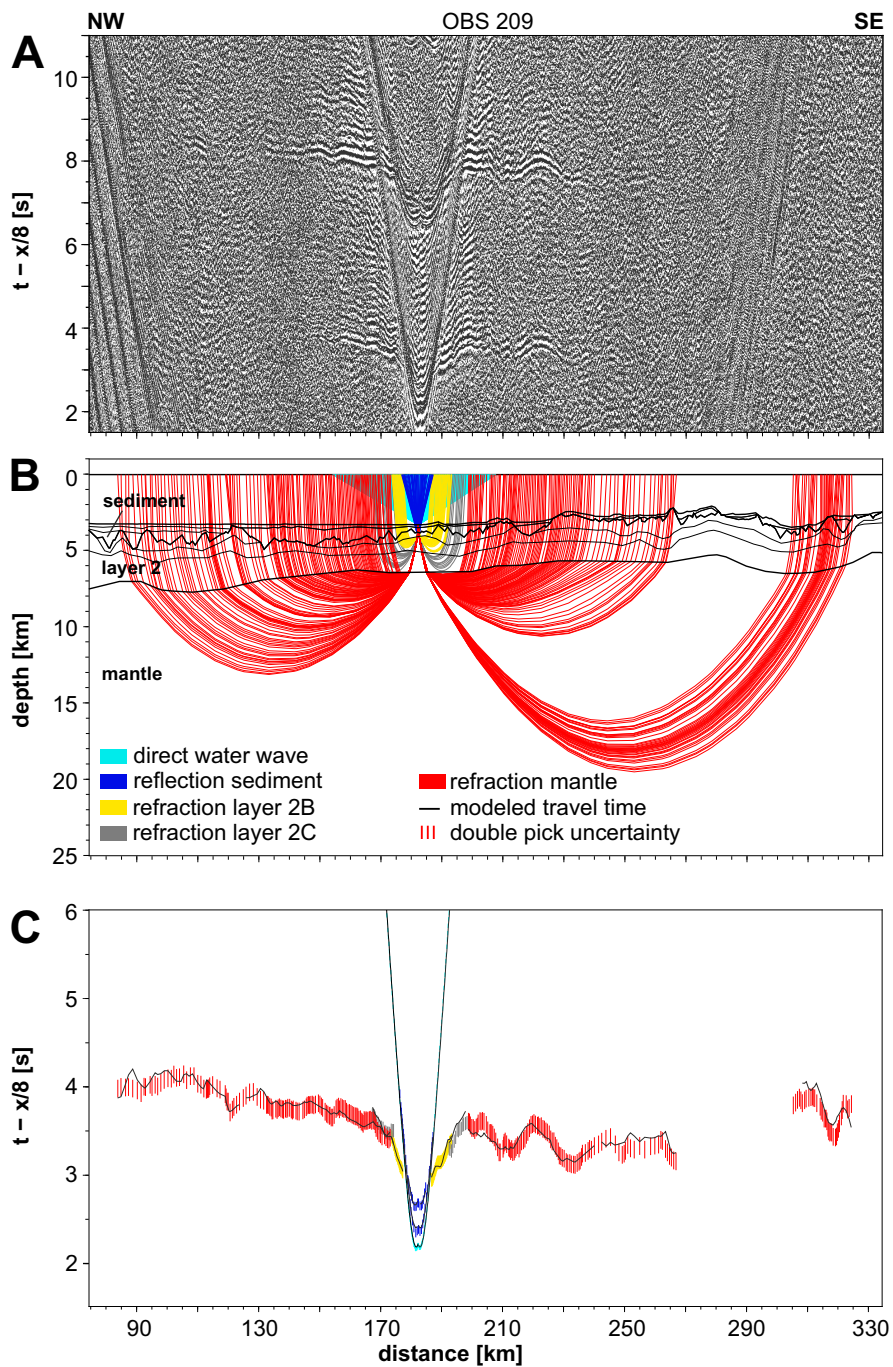


Figure A.1: OBS data example (station 209) of line 20090200 used for the P-wave modelling. (A) Processed data of hydrophone channel, (B) modelled ray coverage, and (C) modelled and picked travel times (Hermann & Jokat 2013a). The upper and lower figure are plotted with a reduction velocity of 8 km/s. Both vertical scales are of different exaggeration.

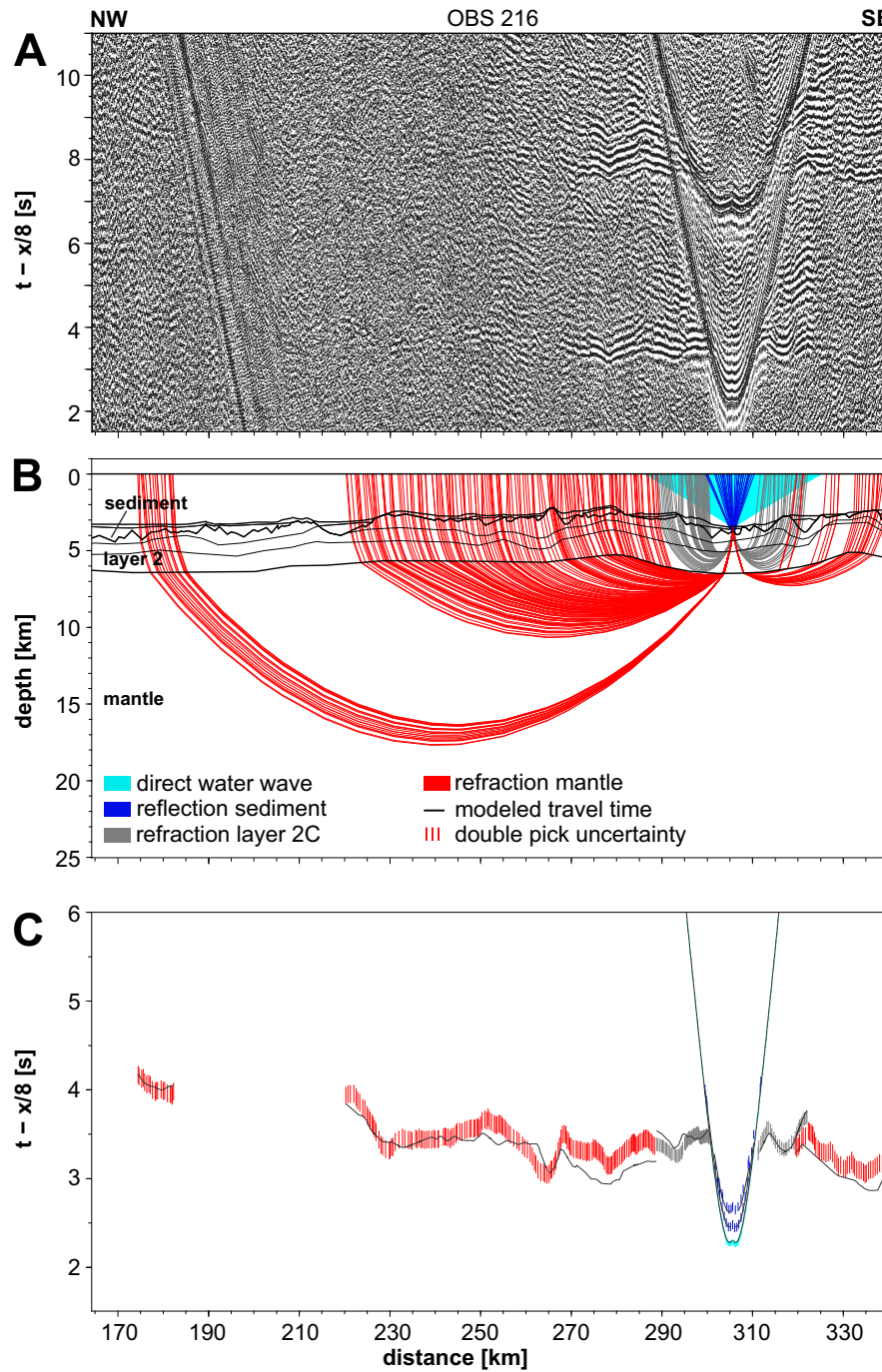


Figure A.2: OBS data example (station 216) of line 20090200 used for the P-wave modelling. (A) Processed data of hydrophone channel, (B) modelled ray coverage, and (C) modelled and picked travel times (Hermann & Jokat 2013a). The upper and lower figure are plotted with a reduction velocity of 8 km/s. Both vertical scales are of different exaggeration.

A Appendix (Seismic Refraction Data)

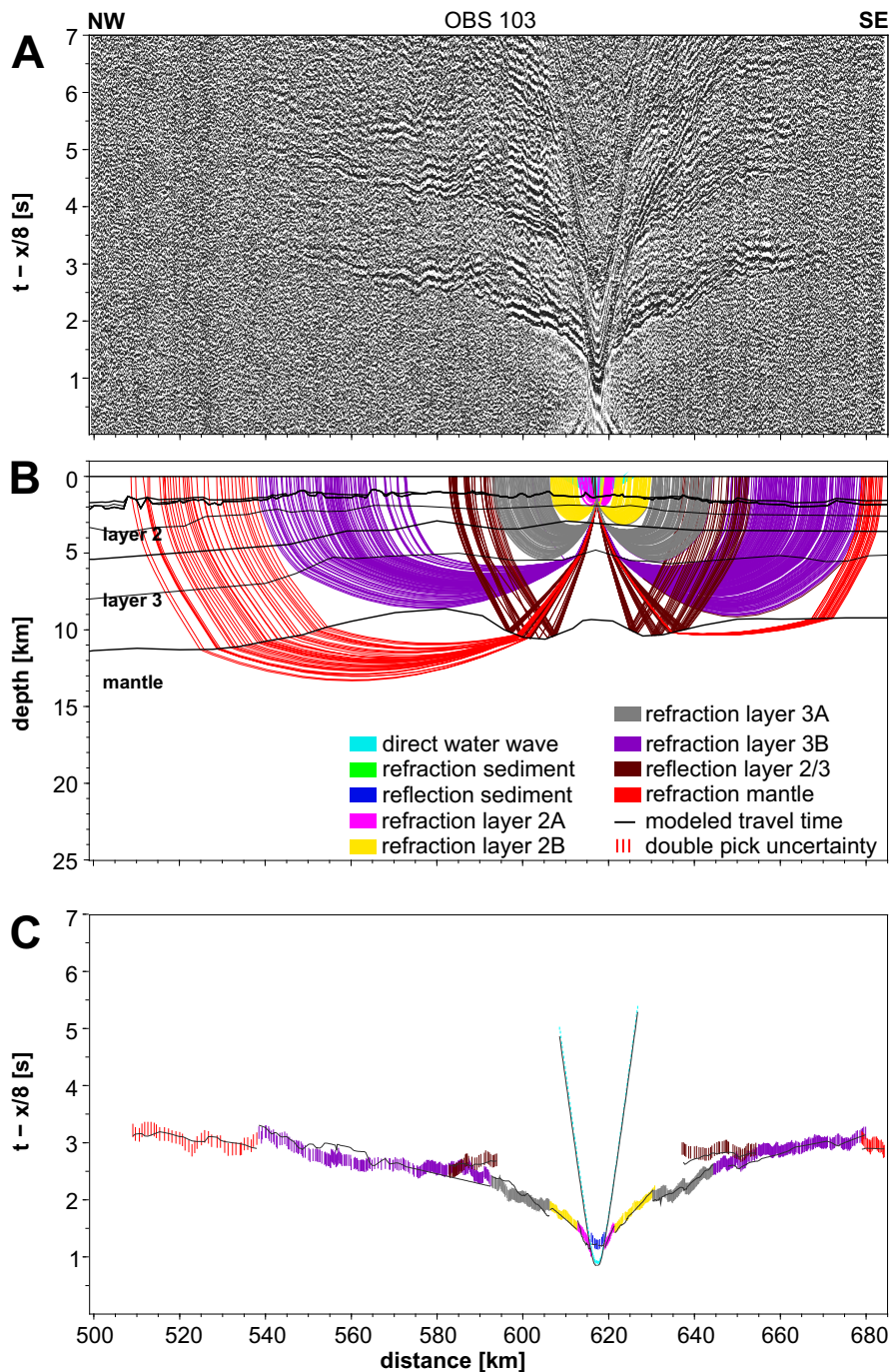


Figure A.3: OBS data example (station 103) of line 20090100 used for the P-wave modelling. (A) Processed data of hydrophone channel, (B) modelled ray coverage, and (C) modelled and picked travel times (Hermann & Jokat 2013b). The upper and lower figure are plotted with a reduction velocity of 8 km/s. Both vertical scales are of different exaggeration.

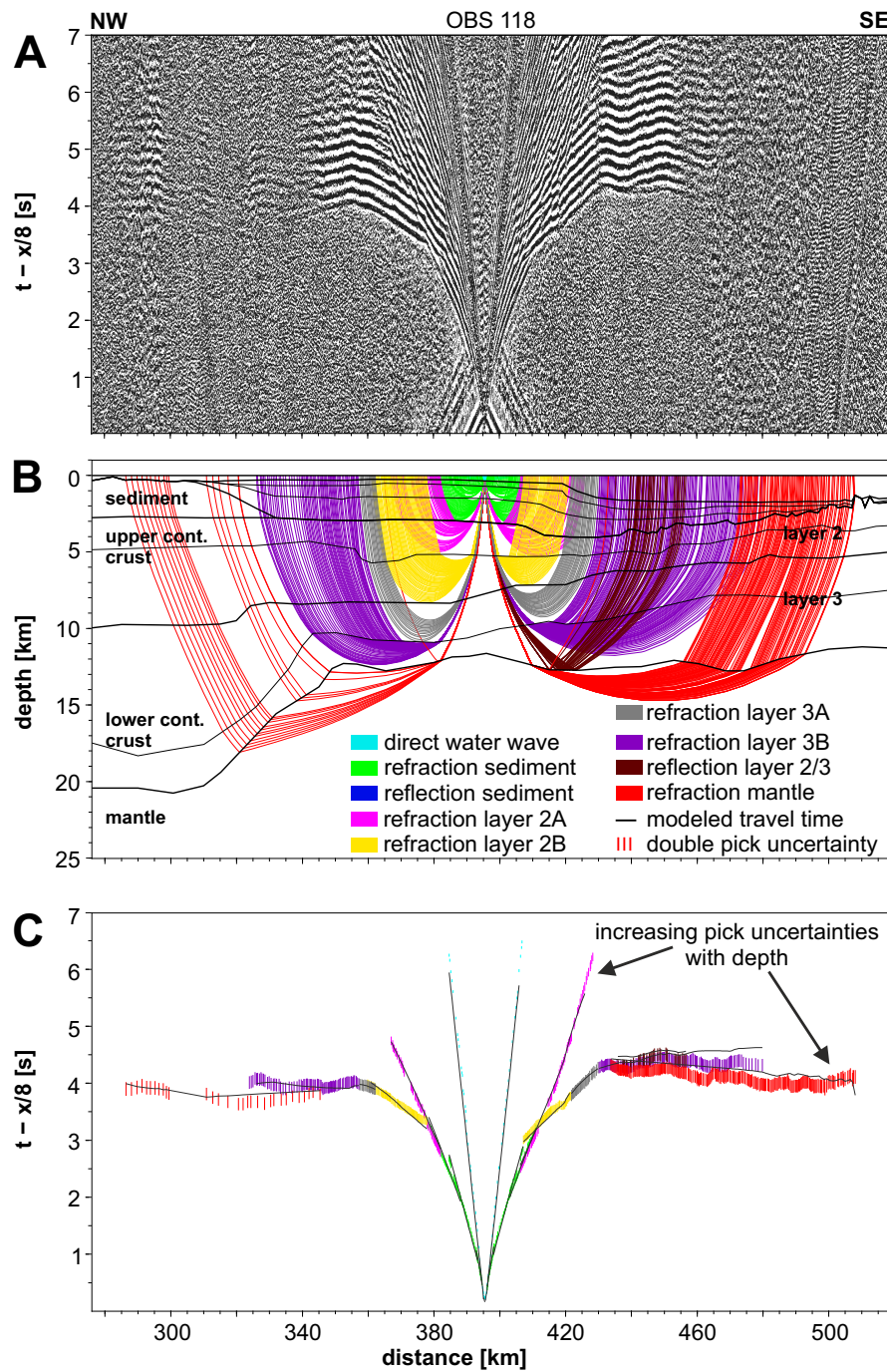


Figure A.4: OBS data example (station 118) of line 20090100 used for the P-wave modelling. (A) Processed data of hydrophone channel, (B) modelled ray coverage, and (C) modelled and picked travel times (Hermann & Jokat 2013b). The upper and lower figure are plotted with a reduction velocity of 8 km/s. Both vertical scales are of different exaggeration.

A Appendix (Seismic Refraction Data)

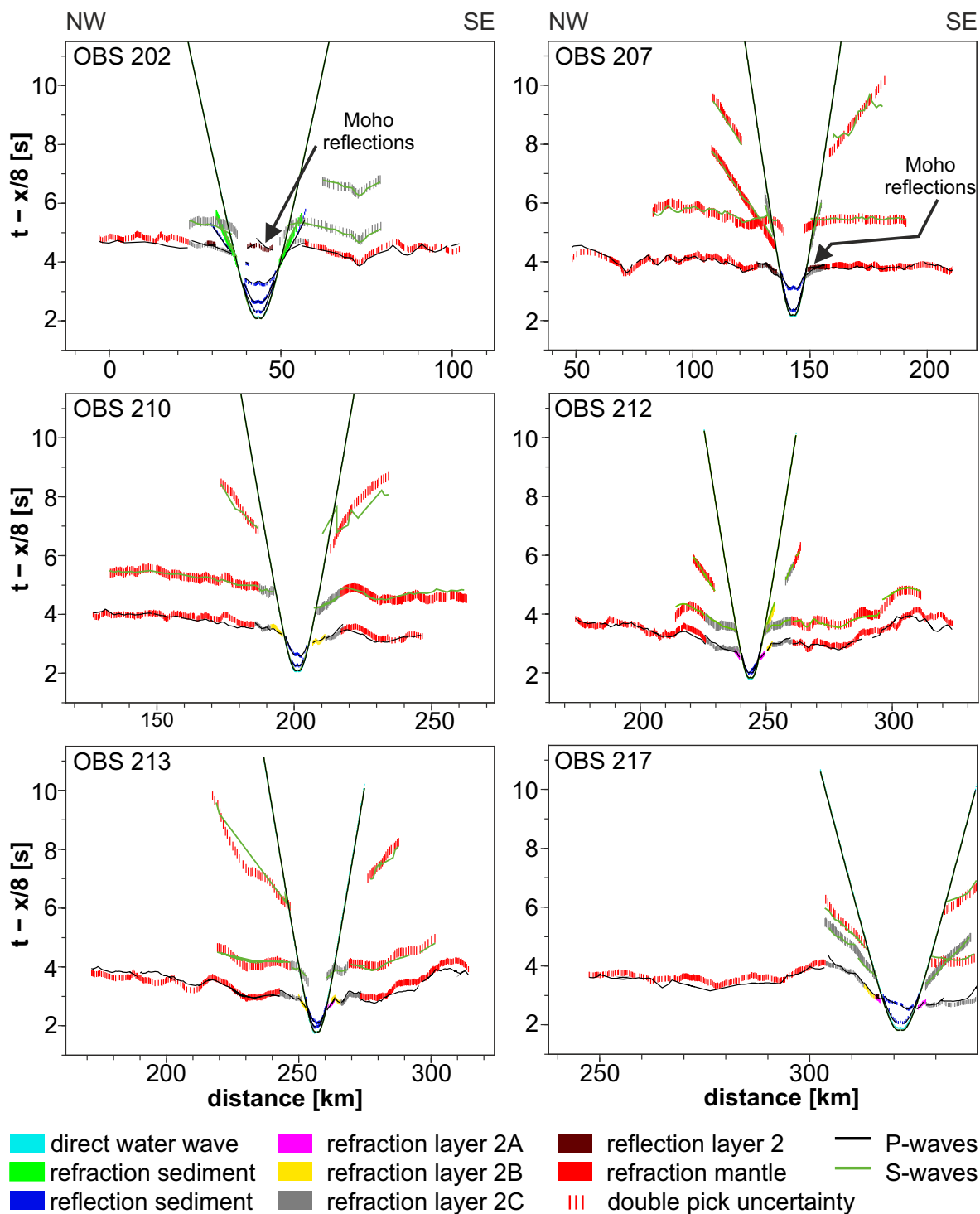


Figure A.5: Observed and calculated P-wave as well as S-wave travel times from selected OBS stations of line 20090200 plotted with a reduction velocity of 8 km/s (Hermann & Jokat 2013a). The horizontal scales are of different exaggeration.

Acknowledgement

Finally, let me express my sincere thanks and appreciation to all people mentioned below for their help and support during my 3 years PhD work at the Alfred Wegener Institute in Bremerhaven and the Friedrich Schiller University in Jena.

First of all, I would like to thank my doctoral advisor, Prof. Dr. Gerhard Jentzsch from the Friedrich Schiller University in Jena, for supervising my PhD thesis. Furthermore, constructive and helpful comments during my 3 years PhD work are gratefully acknowledged.

Secondly, I would like to thank my supervisor, Prof. Dr. Wilfried Jokat from the Alfred Wegener Institute in Bremerhaven, for the possibility to attend several international congresses and ship expeditions. Furthermore, discussions about seismic refraction modelling and constructive comments during my 3 years PhD work are appreciated.

My internal examiner, PD Dr. Thomas Jahr from the Friedrich Schiller University in Jena, is thanked for taking over the evaluation of my thesis, as well as constructive and helpful comments during my 3 years PhD work, in particular, during my final writing phase.

Dr. Thomas Funck from the Geological Survey of Denmark and Greenland in Copenhagen is thanked for interesting and helpful discussions about crustal and upper mantle structures of the Boreas Basin and the East Greenland Ridge. Furthermore, fruitful comments and discussions about the compilation of the ray tracing software *RAYINVR* are acknowledged.

The captain and the crew of RV Polarstern as well as the seismic team is gratefully acknowledged for their excellent job during the ARK-XXIV/3 summer expedition in 2009.

The AWI marine geophysics group I would like to thank for the good working atmosphere, listening to questions and discussing problems.

I am very grateful to Anne Hegewald and Stefanie Kaboth for their proofreading of my

Acknowledgement

first manuscript published by Geophysical Journal International and the final thesis.

Thus, my English became much clearer.

Finally, my **friends** and **family** are thanked for all the great things, activities and help.

Selbstständigkeitserklärung

Ich erkläre, dass ich die vorliegende Arbeit selbstständig und unter Verwendung der angegebenen Hilfsmittel, persönlichen Mitteilungen und Quellen angefertigt habe.

Jena, den 06. November 2013

Tobias Hermann

Selbstständigkeitserklärung

Curriculum Vitae

Personal details

Name: Tobias Hermann
Date of birth: 22. July 1986
Place of birth: Zeulenroda
Nationality: German

Education

08/97 to 06/05 **High School Diploma**, Friedrich-Schiller-Gymnasium Zeulenroda
10/05 to 08/10 **Geophysics Study**, Friedrich Schiller University Jena
since 09/10 **PhD Student**, Friedrich Schiller University Jena and AWI

Employments

10/07 to 07/10 **Student Assistant**, Friedrich Schiller University Jena
08/09 to 09/09 **Trainee**, German Research Centre for Geosciences Potsdam
since 09/10 **PhD Student**, Alfred Wegener Institute Bremerhaven

Experiences

12/10 to 01/11 **Research Assistant**, RV M. S. Merian expedition (MSM 17-2), charged by GEOMAR & AWI, southwest Africa and Walvis Ridge
08/11 to 09/11 **Research Assistant**, RV Oden expedition (EAGER 2011), charged by GEUS, northwest Greenland and East Greenland Ridge
10/12 to 11/12 **Research Assistant**, RV Sonne expedition (SO 224), charged by AWI, Manihiki Plateau (southwest Pacific Ocean)

Conference Presentations

- 10/09 Geoelektrische Hydrountersuchungen am Geodynamischen Observatorium Moxa - eine Fortführung.
study group Geophysics & Geodesy Conference, Brandenburg
- 03/10 Geoelektrische Wiederholungsmessungen am Geodynamischen Observatorium Moxa
DGG Conference, Bochum
- 06/11 First results from a seismic refraction experiment in the Boreas Basin – Northeast Greenland
Internationale Conference on Arctic Margins, Fairbanks
- 04/12 Crustal structure of the Boreas Basin formed at ultraslow spreading Knipovich Ridge - Northern North Atlantic
EGU Conference, Vienna
- 09/12 Crustal structures along the North-East Greenland margin
Seismix Symposium, Beijing (funded by DAAD)

Jena, den 06. November 2013

Tobias Hermann